Title
Microscale tools for improved analytical sensitivity and throughput in single-cell immunoblotting

Permalink
https://escholarship.org/uc/item/7g79t56c

Author
Mourdoukoutas, Antonios P

Publication Date
2021

Peer reviewed|Thesis/dissertation

Microscale tools for improved analytical sensitivity and throughput in single-cell immunoblotting

By

Antonios P Mourdoukoutas

A dissertation submitted in partial satisfaction of the

requirements for the degree of

Doctor of Philosophy

in

Bioengineering

in the

Graduate Division

of the

University of California, Berkeley

Committee in charge:

Professor Amy E. Herr, Chair
Professor Aaron Streets
Professor Mekhail Anwar

Summer 2021

Microscale tools for improved analytical sensitivity and throughput in single-cell immunoblotting

Abstract

Microscale tools for improved analytical sensitivity and throughput in single-cell immunoblotting

by

Antonios P Mourdoukoutas

Joint Doctor of Philosophy in Bioengineering
With the University of California, San Francisco

University of California, Berkeley

Dissertation Mentor:
Professor Amy E. Herr, Chair

Proteins drive nearly all cellular processes, and direct quantitation of protein abundance from single-cells is essential to understanding heterogeneous cell states.[1,2] Immunoassays are widely accepted tools for performing single-cell protein detection,[3,4] but protein detection by immunoaffinity alone is insufficient for precision protein characterization, as proteins with similar binding kinetics can have different biological impacts, including in disease.[5,6,7] To provide a cross-validation tool for protein characterization, electrophoretic cytometry immunoassays have been developed to characterize proteins by both immunoaffinity and molecular-mass through electrophoresis.[8,9] Central to these assays performance is a multifunctional gel matrix that acts as a protein sieving matrix during electrophoresis and a protein scaffolding matrix during in-gel immunoblotting. In-gel immunoblotting of target proteins is widely accomplished by diffusively-driven immunoprobing, yet, this detection strategy suffers from reduced probe access to in-gel immobilized proteins via size-exclusion partitioning. Specifically, reduced probe delivery to the gel matrix in which target proteins are immobilized both (i) adversely impacts equilibrium immunocomplex formation and thus protein detection sensitivity and (ii) extends overall assay run time.

In this dissertation, to improve the analytical detection capabilities and improve assay throughput in electrophoretic cytometry assays, we present methods to enhance immunoprobe delivery to hydrogel matrices, we introduce an assay design to improve throughput in single-cell immunoblotting, and we investigate reengineered sample handling designs for reduced protein losses before immobilization.

Overall, we apply fundamentals in materials science, transport and reaction phenomena, and engineering design principles for the advancement of targeted protein detection assays. We see these advancements as contributing to the broader goal of improving our understanding of cell-state in healthy and disease conditions.

To my family, friends, and the many people in my support network.

Table of Contents

List of Figures

List of Tables

Acknowledgements

You learn a lot of things in Grad School. All science aside, the most important lesson I've learned is that my ambitions will always be out of reach if my support systems are not intact. I am grateful to the PhD journey for driving this lesson home, and to the people in my support system for backing me time and time again.

I am fortunate to come from a loving, loud, chaotic family. I am thankful for *my mom, Rose*, who has brought endless energy and love into my childhood home. I am inspired by *my baba*, *Pavlos*, for his courage in chasing an education far away from his home so that I could have more opportunities in my life. I am thankful for my siblings – for *my brother, Dimitri*, for being my strongest reminder to enjoy life, and *my sister, Eleni,* who inspires me to be as compassionate, kind, and thoughtful as she is. To *GP* and *Nana*, *Γιαγιά* και *Παππού,* the *Mourdoukoutas's* and the *Malave's*, your love has played a huge role in shaping who I am today.

Since my childhood in Lindenhurst, I have always felt most at home when I'm surrounded by big, expressive, honest friend groups. My friends encourage me to hold no reservations in being myself. They celebrate me when I'm flying and keep me in check when I overstep. In every place that I've lived, in every phase of my life, I've been fortunate to build new loving, irreplaceable friendships. To name a few, shoutout to the *Lindenhurst gang*, and the *CUNY crew* - especially *Mikko Baylosis* and *Stevie Borrello* for way too many free phone call therapy sessions. In Berkeley, especially during the pandemic, I have finally felt at home with *Hunter Johnson, Jordan Baker, Amanda Meriwether, María Díaz de León Derby* and *Nina Yanagisawa (and Callie)*. *Nick Altemose*, your friendship has been filled with wisdom, empathy, and swoleful morning gains.

Thanks to my high school AP Physics teacher, *Mr. Tonn*, and my AP Calculus teacher, *Mr. Ehrhardt*, for inspiring me to pursue engineering in my undergrad. At CCNY, thank you to *Prof. Marom Bikson* for giving me my first experience in research, and to *Prof. Maribel Vazquez* for her mentorship and support, both as my professor at CUNY and through her friendship afterwards. Thank you to the CCNY Honors Center for believing in my academic potential. In particular, thanks to *Jennifer Lutton* for spending countless hours working with me on various scholarship and graduate school applications – I've done my best to take advantage of the opportunities that you've helped make available to me, and I sincerely hope that I've made you proud.

My research advisor, *Prof. Amy Herr*, sets a strong standard of what it means to work hard; her determination is remarkable. I am grateful to Amy for prioritizing research meetings with me and all of her trainees, and for letting me be a part of her research group, despite not having any wet lab experience before day 1 of my rotation in her lab. A particularly enjoyable aspect of the Herr Lab is the wonderful people I've been able to work alongside for the past 5 years. In particular, thank you to *Dr. Samantha Grist* and *Dr. Julea Vlassakis* for being incredible in-lab peer advisors, and for *Ali Su* and *Alisha Geldert* for their friendship and quals companionship.

I am grateful for my qualifying exam and dissertation committee members: *Prof. Lydia Sohn*, *Prof. Mekhail Anwar, Prof. Michael Rape, Prof. Rikky Muller,* and especially *Prof. Aaron Streets* – it was a joy to teach a very difficult course on Biological Mass Transport Phenomena alongside you. And lastly, thank you to the National Science Foundation for funding my research through a Graduate Research Fellowship and making my PhD dream possible.

1 Introduction

1.1 Need for single-cell proteoform-specific analysis

Understanding cell state at the single-cell level allows us to study the heterogeneity of the cells in our bodies that is responsible for both the function of our tissues in healthy states and dysfunction in disease states. Single-cell studies permit identification of rare subpopulations that can be biologically and clinically important but lost in bulk analyses, such as drug-resistant tumor cells. Cell state can be characterized by many complementary measurements. These include the characterization of cell morphology traits, such as whole cell size, size ratios of cell nucleus to cytoplasm, cell shape, as well the characterization of cell molecular abundances, such as DNA, RNA and proteins. Recently, technological advances in sequencing techniques have empowered the growth of genomic and transcriptomic tools for measuring DNA and RNA expression. Yet, while providing valuable insights into cell state, DNA and RNA do not predict protein expression at the single-cell level.

Proteins drive nearly all cellular processes, and direct quantitation of protein abundance from single-cells is thus a critical complementary tool to understanding heterogeneous cell states.[1,2] Additionally, while the human genome project revealed that there are ~20,000 protein coding genes in human genome, estimates of the number of distinct human protein forms ("proteoforms") is much greater, some as large as ~6 million. Proteoforms are different forms of proteins arising from the same gene. They are created by a variety of processes including alternative RNA splicing and post-translational modifications, and can also play key roles in biological processes, including in disease. An example is the HER2 membrane oncoprotein and its truncated isoforms. HER2 is an important target for cancer therapy, but it can exist in both full-length and truncated forms that lack the extracellular binding domain for targeted therapy. The truncated proteoforms are clinically important biomarkers of disease, as they have been shown to be linked with resistance to treatment and metastasis. To assess single-cell state, including understanding the role proteoforms play in disease and to inform therapeutic interventions, there is a need to perform proteoform-specific measurements at the single-cell level.

1.2 Electrophoretic cytometry for single-cell targeted proteomics

Immunoassays are widely accepted tools for performing single-cell protein detection,[3,4] but protein detection by immunoaffinity alone is insufficient for precision protein characterization, as proteins with similar binding kinetics (often including proteoform families) can have different biological impacts, including in disease.[5,6,7] To provide a cross-validation tool for protein characterization, Western blotting has been used extensively for decades to characterize proteins by both molecular-mass and immunoaffinity through electrophoresis of bulk biological samples.[8,9]

Since then, protein sizing and immunoaffinity characterization has been brought to the single-cell level through technologies that confine individual cells to microscale fluid compartments. Microfluidic devices for single-cell protein interrogation began with important innovations in

capillary electrophoresis systems, but suffered from throughput bottlenecks, as cells are interrogated in series (one-by-one).[10,11,12]

To improve throughput in single-cell protein electrophoresis, a class of "open" (not confined to capillary channel) hydrogel electrophoretic cytometry technologies have been developed. These tools improve on capillary electrophoresis technologies by massively parallelizing single-cell protein electrophoresis, enabling the simultaneous interrogation of dozens of protein targets from thousands of single-cells in compact chips that require short assay timescales and small sample volumes.[13,14,15] The open devices consist of a hydrogel matrix with an array of thousands of microwells patterned into the surface of the gel, and parallel cellular interrogation by electrophoretic cytometry is achieved as: (i) individual cells are isolated into microwells, (ii) the cells are chemically lysed in microwells, (iii) an electric field is applied across the device and the gel acts as a molecular sieving matrix during electrophoresis, (iv) immediately after electrophoresis, the hydrogel acts as a molecular scaffolding matrix chemically immobilizing size-separated proteins in the gel, and (v) finally, the entire gel matrix can be diffusively immunoprobed for in-gel immunoblotting of target proteins. Critical to operation in these devices is the multifunctionalization of the hydrogel matrix to both perform protein sizing and protein scaffolding on chip via in-gel protein immobilization. However, integrating these distinct assay stages into a single gel matrix presents a challenge to protein readout by diffusive immunoprobing, as the gel matrix itself limits probe access to protein targets immobilized in gel. Specifically, (i) size-exclusion partitioning limits diffusive probe loading to a hydrogel and (ii) slow diffusive probe transfer relative to immunocomplex dissociation reduces probed signal at assay readout. These challenges are exacerbated in small-pore gels used for protein sizing.

To improve the analytical sensitivity of proteoform detection in open hydrogel electrophoretic cytometry assays, there is a need to design novel immunoprobing strategies and immunoassay formats that overcome size-exclusion partitioning in hydrogel immunoprobing.

1.3 Dissertation overview

This dissertation reports on tools development that involves the application of materials science, transport and reaction phenomena, and engineering design principles for (i) improved analytical sensitivity and single-cell throughput of in-gel protein detection, (ii) (ii) the design of novel assay formats to circumvent the need for in-gel protein immobilization, and (iii) the design of novel assay formats to complement intracellular proteoform measurements with secreted protein measurements.

Chapter 2: Rapid electrotransfer probing for improved detection sensitivity in in-gel immunoassays
Protein electrotransfer in conventional western blotting facilitates detection of size-separated proteins by diffusive immunoprobing, as analytes are transferred from a small-pore sizing gel to a blotting membrane for detection. This additional transfer step can, however, impair detection sensitivity through protein losses and confound protein localization. To overcome challenges associated with protein transfer, in-gel immunoassays immobilize target proteins to the hydrogel matrix for subsequent in-gel immunoprobing. Yet, detection sensitivity in diffusive

immunoprobing of hydrogels is determined by the gel pore size relative to the probe size, and in-gel immunoprobing results in (i) reduced in-gel probe concentration compared to surrounding free-solution, and (ii) slow in-gel probe transfer compared to immunocomplex dissociation. Here, we demonstrate electrotransfer probing for effective and rapid immunoprobing of in-gel immunoassays. Critically, probe (rather than target protein) is electrotransferred from an inert, large-pore 'loading gel' to a small-pore protein sizing gel. Electric field is used as a tuneable parameter for electromigration velocity, providing electrotransfer probing with a fundamental advantage over diffusive probing. Using electrotransfer probing, we observe $6.5 \pm 0.1\times$ greater probe concentration loaded in-gel in $\sim82\times$ time reduction, and $2.7 \pm 0.4\times$ less probe concentration remaining in-gel after unloading in $\sim180\times$ time reduction (compared to diffusive probing). We then apply electrotransfer probing to detect OVA immobilized in-gel and achieve $4.1 \pm 3.4\times$ greater signal-to-noise ratio and $30\times$ reduction in total immunoprobing duration compared to diffusive probing. We demonstrate electrotransfer probing as a substantially faster immunoprobing method for improved detection sensitivity of protein sizing in-gel immunoassays.

Chapter 3: 3D projection electrophoresis for single-cell immunoblotting

Immunoassays and mass spectrometry are powerful single-cell protein analysis tools; however, interfacing and throughput bottlenecks remain. Here, we introduce three-dimensional single-cell immunoblots to detect both cytosolic and nuclear proteins. The 3D microfluidic device is a photoactive polyacrylamide gel with a microwell array-patterned face (xy) for cell isolation and lysis. Single-cell lysate in each microwell is "electrophoretically projected" into the 3rd dimension (z-axis), separated by size, and photo-captured in the gel for immunoprobing and confocal/light-sheet imaging. Design and analysis are informed by the physics of 3D diffusion. Electrophoresis throughput is > 2.5 cells/s (70× faster than published serial sampling), with 25 immunoblots/mm2 device area (>10× increase over previous immunoblots). The 3D microdevice design synchronizes analyses of hundreds of cells, compared to status quo serial analyses that impart hours-long delay between the first and last cells. Here, we introduce projection electrophoresis to augment the heavily genomic and transcriptomic single-cell atlases with protein-level profiling.

Chapter 4: Microgel-membrane chips for expedited and enhanced immunoprobe delivery to gel by electrotransfer

In-gel immobilization of target analytes in microgel electrophoretic cytometry immunoassays facilitates targeted protein detection from 1000's of single-cells on a single glass microscope slide chip. While immunoblotting of target proteins in-gel is widely accomplished by diffusively-driven immunoprobing, this detection strategy suffers from limited probe access to in-gel immobilized proteins via size-exclusion partitioning. Specifically, limited probe delivery to the gel matrix in which target proteins are immobilized both (i) adversely impacts equilibrium immunocomplex formation and thus protein detection sensitivity and (ii) extends overall assay run time. To improve the total mass of probe delivery and expedite the rate of probe delivery to microgel immunoassays, we introduce a microgel chip designed to overcome size-exclusion partitioning through electrotransfer probe loading. In this chip, electrotransfer probe delivery to gel is facilitated by grafting microgel layers to electrically permeable nanoporous membranes instead of to conventionally used glass microscope slides (electrically impermeable). In developing the microgel-membrane chip, we (i) establish engineering design rules for minimizing diffusive probe losses during electrotransfer probe loading, (ii) introduce a silanization method for grafting polyacrylamide microgel layers to a

nanoporous regenerated cellulose membranes, (iv) introduce a protocol for microgel-membrane chip fabrication with precision patterning of microwell features, (iv) characterize the silane-treated membranes to preserve >70% their electrical current conductivity compared to untreated membranes, and (v) demonstrate that 1 min of electrotransfer probe loading to our microgel-membrane chip results in ~80X greater probe delivery than 1 min of diffusive delivery, and ~5X greater probe delivery than 1 hr of diffusive delivery. We see our microgel-membrane fabrication technique being adopted in the design of electrotransfer probing strategies to improve analytical sensitivity and reduce time from intact cell to protein detection readout in emerging microgel electrophoretic cytometry immunoassays.

Chapter 5: Simulated and Experimental Feasibility of Using an Offset Electrode Configuration for Direct Electrotransfer
Conventional western blotting protocols involve multiple hands-on steps that are time consuming. Furthermore, during the blotting step when proteins are transferred from the separation gel to the membrane, there is a risk of over transferring smaller molecular weight species such that they pass through the membrane. To address both of these concerns, Thermo Fisher Scientific designed a prototype electrotransfer system with an "offset" electrode configuration that would leverage electrotransfer of protein in both the vertical and lateral dimensions. The offset design has the potential to 1) prevent over transferring smaller-sized species, retaining smaller proteins laterally on the blotting membrane as larger proteins elute from the gel and 2) simplify the conventional western blot workflow by minimizing handling. However, due to the addition of the lateral dimension, non-uniformities arise in electric field and path length, as expected from theory, resulting in performance losses such as lower transfer efficiency, particularly with higher molecular weight targets and protein band dispersion. Thus, we determined the operational regimes and performance losses for gel to membrane electrotransfer of separated proteins using an 'offset electrode configuration' compared to conventional vertical electrotransfer.

Appendix: Towards an Assay for Dual Secreted Protein and Intracellular Proteoform Measurement from Single Cells
To perform dual secreted protein and intracellular protein isoform measurements from single-cells, we introduce a proposal for an integrated device that facilitates on-chip detection of both molecular types. Our proposed chip builds on enclosed microengraving technologies for single-cell secreted protein measurement, but incubates cells in a microwell array patterned into polyacrylamide gel, instead of PDMS. After capture of secreted proteins by microengraving, intracellular protein isoforms can be interrogated by using thepolyacrylamide gel matrix for single-cell Western blotting directly on chip. Towards our development of this assay, we first develop analytical modelling analyses to inform the lower limit of secreted protein detection from single cells in our proposed design. Next, we identify a model cell line and target secreted protein, and determine an approximation of the single-cell protein secretion rate of our model biological system. Then, we validated a method for antibody patterning on poly-L-lysine treated glassslides for subsequent use as microengraving capture surfaces. Finally, we apply the antibody patterned microengraving capture surfaces for preliminary detection experiments of secreted protein from bulk solution and single-cells. While these initial experiments prove unsuccessful, we identify potential causes of experimental failures and identify potential next experimental steps.

1.4 References

1   J. Berg, T. JL and S. L., in *Biochemistry*, 5th ed.

2   C. Vogel, R. D. S. Abreu, D. Ko, S. Le, B. A. Shapiro, S. C. Burns, D. Sandhu, D. R. Boutz, E. M. Marcotte and L. O. Penalva, *Mol. Syst. Biol.*, 2010, **6**, 1–9.

3   F. Chen, P. W. Tillberg and E. S. Boyden, *Science (80-.).*, 2015, **347**, 543–548.

4   I. Costantini, J. P. Ghobril, A. P. Di Giovanna, A. L. Allegra Mascaro, L. Silvestri, M. C. Müllenbroich, L. Onofri, V. Conti, F. Vanzi, L. Sacconi, R. Guerrini, H. Markram, G. Iannello and F. S. Pavone, *Sci. Rep.*, 2015, **5**, 9808.

5   L. M. Smith, N. L. Kelleher and P. Consortium for Top Down, *Nat Methods*, 2013, **10**, 186–187.

6   R. Aebersold, J. N. Agar, I. J. Amster, M. S. Baker, C. R. Bertozzi, E. S. Boja, C. E. Costello, B. F. Cravatt, C. Fenselau, B. A. Garcia, Y. Ge, J. Gunawardena, R. C. Hendrickson, P. J. Hergenrother, C. G. Huber, A. R. Ivanov, O. N. Jensen, M. C. Jewett, N. L. Kelleher, L. L. Kiessling, N. J. Krogan, M. R. Larsen, J. A. Loo, R. R. Ogorzalek Loo, E. Lundberg, M. J. Maccoss, P. Mallick, V. K. Mootha, M. Mrksich, T. W. Muir, S. M. Patrie, J. J. Pesavento, S. J. Pitteri, H. Rodriguez, A. Saghatelian, W. Sandoval, H. Schlüter, S. Sechi, S. A. Slavoff, L. M. Smith, M. P. Snyder, P. M. Thomas, M. Uhlén, J. E. Van Eyk, M. Vidal, D. R. Walt, F. M. White, E. R. Williams, T. Wohlschlager, V. H. Wysocki, N. A. Yates, N. L. Young and B. Zhang, *Nat. Chem. Biol.*, 2018, 14, 206–214.

7   J. Arribas, J. Baselga, K. Pedersen and J. L. Parra-Palau, *Cancer Res.*, 2011, **71**, 1515–1519.

8   H. Towbin, T. Staehelin and J. Gordon, *Proc. Natl. Acad. Sci. U. S. A.*, 1979, **76**, 4350–4354.

9   W. N. Burnette, *Anal. Biochem.*, 1981, **112**, 195–203.

10   T. T. Lee and E. S. Yeung, *Anal. Chem.*, 1992, **64**, 3045–3051.

11   T. M. Olefirowicz and A. G. Ewing, *J. Neurosci. Methods*, 1990, **34**, 11–15.

12   A. J. Dickinson, P. M. Armistead and N. L. Allbritton, *Anal. Chem.*, 2013, **85**, 4797–4804.

13   A. J. Hughes, D. P. Spelke, Z. Xu, C.-C. Kang, D. V Schaffer and A. E. Herr, *Nat. Methods*, 2014, **11**, 455–464.

14   E. Sinkala, E. Sollier-Christen, C. Renier, E. Rosàs-Canyelles, J. Che, K. Heirich, T. A. Duncombe, J. Vlassakis, K. A. Yamauchi, H. Huang, S. S. Jeffrey and A. E. Herr, *Nat. Commun.*, , DOI:10.1038/ncomms14622.

15   K. A. Yamauchi and A. E. Herr, *Microsystems Nanoeng.*, 2017, **3**, 16079.

2. Rapid electrotransfer probing for improved detection sensitivity in in-gel immunoassays

2.1 Introduction

Proteins are key drivers of a range of biological processes,[1] and protein quantification from biological samples is an important metric for understanding cell and tissue state.[2] Protein detection can be accomplished by in-gel immunoassays, in which proteins are immobilized to a hydrogel matrix for subsequent immunoprobing. In-gel protein immobilization can also provide structural integrity to a biological sample, assess protein localization, and perform protein sizing.[3,4,5,6,7] Probing in-gel immunoassays involves (i) probe loading into the immunoassay gel, (ii) in-gel probe incubation for equilibrium immunocomplex formation, and (iii) unloading of unbound probe from the immunoassay gel (Figure 1A-C).[8] The concentration of immunocomplex remaining at time of assay readout is dependent on the concentration of probe loaded in-gel ($[Ab]_{gel}$; mol·m⁻³) and the immunocomplex dissociation during unbound probe unloading. In a bimolecular system, the equilibrium immunocomplex formation ($[AbAg]_{max}$; mol·m⁻³) in step (ii) is dependent on $[Ab]_{gel}$ by[9]

$$\frac{[AbAg]_{max}}{[Ag]_{gel}} = \frac{1}{1 + \frac{K_D}{[Ab]_{gel}}} \qquad (1)$$

where $[Ag]_{gel}$ is the target protein concentration, and K_D (m³·mol⁻¹) is the equilibrium dissociation constant (Figure 1D). In the absence of new binding events, $[AbAg]_{max}$ dissociates during step (iii) according to the dissociation rate constant (k_{off}; s⁻¹)[9]

$$\frac{[AbAg]_t}{[AbAg]_{max}} = 1 - exp(-k_{off}t) \qquad (2)$$

where $[AbAg]_t$ (mol·m⁻³) is the immunocomplex remaining at time t (s) (Figure 1E).

In diffusive probe loading from free-solution to a hydrogel, the in-gel probe concentration is highly dependent on the gel pore size compared to the probe size.[10,11] Small pores relative to the size of the probe impedes diffusive probe loading to a hydrogel. At equilibrium, diffusively loaded $[Ab]_{gel}$ is less than the free-solution probe concentration ($[Ab]_{sol}$) due to size-exclusion partitioning. The ratio of $[Ab]_{gel}$ to $[Ab]_{sol}$ at equilibrium is the probe partition coefficient (K_{part}). In hydrogels that use small gel pores (10-100 nm) to separate proteins by size, $K_{part} < 0.2$ has been observed[3,12] for large antibody probes (hydrodynamic radius ~5 nm)[13] diffusively loaded into the hydrogel.
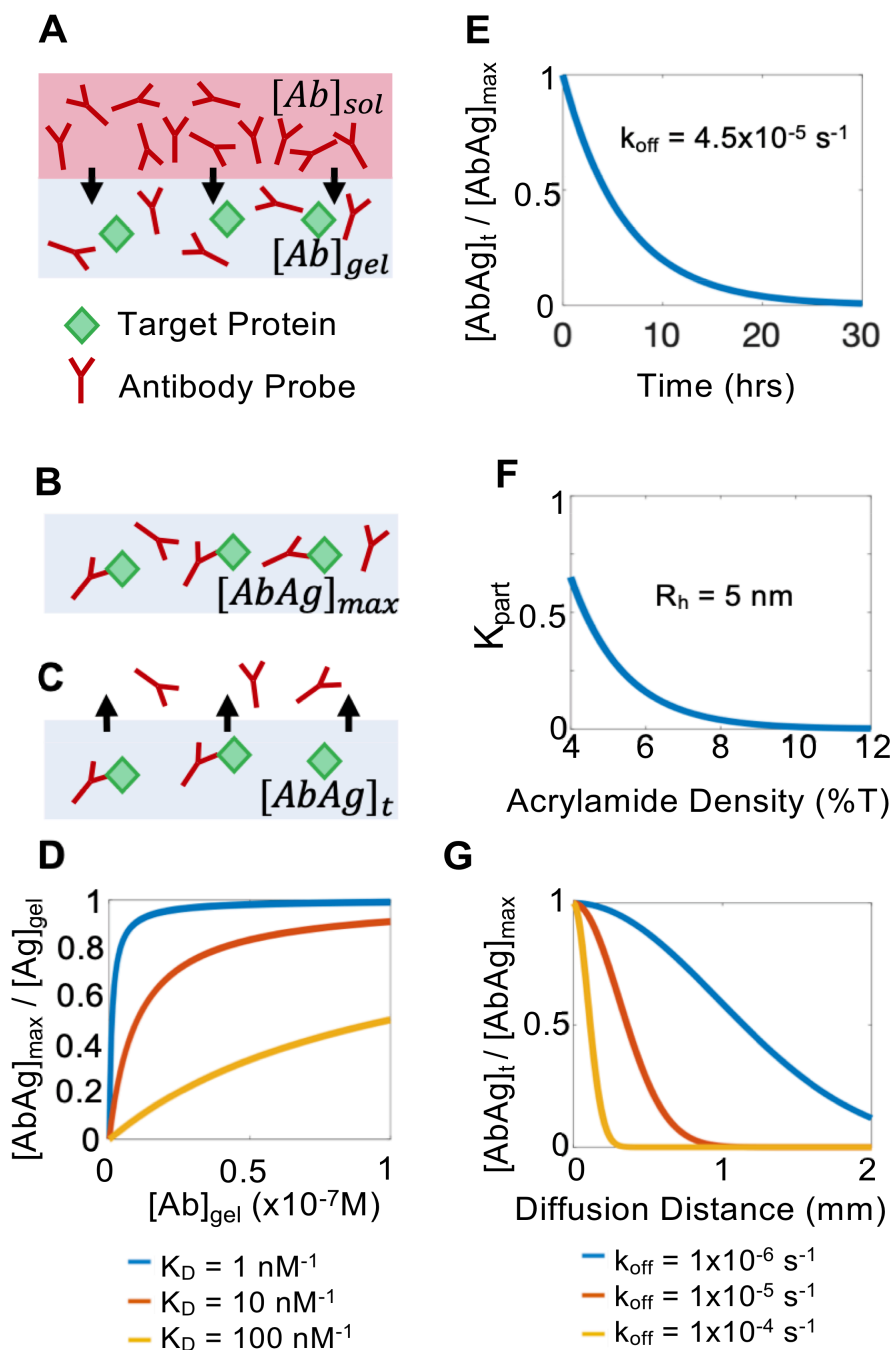
Figure 1. Immunocomplex remaining at time of assay readout is reduced by long probe diffusion distances and small pore-gel size ratio. (**A**) Probe loading into an immunoassay gel (shown in light blue). (**B**) In-gel probe incubation for equilibrium immunocomplex formation. (**C**) Unloading of unbound probe from the immunoassay gel. (**D**) Equilibrium immunocomplex formation, $[AbAg]_{max}$, is maximized by increasing concentration of antibody probe in-gel, $[Ab]_{gel}$. (**E**) Substantial immunocomplex dissociation occurs over hours-long timescales for medium dissociation rate constant, k_{off}. (**F**) Antibody probe partition coefficient, K_{part}, is reduced below 0.25 for polyacrylamide protein sizing gels (7-12%T, 2.7%C). (**G**) Substantial immunocomplex dissociation occurs over a range of k_{off} values during time required for diffusive probe unloading of millimeter scale protein sizing gels (7%T, 2.7%C).

To decouple the gel pore size demands for protein sizing from the gel requirements for effective probe loading ($K_{part} \sim 1$), target proteins in western blotting are electrotransfered from a small-pore protein sizing gel to a large-pore blotting membrane (e.g. nitrocellulose or PVDF, 200-450 nm pores).[14,15,16,17,18] However, while performing protein sizing and immunoprobing in separate materials allows for pore sizes to be independently optimized for each step, target protein can be lost from the assay by incomplete gel-membrane electrotransfer (total protein mass captured by membrane less than protein mass in gel).[14] The extent of protein mass loss in gel-membrane electrotransfer is also target specific, complicating analyte quantification.[14] Additionally, protein sizing separation resolution is reduced by diffusive broadening of separated protein bands during electrotransfer.[14,17] By minimizing protein diffusive broadening and loss timescales, protein size characterizations from single-cells have been performed using in-gel protein immobilization.[3] In-gel protein immobilization has also made possible 3-D protein localization in tissue through hydrogel-tissue hybrid immunoassays.[4,5]

To preserve advantages of performing immunoassays in-gel, a class of diffusive probe loading techniques increases equilibrium in-gel probe concentration, and thus K_{part} , by leveraging electrostatic interactions between charged molecules and charged hydrogels,[19] dehydrating in-gel immunoassays prior to probe loading,[8] and forming bi-phasic systems using salts and PEG.[20] While importantly biasing the probe partitioning equilibrium towards the hydrogel, these methods do not expedite unloading of unbound probe. The time over which immunocomplex dissociates during probe unloading thus remains unchanged.

Electrophoretic probing has been demonstrated in microcapillary gel systems as a method for both overcoming size-exclusion partitioning and rapidly loading and unloading probe compared to diffusive probe transfer.[21,22] These important demonstrations of electrophoretic probing have been shown to improve immunoassay sensitivity, including in small-pore, protein sizing in-gel immunoassays.[21] However, the applicable assay designs have been confined to enclosed microchannels and capillaries, increasing complexity of assay design, limiting sample throughput, and requiring unique microchip probe reservoir design for each microchannel immunoassay. In contrast to encapsulated microchannels, 'open' microfluidic systems remove constraints to biological samples and pre-processing steps by eliminating at least one confining boundary of the fluid sample.[23,24,25] Sample fluid accessibility is also facilitated in open devices by featuring at least one liquid-liquid or liquid-vapor interface. A generalized electrophoretic probing system that can be widely applied to millimeter-scale, open planar format in-gel protein sizing immunoassays[7] has not yet been demonstrated.

Here, we introduce a generalized electrotransfer probing platform for improved detection sensitivity of open, millimeter-scale, small-pore protein sizing in-gel immunoassays compared to diffusive probing. The platform builds on principles of gel-membrane electrotransfer used in conventional western blotting, but critically electrotransfers probe (instead of target protein) from an inert, large-pore gel to an in-gel immunoassay. We evaluated our design in comparison to diffusive probing by investigating maximum probe loading and unloading, and timescales for achieving maximum probe loading and unloading in a protein sizing gel. Finally, we demonstrate electrotransfer probing for significantly improved in-gel immunoassay signal-to-noise ratio (SNR)

in substantially less time (compared to diffusive probing) by using detection of OVA immobilized in a protein sizing gel as a model system.

2.2 Experimental Section

Polyacrylamide gel fabrication

Polyacrylamide (PA) gel was used as the molecular sieving matrix, the 20%T PA gels (used in the probe electrophoretic mobility characterization experiments), and the 4%T PA loading gel. The sizing gels were fabricated in moulds that consisted of a glass slide (VWR), a silicon wafer with SU-8 3050 (Microchem) photolithographically-micropatterned features, and two 1 mm thick shims (C.B.S. Scientific Gel Wrap). The glass slide and silicon wafer were separated by the 1 mm thick shims. To pattern a face of the sizing gel with microwell features, SU-8 features were patterned on the silicon wafer by photolithography as previously described.[26] SU-8 features were cylindrical microposts 40 μm in height, 32 μm in diameter and spaced 100 μm apart (center-center feature spacing). To mitigate gel adhesion, the SU-8 layer was coated with dichlorodimethylsilane (No. 440272, Sigma-Aldrich) and the glass slide was treated with Gel Slick® (No. 50640, Lonza). The 20%T PA gels were fabricated between a glass slide and a glass plate (McCormick). The 20%T PA gels and the 4%T PA loading gels were fabricated in moulds that consisted of a glass slide, a glass plate (McCormick), and two 1 mm thick shims. The glass slide and glass plate were separated by the 1 mm thick shims. The glass slide and glass plate were both treated with Gel Slick®. No features were patterned on the 20%T PA gels or 4%T PA loading gels.

Fabrication conditions for PA gels are described in Table S1. The sizing gels were co-polymerized with N-[3-[(3-Benzoylphenyl)-formamido]propyl] methacrylamide (BPMA) to immobilize protein in-gel.[3,26] BPMA can immobilize proteins to the gel matrix by covalently binding to proteins in-gel upon exposure to ultraviolet light.[27] All PA gels were chemically polymerized for 60 min using ammonium persulfate (APS; No. A36778, Sigma-Aldrich) and TEMED (No. T9281, Sigma-Aldrich). PA gel precursor solutions were degassed and sonicated for 5 min before chemical initiators were added. To cast the sizing gel to the fabrication mould, first, the 1 mm thick shims were affixed with adhesive tape to the SU-8 coated silicon wafer. Then, the PA precursor solution was then pipetted onto the SU-8 mould in the gap between the shims (Figure S1A). Next, a glass slide was placed on top of the shims to mould the PA gel precursor solution between the glass slide, the SU-8 coated silicon wafer, and the shims (Figure S1B). After the PA gel polymerized (60 min), the gels were released from the fabrication moulds by sliding a razor between the glass slide and the silicon wafer (in sizing gel fabrication) or the glass plate (in 20%T PA gel and 4%T PA loading gel fabrication) (Figure S1C) and used as a lever to lift the glass slide from the mould. Finally, the 1 mm thick polymerized PA gels were then trimmed with a razor to the dimensions described in Table S1 (Figure S1D). PA gels were equilibrated in Electrotransfer Buffer (Table S2) at 4 °C for at least 12 h and up to 4 days prior to use.

Probe loading gel fabrication

The loading gel was cast from a mixture of molten 1.5% w/v Ultrapure Low Melting Point Agarose (No. 16520050, Invitrogen) dissolved in 1X Tris-glycine (No. 1610734, Bio-Rad) and fluorescently-labelled antibody (Ab) probe. The sizing gels were fabricated in moulds that consisted of a glass slide, a glass plate, and two 1 mm-thick shims. The glass slide and glass plate were separated by the 1 mm-thick shims.

Fabrication conditions for the loading gels are described in Table S3. To cast the loading gel to the fabrication mould, first, the fabrication mould was assembled: (i) the 1 mm thick shims were affixed with adhesive tape to the glass plate, (ii) the glass slide was affixed with adhesive tape on top of the shims, and (iii) the glass plate was placed on a hotplate and heated to ~35-40 °C (Figure S2A). Temperature measurements were performed by infrared thermometry. Then, the molten mixture of 1.5% w/v agarose and probe was prepared: (i) probe solution was added to a 1.5 mL Eppendorf tube that was warmed to ~35-40 °C on a hot plate (Figure S2B), and (ii) ~40-50 °C molten agarose was added to the antibody probe solution and mixed by pipetting (Figure S2C). Temperatures were optimized to maintain molten state of agarose without exceeding maximum temperature of the probe thermal stability range. Ultrapure Low Melting Point Agarose remains fluid at 37 °C and sets rapidly below 25 °C. IgG antibodies exhibit conformational stability at temperatures <55 °C.[28] Next, the loading gel was cast by pipetting the molten mixture of agarose gel and probe into the fabrication mould (Figure S2D). After casting the loading gel, the loading gel was cooled to gelate by transferring the fabrication mould to an ice pack (Figure S2E). After gelation, the fabrication mould was transferred to a flat surface at ~20 °C, and the loading gel was released from the fabrication mould and trimmed by the same process used for PA gel release and trimming (Figure S2F,G). Finally, the loading gels were dipped in Electrotransfer Buffer and used immediately.

Gel sandwich assembly for electrotransfer probing
To load probe by electrotransfer to a sizing gel, a gel-gel sandwich was made using the loading gel, the sizing gel, two western blot filter paper pieces (1mm thick; No. 84783, Thermo Fisher Scientific), a custom-fabricated acrylic clamp and plastic elastomers. The clamp fabrication is described below in the subsection *Acrylic clamp fabrication.* The filter paper pieces were cut to 55 mm width x 85 mm height to match the clamp dimensions and equilibrated in Electrotransfer Buffer for 5 min prior to assembling the sandwich.

To assemble the gel-gel sandwich used in probe loading, first, the sizing gel was placed on a filter paper piece (Figure S3A). Then, the loading gel was placed on top of the sizing gel without trapping air bubbles in the fluid layer between the gels (gel x-y faces in contact; Figure S3B). Next, the second filter paper piece was placed on top of the loading gel (the edges of the two filter paper pieces were aligned when placing the second filter paper; Figure S3C). The filter paper - gels - filter paper stack was then transferred into the acrylic clamp (Figure S4), and the assembly was compressed together using polymer elastic bands (Scünci Polybands).

To unload probe by electrotransfer from a sizing gel, the same sandwich assembly process that was performed for probe loading was followed, but with the omission of the loading gel. Thus, the sizing gel was placed on a filter paper piece, and the second filter paper piece was placed on top of the sizing gel. The filter paper - sizing gel - filter paper assembly was transferred into the clamp and compressed using plastic elastomers.

Acrylic clamp fabrication
To compress the gel sandwiches used for electrotransfer probing, and suspend the gel sandwiches in the buffer chamber of a slab-gel electrotransfer system, an acrylic clamp was designed and fabricated. Individual clamp components were designed in Adobe® Illustrator® and cut from

acrylic sheets (3.175 mm thick acrylic sheets, clear; No. FJ-63961240, Astari) using a laser cutter (laser cutter printing software: RetinaEngrave3D; laser cutter: No. HL40-5G-110, Full Spectrum Laser). The individual components of the clamp were affixed together with super glue. The assembled clamp consisted of two identical halves that were compressed together with plastic elastomers (Figure S4A,B). The clamp was designed to position up to 6 gel sandwiches in the centre of the buffer chamber of a slab-gel electrotransfer system by hanging (and self-aligning) from the top edge of the chamber (XCell SureLock™ Mini-Cell Electrophoresis System, No. EI0001, Invitrogen; XCell II™ Blot Module, No. EI0002, Invitrogen; Figure S4C).

Probe electrotransfer conditions
To perform electrotransfer probe loading or unloading, a gel sandwich was assembled (described in subsection *Gel sandwich assembly for electrotransfer probing*), affixed with the clamp, and suspended in the buffer chamber of the slab-gel electrotransfer system. In electrotransfer probe loading, the loading gel was positioned towards the cathode (-) and the sizing gel was positioned near the anode (+) so that the negatively-charged probe molecules migrated into and through the sizing gel when the field was applied. The buffer chamber was filled with Electrotransfer Buffer, and the outer chamber was filled with ice water (Figure S4C). The entire slab-gel electrotransfer system was placed on ice. The slab-gel electrotransfer system was connected to a power supply (PowerPac High-Voltage Power Supply; No. 1645056, Bio-Rad). The power supply was set to constant voltage, and an electric field was applied. The applied electric field strength and time are described in Table S4. At the completion of electrotransfer probe loading or unloading, the power supply was turned off and the clamp was removed from the slab-gel electrotransfer system. The polymer elastics were removed from the clamp, and the gels were retrieved. The filter papers were disposed after every use, while the acrylic clamp and polymer elastic bands were rinsed in water and dried before reuse.

Semi-dry electrotransfer system
An anode and a cathode plate (both Bio-Rad Criterion anode plates with plastic housings modified to allow the electrodes to be brought into close proximity) were each attached to laser-cut plastic alignment casings (Figure S5A).[29] The electrode plates were separated by 3 mm shims placed on either side of the electrode surface and magnetically brought into contact (Figure S5B). The semi-dry electrotransfer system was connected to a power supply (Bio-Rad PowerPac Basic).

Probe electrophoretic mobility characterization
To characterize the probe μ_{gel} in a sizing gel, the electromigration of a discrete probe band using the slab-gel electrotransfer system was monitored. The semi-dry electrotransfer system was first used to electrophoretically inject probe from a free-solution layer between a sizing gel and a 20%T PA gel into the sizing gel (Figure S5D-F). The semi-dry electrotransfer system was connected to a power supply. The power supply was set to constant voltage and an electric field of 100 V/cm was applied for 30 s. After the power supply was turned off, the semi-dry electrotransfer system was dissasembled and the sizing gel was retrieved. A filter paper – sizing gel – filter paper sandwich was then assembled, and the sandwich was transferred into the acrylic clamp as described in subsection *Gel sandwich assembly for electrotransfer probing*. Finally, the clamped gel sandwich was inserted to the slab-gel electrotransfer system and probe x_E was monitored (sizing gel microwell-patterned face aimed towards the cathode; electric field = 12 V/cm, applied time = 30s, 60s, 120s, 180s, 240s, 300s). Probe electromigration distance was recorded for each

electrotransfer time, and a least-squares linear-regresion fit was applied to determine the in-gel probe electrophoretic mobility.

Gel sandwich assembly for diffusive transfer probing
To load probe by diffusive transfer to a sizing gel, a gel sandwich was made using two loading gels and a sizing gel. First, a sizing gel was trimmed to final x-y-z dimensions: 5-5-1 mm. The loading gels were then trimmed to final x-y-z dimensions: 7-7-1 mm. Then, a sizing gel was placed on top of a loading gel (gel x-y faces in contact). Next, a second loading gel was placed on top of the sizing gel. The three-gel sandwich was then stored in a dark, humid chamber (single well of a 96-well plate) at 4 °C. No air bubbles were trapped between the gel layers during sandwich assembly. To unload probe by diffusive transfer, a probe loaded gel was placed in a single well of a 96-well plate. The well was filled with Electrotransfer Buffer (~300 μL), and buffer was refreshed every 6 h. The 96-well plate was stored in the dark at 4 °C. Times of diffusive probe transfer are described in Table S5.

OVA in-gel immobilization and probing
A solution of ovalbumin labelled with AlexaFluor® 488 (OVA, diluted to 5 μM in 1X Tris-glycine; No. 034783, Thermo Fisher Scientific) was electrophoretically injected into a sizing gel and immobilized in-gel. To electrophoretically inject OVA, the custom semi-dry electrotransfer system was used (system and sample assembly described in the subsection *Probe electrophoretic mobility characterization*). All gels were equilibrated in 1X RIPA buffer (instead of Electrotransfer Buffer; Table S2) immediately after fabrication at 4 °C for at least 12 h and up to 4 days prior to use. The filter paper was also equilibrated in 1XRIPA buffer (instead of Electrotransfer Buffer). After assembling the semi-dry electrotransfer system, a 35 mA constant current was applied for 15 s. Once the power supply was turned off, the system was disassembled and the sizing gel was exposed to UV light for 45 s to photocapture OVA to the BPMA-functionalized sizing gel as previously described.[27] Next, the sizing gel was incubated in Electrotransfer Buffer at 4 °C for at least 12 h to exchange buffers and unload unbound OVA (dark, 4 °C). In-gel immobilized OVA was probed by electrotransfer and diffusive transfer using 1° and 2° Ab probes (probes described in Table S3; probe transfer conditions described in Tables S4 and S5). Between each probe loading and unloading step, the sizing gel was incubated in a humid chamber for equilibrium immunocomplex formation (dark, ~20 °C). Incubation times for electrotransfer probing were informed by existing hydrogel immunoassay devices (1 °Ab incubation: 2 h; 2 °Ab incubation: 1 h).[3] In summary, the full 1° and 2° Ab probing sequence included: (i) 1°Ab probe loading, (ii) OVA-1°Ab probe equilibrium immunocomplex formation (2 h), (iii) 1°Ab probe unloading, (iv) 2°Ab probe loading, (v) 1°Ab-2°Ab probe equilibrium immunocomplex formation (1 h), and (vi) 2°Ab probe unloading.

Imaging and analysis
Image capture was performed with MetaMorph® imaging software (Molecular Devices) using an Olympus IX51 inverted widefield fluorescence microscope fitted with an Olympus UPlanFLN 4X objective (No. UPLFLN4X) and an X-Cite® illumination source (Excelitas Technologies), CoolSNAP™ HQ2 CCD camera (Teledyne Photometrics), GFP filter set (Chroma 49011 ET), DAPI filter set (Chroma 4900), and TRITC filter set (Chroma 41002c).

Image acquisition of in-gel fluorescence resulting from probe loading and unloading was performed by placing the sizing gel on a 65mm Petri dish (10-10 mm gel x-y face in contact with the Petri dish). The microscope plane of focus was adjusted to the middle-depth of the 1 mm sizing gel. Average in-gel fluorescence was calculated. Background subtraction was performed by subtracting the average in-gel fluorescence of gels with no exposure to fluorescent probe molecules from the average in-gel fluorescence of test group gels. Effective partition coefficients were calculated as the ratio of the average in-gel fluorescence of the sizing gel after loading over the average in-gel fluorescence of the loading gel after fabrication (effective partition coefficient determined following this calculation for both electrotransfer and diffusive probe loading). For probe loading by diffusive transfer, a Power Law[30,31] model for total probe mass loading was fit to in-gel fluorescence timepoint measurements using MATLAB®. In MATLAB, the fit() function and a custom-defined equation to model Power Law probe loading was used (Figure 4B)

$$Fluorescence\ in\ gel = \frac{[Ab]_t}{[Ab]_\infty} = a * t^b \qquad (3)$$

where $[Ab]_t$ is probe mass in gel at time t, $[Ab]_\infty$ is the probe mass in gel at equilibrium, a is a structural constant of the gel, and b is a release exponent.[30,31] Model fit paramters were: $a = 104.1$, $b = 0.1992$, $r^2 = 0.9321‡$.

To calculate probe unloading, the average in-gel fluorescence after unloading was normalized to the average in-gel fluorescence after loading. For probe unloading by diffusive transfer, a Power Law[30,31] model was fit to in-gel fluorescence timepoint measurements using MATLAB®. In MATLAB, the fit() function and a custom-defined equation to model Power Law probe unloading was used (Figure 5B)

$$Fluorescence = \frac{[Ab]_t}{[Ab]_\infty} = 1 - a * t^b \qquad (4)$$

where $[Ab]_t$ is probe mass in gel at time t, $[Ab]_\infty$ is the probe mass in gel at equilibrium, a is a structural constant of the gel, and b is a release exponent.[30,31] Model fit paramters were: $a = 0.1766$, $b = 0.4236$, $r^2 = 0.9812$.

To image probe peak location in the probe electrophoretic mobility characterization, and the immobilized OVA and probed signal peak locations in the OVA immunoprobing experiments, a razor was used to cut a 0.5 mm sliver of the sizing gel (10mm x ~0.5mm x 1mm in x-y-z; Figure S6A). The sizing gel sliver was laid on a 65 mm Petri dish (10 mm x 1 mm sliver x-z face in contact with the Petri dish (Figure S6B). Fluorescence profiles in the z-axis were computed by averaging fluorescence intensities across ~2 mm image region in the x-axis at each z-axis depth (Figure S6B for axis orientation). Averaged fluorescence profiles were fit with Gaussian curves to determine peak location (MATLAB®, fit() function, 'gauss1' fit model, region analysed: peak location ± 3σ). Background subtraction performed by subtracting the average pixel value in the 3σ to 4σ region (defined as background) from the pixel values in the peak location ± 3σ region

(defined as signal). Background noise for determining SNR values of probed signal was calculated by taking the standard deviation of the fluorescence intensity between the 3σ and 4σ bounds of the fluorescence profiles. Peak location was determined by the peak location of the Gaussian fit.

2.3 Results and Discussion

Electrolytic cell design for electrotransfer probing
To improve the in-gel immunoassay detection sensitivity determined by diffusive probe transfer, we sought to address the following immunoprobing design criteria: (i) near complete probe loading ($K_{part} \sim 1$) and unloading in a hydrogel, and (ii) rapid probe loading and unloading in a hydrogel compared to immunocomplex dissociation timescales. PA protein sizing gels designed with 10-100 nm average pore radii are used to resolve proteins with molecular weights of ~10-90 kDa,[32] corresponding to hydrodynamic radii (R_h) of ~1.5-4.0 nm.[33] Size-exclusion partitioning of diffusively loaded probe to hydrogels reduces the equilibrium K_{part} of the probe, and can be approximated using Ogston's model[10,11]

$$K_{part} = \frac{[Ab]_{gel}}{[Ab]_{sol}} = \exp\left(-\phi\left(1 + \frac{R_h}{a_f}\right)^2\right) \qquad (5)$$

where ϕ is the volume fraction of polymer in the gel, and a_f (nm) is the polymer fiber radius of the gel. The average pore size of a gel is related to ϕ through a negative exponential relationship.[34] Thus, increasing ϕ causes exponential decreases in average gel pore size and K_{part}. For gel fabrication, ϕ is linearly related to total acrylamide monomer density (%T), and gel %T can be tuned to control gel pore size (for fixed percent bis-acrylamide cross-linker, %C). When using large antibody probes (150 kDa, $R_h \sim 5$ nm)[13] to diffusively probe protein sizing hydrogel (7-12%T, 2-5%C), $[Ab]_{gel}$ can be an order of magnitude lower than $[Ab]_{sol}$ (Figure 1F).[3,6,7,35]

Long diffusive probe unloading timescales compared to immunocomplex dissociation reduces the concentration of immunocomplex remaining at time of assay readout.[36] The expected 1-dimensional probe diffusion distance, $\langle x_{Diff} \rangle$ (μm), is linearly related to the square-root of time given by[34,37]

$$\langle x_{Diff} \rangle = \sqrt{2D_{\%T}t} \qquad (6)$$

$$D_{\%T} = D_{sol}\exp\left(-3.03\,R_h^{0.59}\,\%T^{0.94}\right) \qquad (7)$$

where $D_{\%T}$ (μm^2·s^{-1}) is the in-gel diffusion coefficient of the probe, D_{sol} is the free-solution diffusion coefficient of the probe. An analytical model shows that in the time required for antibody diffusion across 1.2 mm of a 7%T, 2.7%C PA gel to occur (~53 h), <50% of initial immunocomplex will remain intact for antibodies with $k_{off} > 10^{-6}$ s^{-1} (Figure 1G).

In contrast to diffusive probe migration, probe electromigration velocity (v; $\mu m \cdot s^{-1}$) is linearly proportional to strength of applied electric field (E; $V \cdot cm^{-1}$)

$$v = \mu_{gel} E \qquad (8)$$

$$\mu_{gel} = \frac{q}{6 \pi \eta R_h} 10^{-K_r \, \%T} \qquad (9)$$

where q (C) is the molecule net charge, η ($Pa \cdot s^{-1}$) is the solution viscosity, K_r is the gel retardation coefficient, and μ_{gel} ($cm^2 \cdot V^{-1} \cdot s^{-1}$) is the in-gel electrophoretic mobility of the probe. E thus provides a tuneable parameter to expedite probe electromigration and increase K_{part} (compared to diffusive probing) without altering gel pore size.[38] Additionally, the probe electromigration distance (x_E; μm) is linearly related to t, whereas $\langle x_{Diff} \rangle$ is linearly related to the square-root of t ($x_E \sim t$; $\langle x_{Diff} \rangle \sim \sqrt{t}$).[39]

$$x_E = \mu_{gel} E t \qquad (10)$$

We thus designed an electrotransfer probing platform to satisfy the design criteria of increased K_{part} and expedited probe transfer compared to diffusive probing. In electrotransfer probing: (i) probe is loaded to a small pore sizing gel (7%T, 3.5%C PA gel, pore radius ~40-87 nm[40]) by electrotransfer from an inert, large pore probe loading gel (1.5% w/v agarose, pore radius ~100-150 nm[41]), (ii) probe is incubated in the sizing gel to reach immunocomplex equilibrium, and (iii) probe is unloaded by electrotransfer from the sizing gel (Figure 2A-C). Our system involves sandwiching the loading gel and sizing gel together, and performing probe electrotransfer in an electrolytic cell using a conventional slab-gel electrotransfer system to supply uniform electric field across the gel. We designed an inert, large pore loading gel to facilitate electrotransfer of
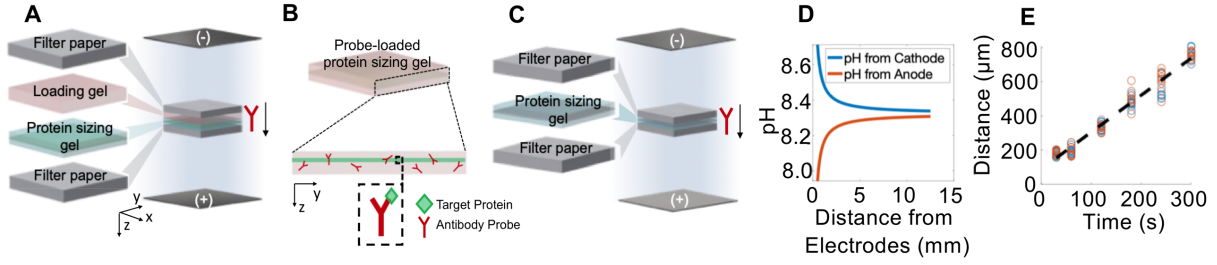
Figure 2. Electrotransfer probing facilitates predictable probe electromigration without direct visualization. (**A**) Probe Loading: A sandwich of filter papers, a loading gel, and a protein sizing gel is submerged in a buffer volume. Probe is loaded to the sizing gel by electrotransfer. (**B**) Equilibrium Immunocomplex Formation: The probe-loaded sizing gel is removed from buffer volume for equilibrium immunocomplex formation. (**C**) Probe Unloading: A sandwich of filter papers and the sizing gel is submerged in a buffer volume and unbound probe is unloaded from the sizing gel by electrotransfer. (**D**) pH stability at the center of electrolytic cell is predicted by modeling analysis of pH resulting from applied current to electrotransfer probing system. The gel sandwiches are located at the center of the 2.5 cm wide electrolytic cell (12.5 mm from each electrode). (**E**) Probe electromigration distance is linearly related to time ($r^2 = 0.9888$, least-squares linear-regression model). Five trials were performed at varied electromigration times (t = 30s, 60s, 120s, 180s, 240s, 300s) using two gels per trial (separate gels are colour-coded). No significant difference was observed across individual gels used in each trial (p > 0.22, Mann-Whitney U-test).

nearly all antibody probe mass from the loading gel to the sizing gel. We evaluated timescales of electrotransfer probe loading and unloading, and mass of probe loaded and unloaded in a sizing gel. Finally, we investigated the impact of electrotransfer probing on the detection sensitivity of a protein sizing in-gel immunoassay in a proof-of-concept demonstration by immunoprobing for in-gel immobilized OVA.

Electrotransfer probing design mitigates the negative impacts of electrolysis products on electromigration performance

To predict probe loading and unloading in a hydrogel by electrotransfer without direct visualization of probe location, the relationship between x_E, E, and t given by Equation 10 can be used as long as key parameters such as q and E remain constant. In designing the electrotransfer probing system, we considered that unpredictable or poorly reproducible in-gel electromigration within an electrolytic cell (not adhering to Equation 10) can result from the gas and ionic products of the electrolysis reactions occurring at the electrode surfaces:[42]

$$Cathode: 2H_2O_{(l)} + 2e^- \leftrightarrow 2OH^-{}_{(aq)} + H_{2(g)} \quad (11)$$

$$Anode: H_2O_{(l)} \leftrightarrow 2e^- + 2H^+{}_{(aq)} + \frac{1}{2}O_{2(g)} \quad (12)$$
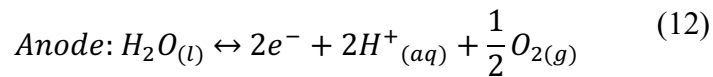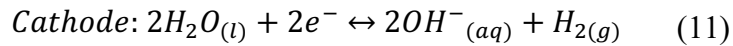
Specifically, the gas bubble products of electrolysis can obstruct the electric field path, and cause time-variable voltage drops (and thus E) across gels.[43] To remove electrolysis gas bubbles from the path of the applied E, a conventional slab-gel electrotransfer chamber was custom-fit with an

20

acrylic gel clamp (Figure SI1). The clamp facilitated bubble removal from the E path by including an open buffer solution – air interface, permitting bubbles to float to the surface of the buffer volume as they are generated.

Deviations from theoretical electromigration behavior (Equation 10) can also result from the strong base (OH-) and strong acid (H+) products of electrolysis. The strong base and acid products can cause sharp pH changes near the electrode surfaces, specifically making the solution near the cathode more basic and the solution near the anode more acidic.[42,44] This phenomenon has been well reported in similar systems, particularly for capillary electrophoresis[42] and has even been applied to form natural pH gradients in isoelectric focusing systems.[44] Such pH variation can cause changes in μ_{gel} by altering the probe q (Equation 9).[45]

A previously established modelling framework[42] predicted pH in buffer solution as a result of applied E and t (total charge delivered). Briefly, total charge delivered from electrodes to solution was calculated using Faraday's law of electrolysis from applied electric current intensity and duration. The total charge delivered was used to calculate the change in [H+] or [OH-] (from surface of anode or cathode, respectively) in solution, and the ion concentration change was used along with initial buffer ion concentrations and buffer pKa to calculate system pH. System pH was then reported as a function of the distance from each electrode surface (where the total number of buffering species available to mitigate pH change is a function of increasing buffer volume). The results of this modeling analysis are included in Figure 2D, which shows the expected pH as a function of distance from each electrode surface in this system. For a 1X-Tris-glycine buffer volume with dimensions 10 cm x 10 cm x 2.5 cm (width x height x depth, 250cm^3 total volume) the center 1 mm between the electrodes (distance between opposite faces of the sizing gel) experiences minimal pH changes (0.031 difference in pH, within the variability of 1X Tris-glycine made from commercially available stock solution[46] and below the resolvable pI difference demonstrated in single-cell isoelectric focusing technologies[47]). Thus, we designed a system in which gas products of electrolysis could be passively removed and ionic products would cause negligible pH changes (as suggested by modeling analysis).

Probe electromigration distance is linearly dependent on time in electrotransfer system
We next sought to experimentally demonstrate that probe x_E responds linearly with t, and calculate the probe μ_{gel} in our system. To monitor probe x_E, probe was electrophoretically injected into the gel from free-solution using a custom made semi-dry electrotransfer system (Figure S5). The probe sample underwent electrophoretic sample stacking (lower probe μ_{gel} than probe free-solution electrophoretic mobility, Equation 9). Because the probe solution initially formed a thin layer and underwent sample stacking, the width of the probe band in-gel (Gaussian fit, $\pm 3\sigma$) was less than the gel thickness. The location of the migrating probe band was tracked by fitting a Gaussian curve to identify the probe peak location. The in-gel x_E of the probe band in the electrotransfer probing system was then characterized over t.

A linear relationship between probe x_E and t in electromigration was determined using a least-squares linear-regression model ($r^2 = 0.9888$, Figure 2E). The probe v for the applied E was extracted from the slope of the linear fit ($v = 2.17$ μm/s) and the $\mu_{7\%T}$ for the probe in this system was determined using Equation 8; $\mu_{7\%T} = 1.81$ x 10^{-5} cm^2/(V·s). No significant difference in x_E

across gels was observed, facilitating prediction of probe location in-gel without real-time visualization of probe location (p > 0.22, Mann-Whitney U-test; Figure 2E).

Electrotransfer yields near-complete probe release from an agarose loading gel

To maximize utility across a range of in-gel immunoassays, we designed the probe loading gel with two key traits: (i) rapid fabrication and assembly with minimal handling, and (ii) efficient probe release (minimal probe entrapment in loading gel) to maximize the amount of probe available for loading into the immunoassay gel. We hypothesized that an inert hydrogel with large pores (100-1000 nm pore radius) could be used as a probe loading gel to satisfy these two design criteria. We thus used a 1.5% low melting point agarose gel as a model probe loading gel (Figure S2).[48] To assess probe release efficiency, we then compared probe release from an agarose loading gel to probe release from a 4%T PA loading gel. Electrotransfer parameters were chosen for a calculated probe $x_E > 1500$ μm, whereas the loading gel thickness was 1000 μm (Equation 10; Figure 2E).

Figure 3. Unbound probe entrapment in loading gels after unloading by electrotransfer (12 V/cm, 12 minutes). Loading gels were fabricated with 0.2 mg/ml Donkey anti-Rabbit AF647 antibody included in molten (1.5% w/v agarose gel) or unpolymerized (4%T, 3.5%C PA gel) states. Pre-unloading: n=9. PA gel Post-unloading: n=6. Agarose Post-unloading: n=3. Error bars indicate standard deviation. (*indicates statistical difference by Mann-Whitney U-test, p<0.0238*)

After unloading, the fluorescence remaining in the agarose loading gel was 3.93% ± 1.76% of the initial in-gel fluorescence (error reported as standard deviation, n=3, Figure 3). The fluorescence remaining in the 4%T PA loading gel was 75.8% ± 12.3% of the initial in-gel fluorescence (error reported as standard deviation, n=6, Figure 3). The agarose loading gel thus retained ~19X less probe than the PA loading gel after unloading by electrotransfer (p=0.0238, Mann-Whitney U-test).

Interestingly, the majority of the probe in the 4%T PA loading gel precursor solution remained in-gel after unloading by electrotransfer. From calculations of probe x_E for applied E and t (Equation 10), we expected probe to unload from the 4%T PA loading gel (calculated $x_E > 1500$ μm in a 7%T PA gel, and therefore also in a 4%T PA loading gel). We therefore do no attribute the observed signal to insufficient applied E or t. However, the free radical cascade resulting from chemically initiated (APS & TEMED) PA gel polymerization is known to interact with proteins that are included in PA gel precursor solutions. This interaction has been shown to cause protein denaturation in PA gels during polymerization, evidenced by western blotting analysis.[49] Additionally, incomplete macromolecule drug release from hydrogel drug-delivery devices has been observed for hydrogel devices that were polymerized with drug included in the gel precursor solution.[31,50] Probe remaining in the 4%T PA gel after electrotransfer unloading may thus be caused by similar interactions, causing denatured probe to be entropically trapped in the

pores or immobilization of the probe to the hydrogel matrix.[50] Agarose gelation does not undergo the same polymerization process and is relatively inert to proteins while transitioning from molten to solidified states[51]. The inert nature of the large-pore agarose loading gel satisfies the design criteria of both minimal probe entrapment in-gel and rapid, straightforward fabrication.

Probe is rapidly loaded with enhanced partition coefficient in electrotransfer probing
After designing a system for controllable constant-velocity probe electromigration ($r^2 = 0.9888$, Figure 2E) and minimal probe entrapment in an agarose loading gel (96.07% $\pm$ 1.76% probe removed, Figure 3A), we aimed to demonstrate this system for an increased K_{part} and rapid probe transfer from the loading gel to a sizing gel in electrotransfer probe loading (as compared to diffusive probing). To determine the expected probe x_E in the system for an applied E, the probe $\mu_{7\%T}$ calculated from Figure 2E was again used. At $E = 8$ V/cm, expected $v = 1.45$ µm/s, and the calculated t required for probe to electromigrate 1000 µm (sizing gel thickness) was ~11.5 min. Probe μ_{gel} in the 1.5% agarose loading gel is expected to be greater than in the 7%T PA sizing gel based on previous comparisons of electrophoretic macromolecule transport in the two materials (larger pore size in agarose gel permits faster macromolecule transport).[48] Because of this difference in μ_{gel} values, it is expected that probe electrotransferring from the loading gel to the sizing gel will undergo electrophoretic stacking, becoming more concentrated upon entering the sizing gel by the ratio of the two μ_{gel} values.[52] As the loading gel and the sizing gel are the same thicknesses (1 mm), we hypothesized this electrophoretic stacking to minimize the extent of probe loss from gel to the surrounding buffer solution by diffusive broadening during probe

electromigration. The mean effective K_{part} for electrotransfer probe loading was $K_{part,E} = 0.87 \pm 0.05$ (n=4, error reported as standard deviation; Figure 4A).

The duration for monitoring diffusive probe loading was informed by Equations 6 and 7. Probe diffusion over 0.5 mm in a 7%T PA gel (minimum characteristic diffusion length, as probe is loaded from both opposite faces of the 1mm thick sizing gel) is expected to occur in ~4.8 h (τ). In-gel fluorescence measurements were recorded over 28 h (>5.8 τ) of diffusive probe loading. The mean K_{part} after 28 h of diffusive transfer probe loading was $K_{part,diff} = 0.13 \pm 0.01$ (n=4, error reported as standard deviation; Figure 4A). Thus, mean effective K_{part} into the sizing gel was enhanced in electrotransfer probe loading compared to diffusive transfer probe loading by a factor of 6.5 ± 0.1 (p=0.0286, Mann-Whitney U-test).

To characterize probe loading over t by diffusive transfer, in-gel fluorescence over 28 h of diffusive probe loading was used to generate a Power Law model fit[30,31] ($r^2 = 0.9321$‡; Figure 4B). From the Power Law fit, 90% of in-gel fluorescence measured at 28 h was determined to occur at ~16 h. Electrotransfer probe loading thus not only resulted in an effective probe K_{part} that was 6.5 ± 0.1 X greater than in diffusive transfer loading, but was also demonstrated to do so >82X faster than diffusive transfer loading (electrotransfer loading time = 11.5 min).

Electrotransfer facilitates rapid, effective probe unloading

We next considered the probe fluorescence retained in the sizing gel after unloading by probe electrotransfer compared to diffusive transfer. To accomplish this, probe-loaded sizing gels were unloaded by either probe electrotransfer or probe diffusive transfer. The E and t (12 V/cm, 15 min) for removal of unbound probe was determined from $\mu_{7\%T}$ calculated in Figure 2E. Calculations estimated probe $x_E \approx 2000$ μm, thus supporting complete unloading of the sizing gel (1000 μm). After

Figure 4. (**A**) Electrotransfer probe loading results in greater partition coefficient than diffusive probe loading. Electrotransfer loading n=4. Diffusive loading n=4. (*indicates statistical difference by Mann-Whitney U-test, p=0.0286*) (**B**) Diffusive probe loading to a sizing gel occurs over hours-long timescale (n=4, separate gels are color coated).
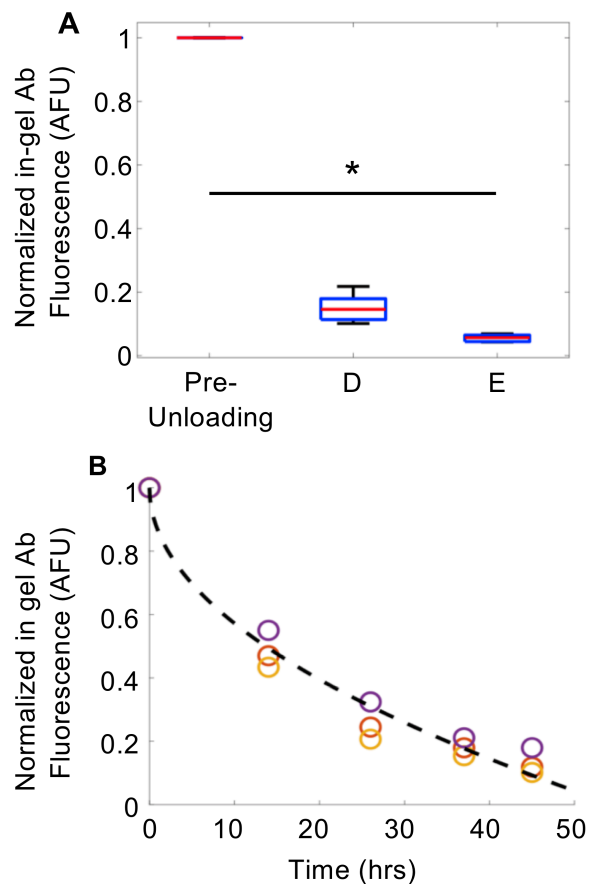
Figure 5. (**A**) Electrotransfer unloading of unbound probe results in less probe entrapment in-gel than diffusive unloading. E: electrotransfer unloading, n=5. D: diffusive unloading, n=6. (*indicates statistical difference by Mann-Whitney U-test, p<0.05*) (**B**) Diffusive probe unloading from a sizing gel occurs over hours-long timescale (n=3, separate gels are color coated).

probe unloading by electrotransfer, the fluorescence retained in the sizing gel was $5.54\% \pm 1.16\%$ (n=5, Figure 5A) of the initial probe-loaded sizing gel fluorescence. Probe unloading by diffusive transfer was expected to occur in ~4.8 h (τ; Figure 1C). After 45 h of diffusive washout (>9.7τ), we observed a mean in-gel fluorescence of $15.09\% \pm 4.62\%$ (n=6, Figure 5A) of the initial in-gel probe-loaded sizing gel.

Interestingly, in-gel fluorescence during probe unloading by diffusive transfer continued to decrease over 45 h (n=3, Figure 5B). In order to characterize probe unloading over t by diffusive transfer, the in-gel fluorescence data during probe removal were fit to a Power Law[30,31] model of diffusive probe unloading ($r^2 = 0.9812$; Figure 5B). From the Power Law fit, 90% of unbound probe was removed at ~45 h. The rate of probe removal could be potentially expedited by more regular buffer bath exchanges (e.g., twice hourly, as is done for similar antibody probe removal steps from similarly dense PA gel immunoassays[3] instead of every 12 h as was done here), or storage in warmer environment (>4 °C). Such measures were not taken in these experimental procedures as 30 min buffer exchanges over >24 hour was not deemed experimentally practical, and to prevent sample contamination or antibody denaturation by additional handling steps and storage in warm environment. Ultimately, the remaining in-gel background fluorescence resulting from probe unloading by electrotransfer was 2.7 ± 0.4 X less than probe unloading by diffusive transfer and was accomplished >180X more rapidly than unloading by diffusive transfer.

Electrotransfer probing improves immunoassay performance compared to diffusive probing
Finally, we assessed the impact of electrotransfer probing on in-gel immunoassay detection sensitivity in comparison to diffusive transfer probing. We hypothesized that applying

Figure 6. Electrotransfer probing detects in-gel immobilized OVA with greater SNR and less immunoprobing duration than diffusive probing. (**A**) Fluorescence micrographs of immobilized OVA and electrotransfer detection probe in a sizing gel. (**B**) SNR of OVA detection probe in electrotransfer probing is greater than in diffusive probing. Electrotransfer: n=6. Diffusive: n=4. *(* indicates statistical difference by Mann-Whitney U-test, p=0.0095)*. (**C,D**) Peak locations of target OVA protein and detection probe show no statistical difference in electrotransfer probing (**C**) and diffusive probing (**D**) conditions (p>0.17, *Mann-Whitney U-test*). (**E**) Immunoprobing duration is 30x shorter in electrotransfer probing than diffusive probing. E: electrotransfer probing. D: diffusive probing.

electrotransfer probing to detect OVA immobilized in a protein sizing gel would result in greater SNR and require less immunoprobing time than OVA detection by diffusive transfer probing. Fluorescence micrographs of the OVA and probe bands are shown in Figure 6A. We observed that the mean SNR in electrotransfer probing was 20.56 ± 15.60 (n=6), while that of diffusive transfer probing was 5.02 ± 1.70 (n=4, p=0.0095, Mann-Whitney U-test, Figure 6B). The SNR variability of electrotransfer probing may have been inflated by variable probe concentration in loading gels, as described in Table S3 (1° Ab probe: 0.1-0.0075 mg/mL, 2° Ab probe: 0.2-0.015 mg/mL). Loading gels used in diffusive probing did not vary in probe concentration (1° Ab probe: 0.1 mg/mL, 2° Ab probe: 0.2 mg/mL). Further experiments are required to investigate the effect of probe concentration in loading gels on SNR. An assessment of target protein peak location and detected probe peak location in electrotransfer and diffusive probing was performed to verify that the measured probe signal corresponded to the actual target protein location (p > 0.17 for both methods, Mann-Whitney U-test, Figure 6C). Notably, the total time required for completion of assay probing steps in electrotransfer and diffusive transfer probing differ greatly: the diffusive transfer probing was completed in 120 h while electrotransfer probing was completed in less than 4 h (Figure 6D). Compared to diffusive transfer probing, electrotransfer probing thus improved in-gel immunoassay detection sensitivity, marked by 4.1 ± 3.4 X greater SNR, and required 30X less immunoprobing time.

2.4 Conclusions

We introduced a gel-gel electrotransfer probing system for rapid and effective probe loading and unloading in mm-scale, dense, open in-gel immunoassays. Our design involves (i) an electrolytic cell that has been designed and characterized for predictable probe migration, and (ii) an agarose loading gel for low-loss delivery of probe to a protein-sizing gel. We demonstrated this system for faster, more effective probe loading and unloading to a large, dense, open hydrogel than possible with conventional diffusive transfer probing. We additionally evaluated the impact of electrotransfer probing on in-gel immunoassay detection sensitivity, using OVA detection from a protein sizing gel as a proof-of-concept example. Compared to diffusive transfer probing, we observed increased probed signal SNR in a substantially shorter overall immunoprobing duration. Electrotransfer probing both increased probed protein measurement SNR and required 30X less immunoprobing time than diffusive transfer probing. Given the prevalent usage of in-gel immunoassays for target protein detection from biological samples, we anticipate that electrotransfer probing will improve detection sensitivity across a wide range of in-gel immunoassays. Open questions include investigations of electrotransfer probing using alternative probe labels (e.g., fluorescent labels with varied charge). Additionally, by removing challenges to immunoprobing mm-scale protein sizing hydrogels, we anticipate electrotransfer probing to facilitate the design of novel in-gel immunoassays with expanded form-factors and enhanced precision protein characterization capabilities.

2.5 References

1   J. Berg, T. JL and S. L., in *Biochemistry*, 5th ed.

2   C. Vogel, R. D. S. Abreu, D. Ko, S. Le, B. A. Shapiro, S. C. Burns, D. Sandhu, D. R. Boutz, E. M. Marcotte and L. O. Penalva, *Mol. Syst. Biol.*, 2010, **6**, 1–9.

3   A. J. Hughes, D. P. Spelke, Z. Xu, C.-C. Kang, D. V Schaffer and A. E. Herr, *Nat. Methods*, 2014, **11**, 455–464.

4   F. Chen, P. W. Tillberg and E. S. Boyden, *Science (80-.).*, 2015, **347**, 543–548.

5   I. Costantini, J. P. Ghobril, A. P. Di Giovanna, A. L. Allegra Mascaro, L. Silvestri, M. C. Müllenbroich, L. Onofri, V. Conti, F. Vanzi, L. Sacconi, R. Guerrini, H. Markram, G. Iannello and F. S. Pavone, *Sci. Rep.*, 2015, **5**, 9808.

6   M. J. Theisen, M. L. Chu and A. Laboratories, *In-gel Immunochemical Detection of Proteins that Transfer Poorly to Membranes*, 2004.

7   S. Desai, B. Dworecki and E. Cichon, *Anal. Biochem.*, 2001, **297**, 94–98.

8   J. Vlassakis and A. E. Herr, *Anal Chem*, 2015, **87**, 11030–11038.

9   J. A. Goodrich and J. F. Kugel, *Binding and Kinetics for Molecular Biologists*, Cold Spring Harbor Laboratories Press, Cold Spring Harbor, 2007.

10   A. G. Ogston, *Trans. Faraday Soc.*, 1958, **54**, 1754–1757.

11   J. Tong and J. L. Anderson, *Biophys. J.*, 1996, **70**, 1505–1513.

12   A. Su, B. E. Smith and A. E. Herr, *Anal Chem*, 2020, 875–883.

13   T. Jøssang, J. Feder and E. Rosenqvist, *J. Protein Chem.*, 1988, **7**, 165–171.

14   D. J. MacPhee, *J. Pharmacol. Toxicol. Methods*, 2010, **61**, 171–177.

15   W. N. Burnette, *Anal. Biochem.*, 1981, **112**, 195–203.

16   H. Towbin, T. Staehelin and J. Gordon, *Proc. Natl. Acad. Sci.*, 1979, **76**, 4350–4354.

17   G. J. Anderson, C. M. Cipolla and R. T. Kennedy, *Anal. Chem*, 2011, **83**, 17.

18   S. Jin, M. D. Furtaw, H. Chen, D. T. Lamb, S. A. Ferguson, N. E. Arvin, M. Dawod and R. T. Kennedy, *Anal. Chem.*, 2016, **88**, 6703–10.

19   C. Kotsmar, T. Sells, N. Taylor, D. E. Liu, J. M. Prausnitz and C. J. Radke, *Macromolecules*, 2012, **45**, 9177–9187.

20   S. H. Gehrke, L. H. Uhden and J. F. McBride, *J. Control. Release*, 1998, **55**, 21–33.

21   R. E. Gerver and A. E. Herr, *Anal. Chem.*, 2014, **86**, 10625–10632.

22   S. N. Krylov, *Electrophoresis*, 2007, **28**, 69–88.

23   J. Berthier, K. A. Brakke and E. Berthier, *Open Microfluidics*, Wiley, 2016.

24   T. Pfohl, F. Mugele, R. Seemann and S. Herminghaus, *ChemPhysChem*, 2003, **4**, 1291–1298.

25   G. V. Kaigala, R. D. Lovchik and E. Delamarche, *Angew. Chemie Int. Ed.*, 2012, **51**, 11224–11240.

26   C.-C. C. Kang, K. A. Yamauchi, J. Vlassakis, E. Sinkala, T. A. Duncombe and A. E. Herr, *Nat Protoc*, 2016, **11**, 1508–1530.

27   G. Dormán, H. Nakamura, A. Pulsipher and G. D. Prestwich, *Chem. Rev.*, 2016, **116**, 15284–15398.

28   A. W. P. Vermeer and W. Norde, *Biophys. J.*, 2000, **78**, 394–404.

29   S. M. Grist, A. P. Mourdoukoutas and A. E. Herr, *bioRxiv*, 2019, doi: https://doi.org/10.1101/805770.

30   J. Siepmann and N. A. Peppas, *Adv. Drug Deliv. Rev.*, 2001, **48**, 139–157.

31   C. C. Lin and A. T. Metters, *Adv. Drug Deliv. Rev.*, 2006, **58**, 1379–1408.

32   A. L. Shapiro, E. Viñuela and J. V. Maizel Jr., *Biochem. Biophys. Res. Commun.*, 1967, **28**, 815–820.

33   H. P. Erickson, *Biol. Proced. Online*, 2009, **11**, 32–51.

34   H. Park, C. S. Johnson and D. A. Gabriel ', *Macromolecules*, 1990, **23**, 1548–1553.

35   K. A. Yamauchi and A. E. Herr, *Microsystems Nanoeng.*, 2017, **3**, 16079.

36   S. J. Shapiro, D. Dendukuri and P. S. Doyle, *Anal. Chem.*, 2018, **90**, 13572–13579.

37   H. Berg, *Random walks in biology*, 1993.

38   K. Ferguson, *Metab., Clin. Exp*, 1964, **13**, 985–1002.

39   T. M. Squires, R. J. Messinger and S. R. Manalis, *Nat. Biotechnol.*, 2008, **26**, 417–426.

40   D. L. Holmes and N. C. Stellwagen, *Electrophoresis*, 1991, **12**, 612–619.

41   J. Narayanan, J.-Y. Xiong and X.-Y. Liu, *J. Phys. Conf. Ser.*, 2006, **28**, 83–86.

42   H. Corstjens, H. A. H. Billiet, J. Frank and K. C. A. M. Luyben, *Electrophoresis*, 1996, **17**, 137–143.

43   C. W. M. P. Sillen, E. Barendrecht, L. J. J. Janssen and S. J. D. van Stralen, *Int. J. Hydrogen Energy*, 1982, **7**, 577–587.

44   K. Macounová, C. R. Cabrera, M. R. Holl and P. Yager, *Anal Chem*, 2000, **72**, 3745–3751.

45   B. Bjellqvist, K. Ek, P. Giorgio Righetti, E. Gianazza, A. Görg, R. Westermeier and W. Postel, *J. Biochem. Biophys. Methods*, 1982, **6**, 317–339.

46   A. M. Tentori, K. A. Yamauchi and A. E. Herr, *Angew Chem Int Ed Engl*, 2016, **55**, 12431–12435.

47   Tris-Glycine Buffer (TG Buffer), pH 8.3±0.2, 10X Concentrate, https://www.polysciences.com/default/catalog-products/life-sciences/buffers/tris-glycine-buffer-tg-buffer-ph-8-3-0-2-10x-concentrate/, (accessed 26 January 2020).

48   N. C. Stellwagen, *Electrophoresis*, 2009, **30(Supp1)**, S188-95.

49   J. M. Brewer, *Science (80-.).*, 1967, **156**, 256–257.

50   C. C. Lin and A. T. Metters, *Pharm. Res.*, 2006, **23**, 614–622.

51   S. Magdelin, *Gel Electrophoresis - Principles and Basics*, Rijeka, Croatia, 2012.

52   J. M. Walker, in *Basic Protein and Peptide Protocols*, Humana Press, 2003, pp. 17–22.

2.6 Supplemental Information

Table S1: Fabrication conditions for polyacrylamide gels.

Reagent	Sizing Gel	20%T PA gel	4%T PA loading gel
30%T, 29:1C stock acrylamide/bis-acrylamide; No. A3574, Sigma-Aldrich	7% w/v final acrylamide concentration	20% w/v final acrylamide concentration	4% w/v final acrylamide concentration
10X Tris-glycine; No. 1610734, Bio-Rad	10% v/v	10% v/v	10% v/v
Rhinohide™; No. R33400, Invitrogen	4.66% v/v	4.66% v/v	4.66% v/v
100mM N-[3-[(3-Benzoylphenyl)-formamido]propyl] methacrylamide in DMSO; No. PAL0603, PharmAgra Labs	3% v/v (3mM)	--	--
Donkey anti-Rabbit IgG AlexaFluor® 647; No. A31573, Invitrogen	--	--	0.2 mg/mL
Degas and Sonication Time	5 min	5 min	5 min
Initiators	--	--	--
APS; No. A36778, Sigma-Aldrich	0.08% w/v	0.08% w/v	0.08% w/v
TEMED; No. T9281, Sigma-Aldrich	0.08% v/v	0.08% v/v	0.08% v/v
Polymerization Time	60 min	60 min	60 min
Gel Dimensions (x-y-z)	10mm-10mm-1mm	10mm-10mm-1mm	14mm-14mm-1mm
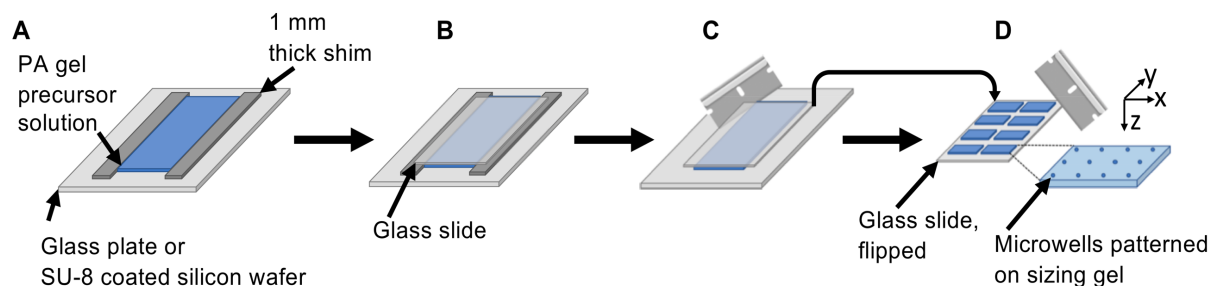
Figure S1: PA gel fabrication assembly. (**A**) To assemble the fabrication mold for PA gels, two 1 mm thick shims were affixed with adhesive onto either an SU-8 coated silicon wafer (for sizing gel fabrication) or a glass plate (for 20%T PA gel fabrication). PA gel precursor solution was cast to the fabrication mold by pipetting the solution between the shims. (**B**) A glass slide was placed on top of the shims without trapping air bubbles in the precursor solution. (**C**) After the gel polymerized (60 min), the gel was released from the fabrication mold by first removing the shims by hand, then sliding a razor between the glass slide and the bottom mold surface (silicon wafer or glass plate), and finally using the razor to gently pry the glass slide away from the silicon wafer or glass plate. To prevent gel surface adhesion, the glass surfaces were treated with Gel Slick® and the SU-8 features were coated with dichlorodimethylsilane. (**D**) The glass slide and gel were removed from the fabrication mold and flipped (glass slide on a flat surface, gels on top of glass slide). The glass slide was used as a support to trim the gels (x-y-z dimensions: 10-10-1 mm). Microwells were patterned on a x-y face of the sizing gel from the SU-8 micropost features (Microwell diameter: 32 µm. Microwell depth: 40 µm. Microwell center-center spacing: 100 µm.). The 20%T gel was not patterned with any features, as the glass plate was featureless.

Table S2: Buffer compositions.

Electrotransfer Buffer	1X RIPA Buffer
10% v/v 10X Tris-glycine; No. 1610734, Bio-Rad	10% v/v 10X Tris-glycine; No. 1610734, Bio-Rad
0.5% v/v Triton X-100; No. X100, Sigma-Aldrich	0.5% w/v Sodium Dodecyl Sulfate; No. L3771, Sigma-Aldrich
89.5% v/v MilliQ Water	0.25% w/v Sodium Deoxycholate; No. D6750, Sigma-Aldrich
--	MilliQ Water: 79.8% v/v

Table S3: Fabrication conditions for probe loading gels

Reagent	Probe Loading Characterization Gel	OVA Immunoprobing: Primary Probe Loading Gel	OVA Immunoprobing: Secondary Probe Loading Gel
Ultrapure Low Melting Point Agarose; No. 16520050, Invitrogen	1.5% g/mL (dissolved in 1X Tris-glycine)	1.5% g/mL (dissolved in 1X Tris-glycine)	1.5% g/mL (dissolved in 1X Tris-glycine)
Antibody Probes	0.2 mg/mL Donkey anti-Rabbit IgG AlexaFluor® 647; No. A31573, Invitrogen	<u>Diffusive probing:</u> 0.1 mg/mL Rabbit anti-OVA IgG; No. Ab181688, Abcam <u>Electrotransfer probing:</u> 0.0075 - 0.1 mg/mL Rabbit anti-OVA IgG; No. Ab181688, Abcam	<u>Diffusive probing:</u> 0.2 mg/mL Donkey anti-Rabbit IgG AlexaFluor® 555; No. A31572, Invitrogen <u>Electrotransfer probing:</u> 0.015 - 0.2 mg/mL Donkey anti-Rabbit IgG AlexaFluor® 555; No. A31572, Invitrogen
Gelation Time	5 min on ice pack	5 min on ice pack	5 min on ice pack
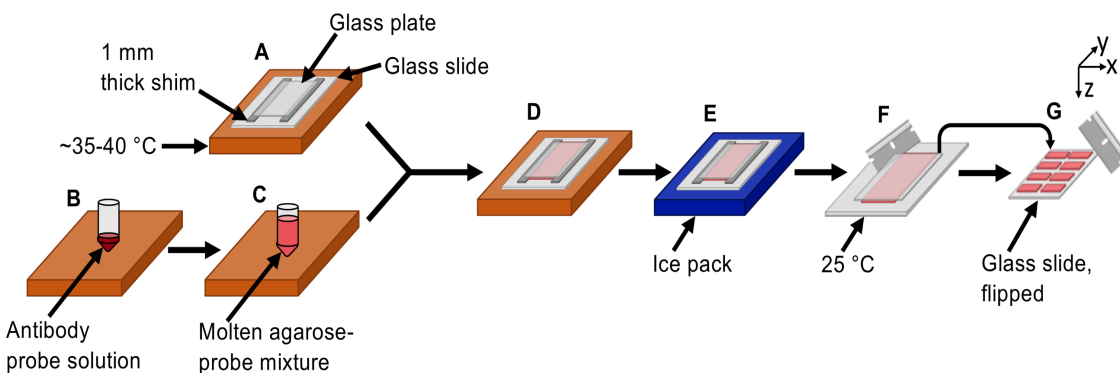
Figure S2: Agarose probe loading gel fabrication assembly. (**A**) To assemble the fabrication mold for the loading gel, first, two 1 mm thick shims were affixed with adhesive onto a glass plate. Then, a glass slide was affixed with adhesive onto the two shims. The fabrication mold was then placed on a hot plate and warmed to ~35-40 °C. (**B**) An Eppendorf tube was warmed on a hotplate and brought to ~35-40 °C. Antibody probe solution was added to the heated Eppendorf tube. (**C**) Molten agarose was added to the antibody probe solution, and mixed by pipetting. (**D**) To cast the loading gel to the fabrication mold, the molten agarose gel-probe mixture was pipette between the glass slide and glass plate. Enough molten agarose-probe mixture was pipetted to fill the volume encased by the glass slide, glass plate, and shims, without introducing air bubbles. (**E**) To gelate the loading gel, the fabrication mold was transferred to an ice pack for the molten agarose-probe mixture to cool for 5 min. (**F**) After gelation, the fabrication mold was removed from the ice pack, and placed on a 25 °C surface. The gel was released from the fabrication mold by first removing the shims by hand, then sliding a razor between the glass slide and glass plate, and finally using the razor to gently pry the glass slide away from the glass plate. (**G**) The glass slide and loading gel were removed from the fabrication mold and flipped (glass slide on a flat surface, loading gel on top of glass slide). The glass slide was used as a support to trim the loading gels (x-y-z dimensions: 14-14-1 mm).
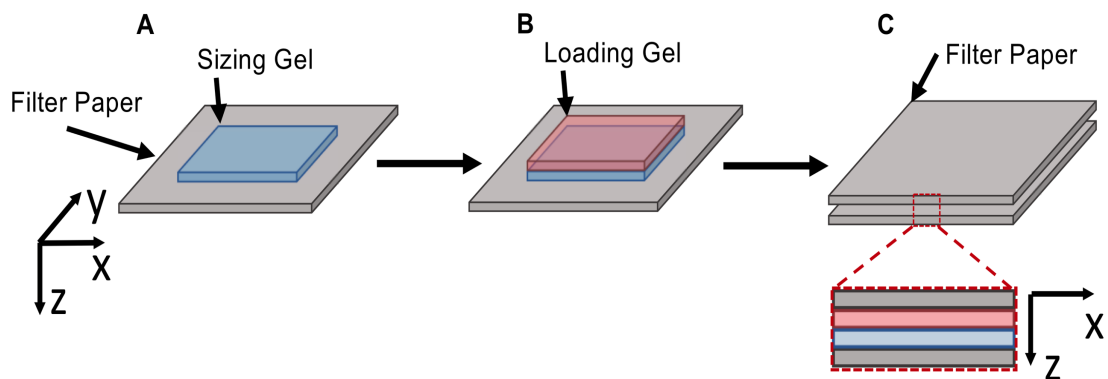
Figure S3: Filter paper – gels – filter paper sandwich assembly for electrotransfer probe loading. (**A**) A sizing gel was placed on a western blot filter paper piece. (**B**) A loading gel was placed on the sizing gel without trapping air bubbles between the two gels. The loading gel was aligned in the x-y plane to entirely overlap the sizing gel. (**C**) A second western blot filter paper piece was placed on top of the loading gel without perturbing the alignment of the loading and sizing gels.
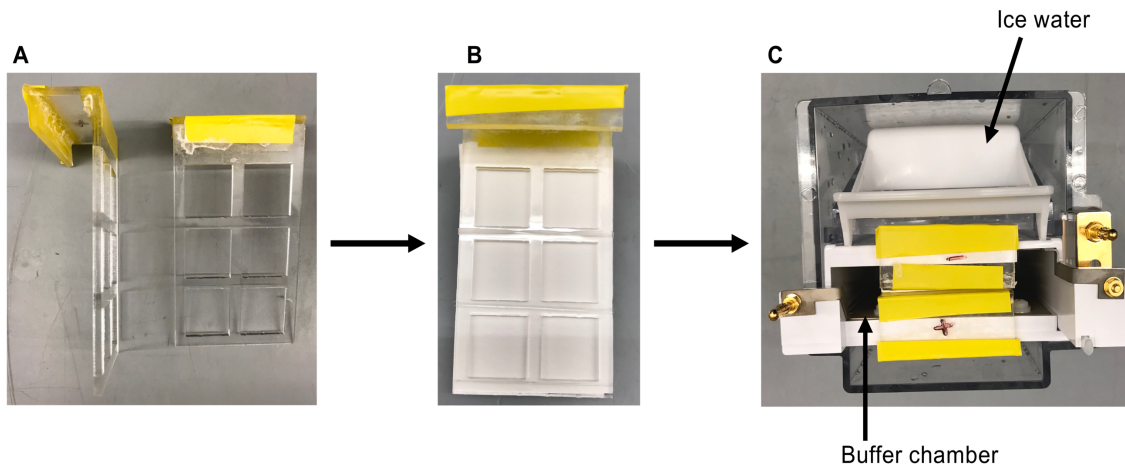
Figure S4: Acrylic clamp assembly. (**A**) The trace for the acrylic clamp face in contact with the filter paper have the following dimensions: 55 mm width x 85 mm height. Window cut outs have the following dimensions: 20 mm squares, 3 x 2 array, 5 mm edge-to-edge spacing between square windows. The windowed component of the clamp was super glued to an acrylic rectangle (55mm wide x 30 mm long) so that the assembled gel holder could rest on the brim of the electrotransfer system buffer chamber. (**B**) The clamp was designed with capacity for up to 6 gel sandwiches to be housed simultaneously. The clamp is compressed by using plastic elastomers along the frame of the windows. (**C**) The acrylic clamp rests on the brim of the electrotransfer buffer chamber, and the gels sandwiches are submerged in buffer volume.

Table S4: Electrotransfer conditions in probe loading and unloading

Electrotransfer Probing Process	Electric Field Strength	Electrotransfer Time
Probe Loading	8 V/cm	11.5 min
Probe	12 V/cm	15 min
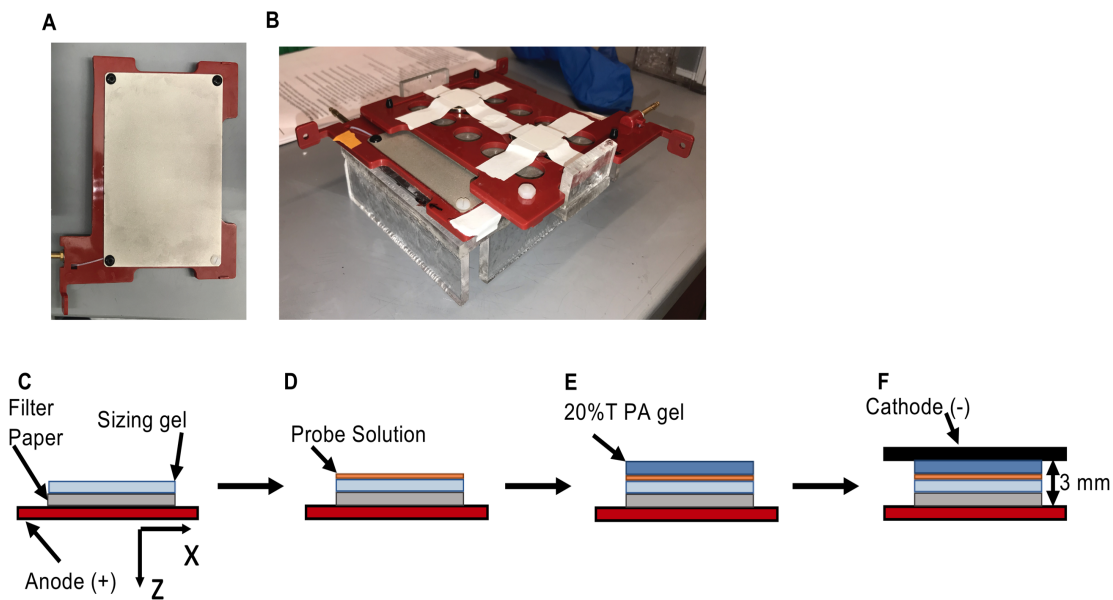
Figure S5: The semi-dry electrotransfer system was used to electrophoretically inject antibody probe from free-solution into a sizing gel for probe electromigration characterization. (**A**) The system is composed of two electrode plates surrounded by plastic alignment casings. (**B**) The system was assembled by aligning the two electrode plates and magnetically bringing the plates into contact. To prepare the sample between the electrode plates (**C**) first, a piece of filter paper was placed on the anode (filter paper x-y-z dimensions: 10-10-1 mm; filter paper x-y face placed in contact with anode; filter paper equilibrated in Electrotransfer Buffer for 5 min). (**D**) Then, a sizing gel was placed on the filter paper. The mircowell patterned face of the sizing gel was faced upwards and was gently blotted dry with a Kimwipe. Next, 5 μL of 5 μM Donkey anti-Rabbit IgG AlexaFluor® 647 solution (in 1X Tris-glycine) was pipette on the microwell patterned face of the sizing gel. The microwells acted as a reservoir for probe solution to facilitate electrophoretic injection. (**E**) After pipetting the Ab probe solution, a 20%T PA gel was blotted dry (gel fabrication described in Table S1) and placed on the sizing gel. (**F**) Two, 3 mm shims were placed around the filter paper – gel assembly, and the cathode was placed on top. The electrode plates were magnetically compressed.

Table S5: Diffusive transfer times in probe loading and unloading

Diffusive Transfer Probing Process	OVA Immunoprobing: Primary & Secondary Probe	Loading and Unloading Characterization
Probe	15 h	28 h
Probe	45 h	45 h
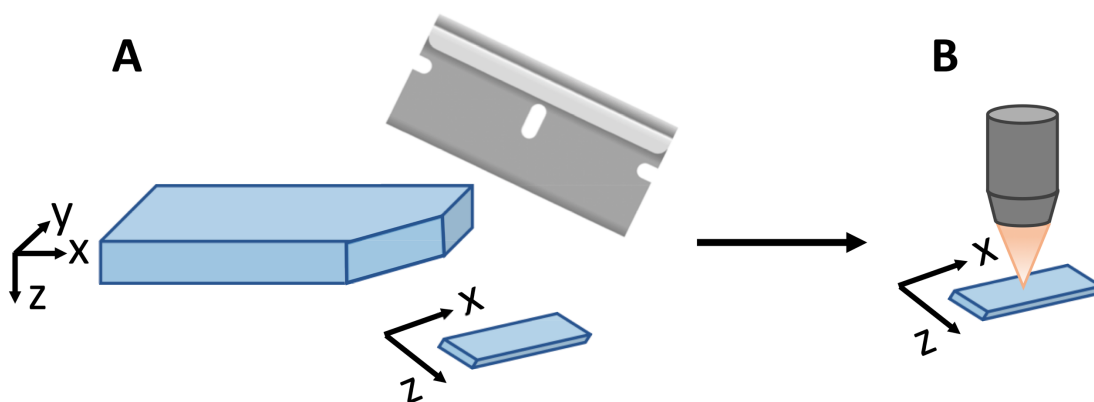
Figure S6: Workflow for imaging gel-sliver. (**A**) A sizing gel was cut using a razor to produce a gel-sliver (dimensions of gel sliver: 10mm x ~0.5mm x 1mm in x-y-z). (**B**) The gel sliver was imaged such that the gel x-z face was parallel with the microscope plane-of-focus.

Note S1: Design considerations for diffusive probing system

In designing the diffusive probing control, we considered systems for (i) uniform probe delivery to the sizing gel and (ii) consumption of the antibody probe mass as equivalent to that consumed in the electrotransfer probing system. To satisfy this latter criterion when diffusive probing is accomplished by submerging a sizing gel in a probe solution, requires prohibitively large consumption of antibody probe material. For example, sufficient probe-solution volume to submerge a sizing gel requires an antibody probe concentration that is low compared to the probe concentration maintained in the loading gel (using single well of 12 well plate). The in-gel probe concentration at equilibrium is further reduced compared to the in-solution probe concentration, as size exclusion partitioning strongly impedes diffusive probe entry into the sizing gel. Thus, to satisfy the latter criterion, an alternative method for interfacing probe solution to the sizing gel without reducing the in-solution probe concentration was devised by pipetting a smaller volume of probe solution directly onto the sizing gel (the reduced solution volume preserves in-solution antibody probe concentration). The primary challenge in this system design is that fluid tends to pool around gel edges, resulting in non-uniform probe delivery to the sizing gel surface that is in contact with the probe solution, as we have previously demonstrated.[1] Consequently, the loading gel – sizing gel – loading gel diffusive probing system was ultimately chosen as it meets the needs of our diffusive probing control system by (i) preventing probe solution from pooling to gel edges and (ii) not diluting probe in large solution volumes.

1   A. Geldert, H. Huang and A. E. Herr, *Sci. Rep.*, 2020, **10**, 1–12.

3 3D Projection Electrophoresis for Single-Cell Immunoblotting

3.1 Introduction

Proteins are biomolecules that play a direct role in nearly all cellular processes[1]. As such, protein expression is a primary metric for quantifying cell state[2]. Although genomics and transcriptomics analysis of gene and RNA expression are powerful and complementary measurement techniques, they often do not predict protein expression at the single-cell level[3–5]. Proteoforms, or different forms of proteins arising from the same gene[6], are also critical to understanding cell state: cellular heterogeneity at the proteoform level plays critical roles in cellular processes including regulating tumor growth[7] and resistance to treatment in cancer[8]. Many single-cell proteomic technologies are limited to protein detection by antibodies with limited protein specificity, which may not be proteoform-specific[9] and thus cannot distinguish proteoform-level heterogeneity. Protein separations based on electrophoresis can overcome these antibody specificity limitations through dual measurements of the physicochemical properties of protein targets (i.e., molecular mass, isoelectric point) and primary antibody reactivity for protein detection.

To offer a comprehensive understanding of complex cellular systems, selective detection of protein targets in individual cells is required; yet, key single-cell analysis challenges persist in throughput, sample preparation, and interfacing[10]. Measurement throughput is crucial to detect rare but important subpopulations of cells (e.g., metastasis, resistance to treatment), but – to attain suitable statistical power – the minimum sample size increases as subpopulation prevalence decreases[11]. Thus, the ability to assay hundreds or even thousands of cells is valuable. Further compounding the challenge of measuring a large cell population with single-cell resolution is synchronously assaying all of the single cells. Proteomic cell state is dynamic[12] so differences in analysis time across cells can add artefactual heterogeneity – particularly when assessing cell response to drugs or environmental stimuli. Furthermore, single-cell lysate preparation and interfacing for interrogation must also preserve detectable protein concentrations from low single-cell copy numbers. Dilution into larger-than-a-cell volumes, sample losses, and lysate changes during transfer to an analysis platform can further challenge single-cell proteoform measurement[10].

Since the early 1990's, capillary electrophoresis (CE) has been applied to surmount challenges in analysis of lysate from individual cells[13]. To maintain protein target concentrations during analysis, CE uses fused silica capillaries with micron-scale diameters, facilitating efficient dissipation of Joule heating and ultra-rapid electrophoresis. For lysate transfer, the CE systems use physical alignment of the capillary to reagent baths or isolated single cells. Early single-cell CE

technologies were capable of assaying 10's of cells per day, making measurement of single-cell heterogeneity among large cell populations out of reach[14,10]. CE Improvements use capillary arrays for simultaneous analyses of samples[15] and bundled 168-plex microstructured silica fibers (demonstrated to improve heat transfer rather than throughput)[16]. Analyte loss via adsorption to the capillary surface (due to large surface-area-to-volume ratios) challenges single-cell CE measurements[10].

To advance single-cell resolution analyses, researchers brought both automation and microfluidic design to bear to efficiently integrate disparate sample preparation and electrophoretic analysis. In an excellent example, the Allbritton group introduced an automated, serial single-cell electrophoresis system by integrating a single glass capillary with a microwell array for cell isolation, using a motorized stage for microwell alignment to the capillary for serial sampling and analysis[17]. For analysis of a population of 219 mammalian cells, throughput was clocked at 2.1 cells/min (cell lysis, electrophoresis, and real-time fluorescence detection of sphingosine fluorescein and sphingosine-1-phosphate fluorescein). Also exemplar of integrated approaches, planar microfluidic devices support analysis of up to 12 cells/min[18,19]. While useful, serial analysis of large cell populations is inherently asynchronous and, as mentioned, can introduce artefactual cell-to-cell heterogeneity, particularly critical to assessing response to stimuli.

Mass spectrometry is a powerful, complementary separations technology that is promising for single-cell protein detection. Aside from mass cytometry[20], other forms of mass spectrometry do not rely on antibody specificity for selective protein detection. Highly multiplexed protein detection from single cells (1000's of targets per cell) is possible with bottom-up mass spectrometry, although throughput has not yet exceeded 100 individual cells[21,22]. Mass spectrometry is limited to highly abundant proteins ($>10^4$ copies per cell)[21,22] and small-to-intermediate molecular masses for top-down proteomics (e.g. typically 25 kDa for MALDI-TOF, although specialized detectors facilitate detection of proteins up to 110 kDa[23,24]). Furthermore, the vast majority of single-cell mass spectrometry approaches are bottom-up, wherein the requirement for protein digestion to peptides confounds proteoform stoichiometry. While top-down mass spectrometry does measure intact proteins – making the approaches relevant to proteoforms – and imaging mass spectrometry can assay larger numbers of cells (e.g. >1000 dorsal root ganglia)[25], larger proteins present a measurement challenge even with optimization for wider-range mass measurement (m/z 400 to 20 000)[25].

Immunoblotting is a class of separations with a powerful capacity for targeted proteomics. To detect protein targets *a priori* identified through hypotheses or discovery tools, this suite of separations approaches integrate two analytical modalities to yield enhanced target specificity over either alone: separation of proteins by electrophoresis and probing of specific targets by immunoreagents. While only recently developed for single-cell and sub-cellular resolution by our group, immunoblotting (and its most popular form, western blotting[26,27]) have been a workhorse in biological and clinical laboratories for decades. Using automation in a different way to advance towards both single-cell resolution and multiplexed detection, the Kennedy group designed an automated system that integrates microchip electrophoresis with immunoprobing on an off-chip PVDF membrane[28]. Integration between the microchip and membrane uses a mobile membrane,

with the separations effluent deposited (blotted) onto that moving membrane. While not demonstrated for single-cell analysis, multiplexing was boosted to 11 separated protein targets from 9 serial separations in 8 min, with each separation from the same aliquot of bulk cell lysate with a total protein content similar to that of a single cell (400 ng total protein). Taking a different approach inspired by single-cell DNA electrophoresis (COMET assays)[29], we introduced single-cell western blotting with a throughput of ~200 cells/min[30]. The planar 2D device uses a thin layer of polyacrylamide gel stippled with microwells for parallel cell isolation and lysis. Protein lysate is subjected to immunoblotting in the photoactive polyacrylamide gel abutting each microwell. We have applied the single-cell western blotting technology to studying heterogeneity of circulating tumour cells[31], smooth muscle cells[32], and HER2 isoform expression in clinical specimens[33]. Furthermore, using similar design principles we have introduced single-cell immunoblotting tools based upon other physicochemical protein properties (e.g. subcellular localization[34] and isoelectric point[35,36]) and adapted the single-cell western blot to assess adherent cells (without detachment)[37] and study invasive motility[38]. These tools have emerged as powerful technologies for single-cell analysis; however, their throughput and sample consumption remain limited by the large spacing between microwells required for the protein separation[37].

Here, we introduce a high-density parallelized single-cell immunoblotting device that uses the third dimension (z-axis), to enhance the microwell array density and, hence, throughput and sample consumption. In projection electrophoresis, we sought to leverage the full gel volume to map protein size and originating cell position from the 3D location of separated protein bands. The 3D design is inspired by multifunctional 3D hydrogel materials like Expansion Microscopy[39] and CLARITY[40], as well as the efficient electrotransfer of protein from gel to PVDF membrane in conventional western blotting[27,41] and bulk separations in 3D and layered systems[42–44]. Using a 3D volume improves microwell array density to 25 microwells/mm^2 from 2 microwells/mm^2 in 2D (planar) devices. Owing to this density improvement, the assay consumes an order of magnitude less volume of a cell suspension (25 μL vs. 300 μL) to assay ~300 cells (similar to planar systems), resulting in a 10-fold improvement in sample consumption. In this work, we describe the separation performance and use the physics of 3D diffusion to design the projection electrophoresis system, and perform near-simultaneous immunoblotting of both cytoplasmic (GAPDH, actinin, beta tubulin) and nuclear (PTBP1) protein targets from hundreds of single mammalian breast and brain tumour cells.

3.2 Methods and Materials

Wafer microfabrication and silanization. Wafers with 40 μm high features (32 μm diameter microwells for purified protein experiments and lysis monitoring, or 25 μm diameter microwells for BT474 and U251 single-cell separations) fabricated using SU-8 3050 (Microchem, now Kayaku Advanced Materials, Inc.) were fabricated according to the manufacturer's instructions and then silane-treated[62]. Silicon wafers (WaferPro C04009) were cleaned by 5-minute agitated immersion in acetone followed by rinsing in acetone, isopropanol, and deionized water. Wafers were then dried under a nitrogen stream and dehydrated by a 10-minute bake on a hotplate set to 200 °C. Immediately after cooling, SU-8 3050 was spin-coated onto the wafers using a spin program consisting of 10 seconds at 500 RPM with an acceleration of 100 RPM/s followed by 30s at 4000 RPM with an acceleration of 500 RPM/s. The resist was soft baked for 2 minutes on a 65 °C hotplate followed by 15 minutes on a 95 °C hotplate and finally 3 minutes on a 65 °C hotplate. The resist was exposed to ultraviolet light within a mask aligner for 10.8s at an optical power of 29.26 mW/cm^2 (for an exposure dose of 316 mJ/cm^2), through a transparency mask (CAD/Art Services, Inc.) and a longpass optical filter (Omega PL-360LP) (both of which attenuate the dose applied to the wafer below the 316 mJ/cm^2 stated above). After exposure, each wafer was post-exposure baked for 1 minute at 65 °C, 5 minutes at 95 °C , and 1 minute at 65 °C and cooled slowly by convection. Once cooled to room temperature, the features were developed in SU-8 developer (Microchem, now Kayaku Advanced Materials, Inc.) for 2.5-3 minutes on a shaker followed by 30-60s spraying with fresh developer. The wafer was then rinsed by spraying with isopropanol to pool and cover both sides of the wafer 5 times, and then dried under a nitrogen stream. Finally, the resist was hard baked for 30 minutes at 200 °C and then slowly ramped down to room temperature in 40 °C increments every 20 minutes. The patterned wafer was treated to facilitate gel release using vapour deposition of dichlorodimethylsilane (Sigma-Aldrich 440272-100ML) in a desiccator[78]. Within a chemical fume hood, wafers were placed face-up in a desiccator and ~50-100 μL of liquid dichlorodimethylsilane was deposited into a 35 mm petri dish inside the desiccator. The desiccator was then immediately closed and connected to vacuum after a 1-minute waiting period. The desiccator was evacuated for 5 minutes; the vacuum was then switched off, desiccator valve closed, and silane left to settle under vacuum for 30 minutes. The desiccator valve was then slowly opened and wafers rinsed with deionized water and dried under a nitrogen stream.

Polyacrylamide gel fabrication. Substrate-free and featureless polyacrylamide gels (used for lysis and enclosing purified protein microwells) were fabricated between a glass plate (McMaster-Carr) and 25x75 mm or 50x75 mm glass slide (VWR), both treated with Gel Slick® glass plate coating according to the manufacturer's instructions and rinsed briefly in deionized water prior to gel fabrication. For purified protein experiments and cell seeding gels, microwell-stippled gels were cast between a methacrylate-functionalized glass slide and a dichlorodimethylsilane (Sigma Aldrich 440272)-treated silicon wafer (WaferPro). The methacrylate-functionalized slide was treated to promote gel adhesion with a 30-minute exposure to a degassed aqueous solution of 20% 3-(Trimethoxysilyl)propyl methacrylate (Sigma-Aldrich 440159-100ML) and 30% acetic acid (Fisher A38212) in deionized water, and subsequently rinsed in pure methanol and deionized water and then dried under a nitrogen stream[62].

Our approach for substrate-free micropatterned gel fabrication was inspired by that recently developed by our group to fabricate releasable gel microparticles[78]. In all cases, 1 mm or 500 μm

thick gels were fabricated using spacers of the appropriate thickness (C.B.S Scientific Gel Wrap) between the two glass pieces or between the wafer and glass slide. Acrylamide precursor solutions for the various gels were prepared by diluting 30% stock acrylamide/bis-acrylamide precursor (Sigma-Aldrich A3699) and Rhinohide® (ThermoFisher R33400) solution (to increase mechanical robustness of substrate-free gels) in ultrapure water (Millipore®) and 10X tris-glycine (Bio-Rad 1610734) where appropriate. Separation gels contained 3 mM final concentration BPMA: N-(3-((3-benzoylphenyl)formamido)propyl) methacrylamide, which was custom-synthesized by PharmAgra Labs (cat. no. PAL0603)[62]. BPMA is co-polymerized into the gel matrix and permits photo-immobilization of proteins. Gels were chemically polymerized for 60 minutes with 0.08% (w/v) ammonium persulfate (APS, Sigma-Aldrich A3678) and 0.08% (v/v) TEMED (Sigma-Aldrich T9281), from freshly-prepared 10% stock solutions in ultrapure water. The constituents of the various gel types used in this work are presented in Supplementary Table 1, and a schematic showing the released gel fabrication and molding process is depicted in Supplementary Figure 7.

After polymerization, gels were trimmed to size using a razor blade and released from the glass substrate by carefully sliding the razor blade under the gel, applying firm pressure with the blade onto the glass and gently adding water between the razor blade and gel to lubricate and prevent tearing. Separation and shield/lysis gels were stored in the appropriate buffer solution for a minimum of 12 hours and up to 4 days prior to running separations. Buffer storage conditions are presented in Supplementary Table 1 and were either (1) dual function lysis-electrophoresis modified RIPA buffer (1X or 2X RIPA as described in Supplementary Table 2), (2) run buffer (1X tris-glycine with 0.5% Triton X-100), or (3) 1X tris-glycine for gels to be used for cell settling. Buffers used in this work are described in Supplementary Table 2.

Z-directional electrode system. The Z-directional electrode separation system consists of planar electrodes integrated into a custom laser-fabricated acrylic alignment setup and brought into contact with two 32 mm diameter, 3 mm thick neodymium rare-earth magnets on the back side of each electrode (each magnet specified to provide 19 lbs of pull force). Uniform spacing between the electrodes is facilitated by 2.5 mm (purified protein experiments) or 3 mm (cell experiments) removable polymer spacers (C.B.S Scientific Gel Wrap) at the top and bottom of the electrodes. The planar electrodes were commercial platinum-coated electrotransfer anodes (Bio-Rad Criterion anode plates) with plastic housings modified to permit close proximity of the electrode surfaces. Electric fields were provided by a power supply (Bio-Rad PowerPac® Basic) connected to the electrodes with standard banana plug interfacing. Cold packs on the back side of each electrode maintained gel temperature at ~4°C to help to mitigate deleterious effects of Joule heating during purified protein separations. To aid in lysis and protein solubilization[63], the cold packs were heated in a 55ºC water bath for single-cell separations, yielding electrode temperatures of ~37ºC. Hot packs were heated for >10 minutes to equilibrate to temperature, and exchanged every ~15 minutes between separations.

Purified protein separation experiments. Mixed molecular weight purified protein solutions were prepared by diluting stock solutions of Alexa Fluor®555-labelled bovine serum albumin (BSA; Thermo Fisher Scientific A34786; 5 mg/mL stock), Alexa Fluor®488-labelled ovalbumin (OVA; Thermo Fisher Scientific O34781; 2 mg/mL stock), and Alexa Fluor®647-labelled donkey anti-mouse secondary antibody (IgG; Thermo Fisher Scientific A31571 lot 1900251; 2 mg/mL

stock) in a run buffer (Supplementary Table 2) consisting of 1X tris-glycine (prepared by ultrapure water dilution of 10X stock, Bio-Rad 1610734) containing 0.5% v/v Triton X-100 (Sigma). High molecular weight purified protein solutions were prepared by diluting stock solutions of Alexa Fluor®488-labelled lectin (Thermo Fisher Scientific L11270; 2 mg/mL stock), and Alexa Fluor®647-labelled transferrin (Thermo Fisher Scientific T23366; 5 mg/mL stock) in the same run buffer. All proteins were diluted to a final concentration of 5 μM.

Western blotting filter paper of 1 mm thickness (Thermo Fisher Scientific 84783) was cut into 12x12 mm squares and allowed to equilibrate in dual-function lysis-electrophoresis modified RIPA buffer for >10 minutes prior to starting separations. Microwell-patterned separation gels of 1 mm thickness and shield gels of 500 μm thickness were prepared as described in Supplementary Table 1, cut into squares of 9x9 mm (separation gel) or ~12x12 mm (shield gel), and equilibrated in the appropriate buffer for >12h.

We first assessed the appropriate constant current conditions to yield the target electric field. We set up a dummy separation stack consisting of the anode (bottom), the buffer-equilibrated filter paper, a separation gel, a shield gel (with bottom surface dried by placing on a clean, dry Kimwipe), and the cathode (top). We supplied a constant voltage of 13 V (the necessary voltage for an electric field of 52 V/cm) and noted the initial current through the dummy stack (typically ~33 mA). This constant current was chosen for each following separation run on a given day, and the initial and final voltages were noted during each trial to quantify the electric field and resistance changes during the separation.

To run the separations, we again stacked the anode, buffer-soaked filter paper, and separation gel, but this time dried the top (microwell-studded) surface of the separation gel gently bringing it into contact with a folded Kimwipe prior to stacking on top of the filter paper. Drying the top surface of the separation gel and bottom surface of the shield gel reduces dilution of the purified protein solution prior to separation. We pipetted 3 μL of the mixed purified protein solution (either the mixed molecular weight standard or the high molecular weight standard) on top of the separation gel and spread the resulting droplet to cover the surface of the gel using the side of a p20 pipette tip, taking care not to puncture the gel surface. We then dried the bottom side of a shield gel by placing it on a folded Kimwipe, brought it into contact with the separation gel by carefully lowering it from one corner to reduce bubble entrapment, and assembled the cathode on top. We supplied constant current between the anode and cathode for varying electrophoresis times, running duplicate gels for each electrophoresis time in each experiment.

Immediately after electrophoresis was complete, the power was shut off and the system disassembled to permit optical access for a UV source (Hamamatsu Lightningcure LC5). The liquid light guide-coupled UV source was used to photocapture the separated protein bands using a 45s UV exposure, holding the tip of the liquid light guide ~4 cm from the separation gel. We have photocaptured with both the top (microwell) and bottom (flat) side of the separation gel facing the light guide. The total time between beginning electrophoresis and initiating UV exposure was recorded for each test as an estimate of the in-gel diffusion time t_{diff}.

After photocapture, each gel was rinsed briefly in deionized water and then stored for >12 hours in 1X tris-buffered saline solution with Tween® (TBST, prepared from Cell Signaling Technology

9997S 10X stock and MilliQ ultrapure water) in a polystyrene 12-well plate prior to imaging to permit release of any non-photocaptured protein. Gels were imaged through a #1 coverslip using a Zeiss LSM 880 laser-scanning confocal microscope fitted with a 20X water dipping objective (NA=1.0, Zeiss W Plan APO 20x/1 DICIII). A confocal Z-slice spacing of 5 μm was chosen, and volumes extending ~100 μm past visible fluorophore bands were imaged. As we were not quantifying or comparing protein abundance, excitation laser powers were adjusted to permit fluorescence visibility depending on the sample brightness. Fluorescence intensities were not compared between purified protein samples. Similarly, images were brightness and contrast-adjusted in Fiji[79] (based on ImageJ[80], National Institutes of Health) to ensure visibility of protein bands. Maximum intensity projection 3D renderings were prepared in Zeiss Zen Blue software.

Purified protein confocal datasets were analyzed using custom analysis scripts in MATLAB®. The scripts were designed to (1) find and track regions of interest (ROIs) corresponding to protein originating from each of the microwells through the depth of each confocal stack, (2) create 1D intensity plots of summed fluorescence intensity vs. Z depth for each ROI by summing the fluorescence intensity for the ROI at each Z-plane, (3) assess the Z migration distance and peak width for each protein by Gaussian fitting each intensity profile peak, allowing the user to set bounds for fitting peaks corresponding to each purified protein, (4) measure the diffusional spreading of protein from each microwell by Gaussian fitting the summed 1D X- and Y-intensity profiles for each protein at its Z migration peak location for each protein, (5) plot migration distance, Z-direction peak width, and X-Y peak width vs. electrophoresis time or diffusion time, comparing across multiple gels.

Zeiss CZI confocal Z-stacks and associated metadata were imported into MATLAB® (MathWorks®) using the MATLAB® Bio-Formats libraries provided by the Open Microscopy Environment[81]. ROIs were segmented in each Z-slice image (summing the intensities of all colour channels into one image for the purposes of segmentation) using intensity thresholding followed by morphologic open and close operations to remove erroneously-segmented small features and close incomplete contours. A fill operation was then used to close all holes in the segmented spots of protein, and all segmented objects touching the border of the image were removed. The centroids of the segmented spots of protein at each Z location were stored, and a MATLAB® particle tracking library (based on a previous IDL implementation[82]) made publicly accessible by Prof. Daniel Blair and Prof. Eric Defresne[83] was used to track the positions of protein originating from each microwell through the Z depth of the image. The tracked centroids were then subject to a quality control step to remove protein spots that were only found in small portions of the full Z volume. After this was complete, the tracking code output a set of tracked 'particles' (protein spots originating from a given microwell), each with a list containing the x-y location of the centroid of each protein spot for every Z location in the image. To create the intensity profiles, the intensities in a 300 pixel (102 μm) square ROI were analyzed surrounding each centroid at each Z location. The data were background-subtracted by subtracting from each pixel the average measured intensity 15 μm below the bottom of the microwells, in regions at least 100 pixels (34 μm) from any segmented protein spots. After Gaussian fits to find the migration distance, z-direction peak width, and x-y peak width for each protein peak, the data from all of the ROIs from multiple gels (multiple electrophoresis times in duplicate) were plotted and fit to the expected linear physical relationship (migration distance vs. electrophoresis time, squared peak width and squared x-y peak width vs. total in-gel time).

Cell culture. U251 human glioblastoma cells stably transduced with turboGFP by lentiviral infection were kindly provided by Prof. Sanjay Kumar's laboratory at UC Berkeley (the naïve, pre-modification U251 cell line was obtained from the UC Berkeley Tissue Culture Facility, originally sourced from the American Type Culture Collection). Cells were maintained in tissue culture flasks in a standard cell culture incubator (Heracell 150i) at 5% CO2 and 37°C, in DMEM (Invitrogen 10566016) supplemented with 10% FBS (Gemini Bio-Products Benchmark 100-106), 1% penicillin/streptomycin (Life Technologies 15140-122), 1X sodium pyruvate (Thermo Fisher 11360070), and 1X non-essential amino acids (Life Technologies 11140-050 100X stock). The cells were passaged at a density of 1:10 to 1:40 after reaching ~80% confluency by detaching with 0.05% Trypsin-EDTA (Life Technologies 25300120), centrifuging for 3 minutes at 1000 RPM, and resuspending in completed media to reseed.

BT474 human breast cancer cells were purchased from the UC Berkeley Biosciences Divisional Services Cell Culture Facility. Cells were maintained in tissue culture flasks in a standard cell culture incubator (Heracell 150i) at 5% CO_2 and 37°C, in DMEM (Invitrogen 10566016) supplemented with 10% FBS (Gemini Bio-Products Benchmark 100-106) and 1% penicillin/streptomycin (Life Technologies 15140-122). The cells were passaged at a density of 1:2 to 1:8 after reaching ~80% confluency by detaching with 5 mM EDTA in PBS (Invitrogen 15575-038 diluted in sterile 1X PBS: Life Technologies 10010049), centrifuging for 3 minutes at 1000 RPM, and resuspending in completed media to reseed.

Cell lysis monitoring experiments. We compared diffusion profiles of cells lysed after settling in 32 μm diameter, 40 μm high microwells within 1 mm thick gels. Microwell gels and lysis gels (18x18 mm in area) were prepared and equilibrated in PBS for >12h as described above.

To settle cells in microwells, we followed a procedure similar to that used for single-cell western blotting[62]: U251-turboGFP cells were detached using 0.05% trypsin-EDTA (Life Technologies 25300120), resuspended in PBS (Life Technologies 10010049) at a concentration of 100 000 cells/mL, and filtered using a cell strainer (Corning 352235). The 18x18 mm microwell gels were placed microwell side up in a 60 mm tissue culture dish. ~100 μL cell solution was pipetted onto the surface of each microwell gel (to cover but avoid spillage over the edge of the gel) and spread to cover the full array of microwells. The cells were allowed to settle for 5 minutes on ice, gently agitating every ~2 minutes, before rinsing with 1-3 mL PBS by tilting the tissue culture dish at a ~40° angle, pipetting PBS at the top surface of the microwell gel, and allowing it to flow over the surface of the microwell gel into the bottom of the petri dish. After rinsing was complete, the excess PBS/cell solution was aspirated for biohazard disposal.

To facilitate monitoring, each microwell gel was immobilized within a 60 mm petri dish by pipetting 200 μL of a warmed solution of 5% agarose (Invitrogen 16500) in PBS (Life Technologies 10010049) beside the gel and allowing it to gel at room temperature (in contact with the edge of the gel and the petri dish). Before lysis, excess fluid was removed from the gel by tilting the petri dish and wicking away the fluid layer by bringing a folded Kimwipe into contact with the corner of the gel (not touching cell-containing regions). The petri dish was then secured to the stage of an Olympus IX71 microscope for monitoring with a 4X or 10X air objective. Fluorescence excitation was provided by an X-Cite source (Excelitas Technologies) through a GFP filter set (Chroma 49011 ET), and fluorescence was measured using an EM-CCD camera (Andor

iXon). Time-lapse images of the turboGFP fluorescence were captured using the MetaMorph® imaging software (Molecular Devices). After focusing, setting up the imaging settings and initiating the time-lapse, the lysis gel was carefully placed on top of the cell-containing gel, starting with one corner and then smoothly bringing the rest in contact to reduce bubble entrapment between the two gels. The time at which the lysis gel was placed in the time-lapse series was recorded. The lysis gel was a 20%T, 10% Rhinohide shield gel equilibrated in 2X RIPA-like lysis buffer.

The lysis monitoring data were analyzed using custom scripts written in MATLAB®. At each time point, the cells were segmented using adaptive thresholding of the median filtered (3x3 neighborhood) image. The segmentation was improved using morphologic open and close operations, and the centroids of the segmented cells were computed and stored. The MATLAB® particle tracking library (based on a previous IDL implementation[82]) made publicly accessible by Prof. Daniel Blair and Prof. Eric Defresne[83] was used to track the centroids of each cell over the course of the experiment, although minimal drift was observed. The maximum fluorescence intensity and total fluorescence intensity in a 100 μm diameter circle surrounding the centroid of each segmented cell were tracked for each time point. All pixel intensities were background-subtracted using the average fluorescent intensity of the background region at each time point, taken to be the image regions greater than 30 μm away from all segmented regions.

Finite-element modelling of protein diffusion. We used finite-element modelling of dilute species transport in COMSOL® Multiphysics to predict protein concentrations during lysis and electrophoresis. The simulation geometries for the Z-directional simulations are presented in the cross-sectional view shown in **Figure 4**b. 2D axisymmetric models were used for all simulations due to the inherent symmetry of the geometry. Diffusion coefficients in free solution portions of the model were estimated from the Stokes-Einstein equation[51], while in-gel diffusion was estimated from the free-solution diffusivity using the methods presented by Park, *et al.*[52] Protein hydrodynamic radii were estimated from the number of amino acids[84]. Thermodynamic partitioning of protein was simulated using flux boundary conditions relating in-gel concentration to in-solution concentration using a partition coefficient $k=C_{gel}/C_{solution}$. Partition coefficients were estimated using the Ogsten model[85] (assuming size-exclusion partitioning), using estimates of fibre radius from Tong and Anderson[68] and hydrogel volume fraction from the data presented by Baselga et al[86]. A temperature of 4°C was assumed for all simulations except the comparison with the single-cell western blot platform, which assumed 10°C for both platforms. The diffusion and partition coefficients for each protein at 4°C are presented in Table 1.

Table 1. Protein hydrodynamic radii (r_H), diffusion coefficients (D) and partition coefficients (k) used in finite-element modelling of diffusion during lysis and electrophoresis.

Protein	r_H [nm]	D_{sol} [m^2/s]	$D_{7\%T}$ [m^2/s]	$D_{20\%T}$ [m^2/s]	$k_{7\%T}$	$k_{20\%T}$
turboGFP	2.3	6.61×10^{-11}	1.36×10^{-11}	9.49×10^{-13}	0.501	0.0415
BSA	3.01	5.05×10^{-11}	7.90×10^{-12}	3.49×10^{-13}	0.344	0.00744
HER2	3.76	4.04×10^{-11}	4.88×10^{-12}	1.39×10^{-13}	0.213	8.16×10^{-4}

In each model, gel-solution boundaries were modelled as flux boundary conditions taking size-exclusion partitioning into account. The edges of each model were modelled as flux boundary conditions permitting protein to freely leave the model; however, the simulation region was sufficiently large (500x500 μm) that changing these boundary conditions to no flux resulted in negligible change to the modelled concentration profiles. The initial protein concentration in the cell region was 2 μM, while the initial concentration elsewhere in the model was zero. In models of the single-cell western blotting platform, the bottom surface of the gel was modelled as no flux to model the presence of the glass slide present in that system. The model was meshed with a physics-controlled mesh calibrated for fluid dynamics, and a user-controlled override with maximum element size of 0.5 μm was used in the microwell and thin fluid layer regions to ensure sufficient mesh density in these smaller regions.

A time-dependent study was used to model the protein concentration profile during lysis and electrophoresis. To model both in the same diffusive model, the diffusion and partition coefficients were set as step functions. For the first 25s of the model (the lysis portion), the diffusion and partition coefficients were set as in Table 1. After this 25s lysis period, all partition coefficients were set to 1, and the diffusion coefficients in all regions of the model were set to those for 7%T gel (the separation gel), effectively simulating instantaneous injection of the full protein profile into a separation gel. While this method is straightforward and does not require modelling of the electrophoresis physics, it provides a conservative (over-) estimate of Z-directional diffusional spreading because it does not model stacking of the protein band as it is injected from free solution into the gel.

After running the model, we assessed the maximum protein concentrations in the simulated geometry. We also assessed the integrated protein intensities (the protein concentrations at each radial (x) location, integrated in z) to model the wide-field microscopy imaging measurements in which fluorescence from the full Z region is integrated into a 2D image. These intensities were compared with the experimental lysis monitoring data.

Single-cell separations. Adherent U251 glioblastoma and BT474 breast tumor cells were detached from culture flasks with 0.05% Trypsin-EDTA (Life Technologies 25300120) (U251) or 5 mM EDTA (Invitrogen 15575-038) in PBS (BT474) and resuspended in cold PBS (Life Technologies 10010049) at a concentration of 1.5×10^6 cells/mL. For viability staining to aid in microwell occupancy assessment, BT474 cells were stained with Calcein-AM in incomplete

DMEM for 20 minutes at room temperature prior to resuspension. Cell suspensions were kept on ice and filtered through a cell strainer (Corning 352235) to reduce cell aggregates immediately prior to settling.

1 mm-thick micropatterned separation gels were stored in 1X tris-glycine (Bio-Rad) and buffer-exchanged to lower conductivity sucrose-dextrose dielectrophoresis buffer (DEP buffer: 2.39 g/L HEPES (VWR 3638C017), 80.7 g/L sucrose (Sigma-Aldrich S0389), 4.5 g/L dextrose (Fisher D16-500), 11.1 mg/L $CaCl_2$ (FisherC79-500); pH adjusted to pH 7.5 with NaOH[87] at least 10 minutes prior to cell settling. To settle the cells, gels were placed microwell side up inside of a 35 mm tissue culture dish. 25 µL of single-cell suspension was supplied to each 9x9 mm gel (by first pipetting 15 µL onto the gel surface, spreading with a pipette tip while taking care not to perforate the gel surface, and subsequently dispensing another 10 µL onto the surface. Cells were allowed to gravitationally settle for 20 minutes, agitating the gel periodically and covering the gel with the lid of the 35 mm tissue culture dish (to reduce evaporation). Settled cells were checked at the 10-minute mark, and if the cell suspension had aggregated towards the centre of the gel, an additional 10 µL of cell suspension was supplied to the gel edges.

After 20 minutes of settling, gels were rinsed by holding the petri dish at a ~40º angle and pipetting 0.5 mL of DEP buffer onto the top corner of the gel, allowing the fluid stream to wash over the full gel into the tissue culture dish. The wash fluid was aspirated for biohazardous waste disposal, and the wash was repeated with an additional 0.5 mL of DEP buffer before pipetting ~40 µL DEP buffer on top of the gel to prevent drying during imaging. Tiled images of the settled cell fluorescence were captured using the ScanSlide plugin for the MetaMorph® imaging software (Molecular Devices), using an Olympus IX51 inverted wide-field fluorescence microscope fitted with an X-Cite® illumination source (Excelitas Technologies), GFP filter set (Chroma 49011 ET), 4X objective, and CoolSNAP HQ2 CCD camera (Teledyne Photometrics). Cell occupancy was calculated from a MATLAB® script that analyzed tiled live-cell brightfield and fluorescence images, determined whether there was a fluorescent object in a region surrounding each microwell (via thresholding segmentation) and, if found, displayed the region and prompted user input of number of cells in the microwell region.

Aliquots of lysis buffer (4 mL) were prepared by dissolving urea to a final concentration of 8 M in 2X RIPA-like lysis buffer in a water bath set to 55ºC. Lysis gels (14x14x1 mm) were stored in 2X RIPA-like lysis buffer and transferred to aliquots of urea lysis buffer as soon as the urea had dissolved (10-60 minutes prior to running the separations). The lysis gels in buffer aliquots were heated to 55ºC in a water bath until immediately prior to use, agitating periodically to ensure the solution was well mixed.

After cell settling and live-cell imaging, 4 mL 2X tris-glycine (diluted from Bio-Rad 1610734 10X stock) was pipetted into the tissue culture dish containing the separation gel and incubated for 1 minute to reduce the concentrations of potentially unwanted ions. A 10x10x1 mm filter paper (cut to size from Thermo Fisher Scientific western blotting filter paper) was hydrated in the heated lysis buffer aliquot and placed on the anode. The separation gel was placed (microwell side up) on top of the filter paper immediately after tris-glycine incubation, placing slowly from one corner to reduce bubble entrapment between the layers. The lysis gel was removed from the buffer aliquot and placed on top of the separation gel, again placing gradually so as to not introduce bubbles

between the gels. The lysis timer was started as soon as the lysis gel was placed, and the electrode system was closed by placing the cathode on top of the lysis gel. After 25s lysis, the separation was initiated by supplying 80 mA of constant current (typically yielding 13-16V initial voltage for an average electric field of 43-53 V/cm across the gel stack) using a DC power supply (Bio-Rad PowerPac Basic) and recording the voltage at 5s intervals during electrophoresis. After electrophoresis was complete, the power supply was stopped, electrode system opened, and 45s photocapture was completed using a Hamamatsu Lightningcure LC5 UV source. The gel was then rinsed briefly in deionized water before equilibrating in tris-buffered saline with Tween® (1X TBST, from Cell Signaling Technology 9997S 10X stock) overnight to remove any residual lysis buffer (exchanging the buffer after 2h). Projection electrophoresis gels probed with F(ab) fragments were blocked overnight in 5% BSA in TBST at 4°C or for between 2-4h on a shaker at room temperature prior to immunoprobing.

Immunoprobing and imaging. Single-cell projection electrophoresis immunoblotting gels were probed either diffusively (for initial characterization experiments using labelled F(ab) fragments in **Figure 4**) or electrophoretically (using standard primary and fluorescently-labelled secondary antibodies in **Figure 1** and **Figure 5**). All probing wash steps were performed using an electrophoretic wash platform.

In-gel probing requires high concentrations of immunoprobes to mitigate size-exclusion partitioning effects[62,68]. To minimize reagent consumption, we probe single-cell western blotting gels using minimal solution volumes. For the projection electrophoresis system, larger probe volumes are required to probe thicker gels; as such, we deliver probes using thin (0.5-1 mm thick) hydrogel layers to provide even probe delivery to all regions of the gel. Fluid, in contrast, tends to pool around gel edges, resulting in brighter probed signal at the gel edge. Constituents and fabrication parameters of probe delivery gels are described in Table 2.

Table 2. Probe delivery gel fabrication parameters for electrophoretic and diffusive probing.

Gel type	Final agarose concentration after probe dilution	Antibody probes	Gelation time	Fabrication setup
Primary antibody agarose electrophoretic probe delivery gel	1.5% g/ml (dissolved in 1X tris-glycine) UltraPure LMP Agarose, (Thermo-Fisher: 16520050)	For the studies reported in Figure 5 and Supplementary Figures 4-6), dilutions from each stock were: (1) Rb α-actinin (1:15, 6.67% v/v) *&* (2) Gt α-GAPDH (1:10, 10% v/v). For the studies reported in Figure 1 and Supplementary Figure 8), dilutions from each stock were: (1) Ms α-PTBP1 (1:10, 10% v/v) *&* (2) Gt α-GAPDH (1:10, 10% v/v)	5 mins on ice pack	Glass plate and glass slide
Secondary antibody agarose electrophoretic probe delivery gel	1.5% g/ml (dissolved in 1X tris-glycine)	For the studies reported in Figure 5 and Supplementary Figures 4-6), dilutions from each stock were: (1) Dk α-Rb AF555 (1:10, 10% v/v) *&* (2) Dk α-Gt AF488 (1:10, 10% v/v). For the studies reported in Figure 1 and Supplementary Figure 8), dilutions from each stock were: (1) Dk α-Ms AF555 (1:20, 5% v/v) *&* (2) Dk α-Gt AF488 (1:20, 5% v/v)	5 mins on ice pack	Glass plate and glass slide
hFAB agarose diffusive probe delivery gel	1.5% g/ml - dissolved in 1X tris-buffered saline solution with Tween® (1X TBST, from Cell Signaling Technology 9997S 10X stock)	1:10 (10% v/v) dilution from stock of *either*: (1) Bio-Rad hFAB Rhodamine α-GAPDH *or* (2) hFAB Rhodamine α-tubulin	5 mins on ice pack	Glass plate and glass slide

For diffusive probe delivery, Bio-Rad hFAB probes for GAPDH (12004167) or tubulin (12004165) were mixed at a 1:10 dilution with low melting temperature agarose (Invitrogen 16520-050) solution. Agarose was dissolved in 1X tris-buffered saline solution with Tween® (TBST) to yield a final concentration of 1.5% (w/vol) after probe dilution, and maintained on a hotplate with spin bar at a temperature of ~40°C until mixing with the probes. Temperature of the solution immediately after mixing typically read ~30°C. The agarose gel was then immediately cast from the agarose-probe solution by pipetting between a heated (to ~30°C) glass plate and microscope glass slide, separated by gel casting spacers (C.B.S. Scientific GelWrap, 0.5 mm thickness). After casting, the glass plate setup was carefully moved onto a cold pack and the agarose was permitted to gel for 5 minutes before carefully disassembling the stack, cutting the gels to match the size of the separation gels, and immediately setting up the probing stacks. Each

high-density separation gel was sandwiched between two 0.5 mm thick agarose probe delivery gels in a 24-well plate (with surrounding wells filled with water), sealed with a plate sealer, and incubated at 4°C in the dark for 40 hours.

For electrophoretic probe delivery, agarose probe delivery gels were fabricated in the same manner as the diffusive probe delivery gels described above; however, gels were fabricated at 1 mm thickness. Primary antibodies were electrophoretically introduced, incubated, and electrophoretically washed; this process was then repeated for fluorescently-labelled secondary antibodies. Primary antibodies used were Rb α-actinin (CST 6487, lot 2), Ms α-PTBP1 (Sigma WH0005725M1, lot J4241-3H8), and Gt α-GAPDH (Sigma SAB2500450, lot 6377C3); secondary antibodies were Dk α-Rb AF555 (Invitrogen A-31572, lot 2017396), Dk α-Ms AF555 (Invitrogen A-31570, lot 2045336), and Dk α-Gt AF488 (Invitrogen A-11055, lot 2059218). Immediately after casting the antibody probe delivery gel, a stack was set up for electrophoretic probe introduction. The probe delivery gel was placed against the flat (non-microwell-stippled) side of the separation gel. The stacked gel setup was sandwiched between two pieces of western blotting filter paper (Thermo Fisher Scientific 84783) held together using a laser-cut acrylic holder with a cut-out for the gel stacks. The holder was used to suspend the gels (with the separation gel facing the anode (+) and delivery gel facing the cathode (-)) in a slab-gel blotting module (Invitrogen X-Cell II) filled with 1X tris-glycine with 0.5% Triton X-100. Probes were transferred from the delivery gel into the separation gel at an electric field of 8 V/cm for 13 minutes; the stack was then disassembled and the separation gels were incubated at room temperature on a glass slide within a hydration chamber for 2 hours for primary antibody binding, or 1 hour for secondary antibody binding.

After each probe incubation step (primary and secondary antibodies), projection electrophoresis gels were electrophoretically washed by sandwiching between two filter papers soaked in 1X tris-glycine with 0.5% Triton X-100 (held in place by custom laser-cut acrylic with a cut-out for the gels, which suspended the gels within the chamber of a slab-gel blotting module. Separation gels were submerged in 1X tris-glycine with 0.5% Triton X-100 for ~1 min for rehydration immediately before electrophoretic washing. The blotting module was also filled with 1X tris-glycine with 0.5% Triton X-100. Gels were electrophoretically washed for 15 minutes at an electric field of 12 V/cm.

Gels were confocal imaged through a #1.5 coverslip using a Zeiss LSM 880 laser-scanning confocal microscope fitted with a 20X water dipping objective (NA=1.0, Zeiss W Plan APO 20x/1 DICIII). A confocal Z-slice spacing of 5 μm was chosen, and volumes extending ~100 μm past visible fluorophore bands were imaged. As we were not quantifying or comparing protein abundance, excitation laser powers were adjusted to permit fluorescence visibility depending on the sample brightness, as fluorescence intensities were not compared between cell separations. Similarly, images were brightness and contrast-adjusted in Fiji[79] (based on ImageJ[80], National Institutes of Health) to ensure visibility of protein bands.

For full-gel imaging, gels were imaged using a Zeiss Lightsheet Z.1 system fitted with a 5X detection objective (Zeiss EC Plan-Neofluar 420330-8210) and 4X light sheet forming objectives (Zeiss LSFM 400900-9010). Samples were excited with 488 nm and 561 nm lasers and detected using two pco.edge sCMOS cameras (with filter sets for AlexaFluor® 488 and AlexaFluor® 555). The samples were mounted to #1.5 coverslips using superglue at the gel corners, and the coverslip was glued to a custom 3D printed adapter to suspend the gel within the imaging chamber. The gels

were imaged facing the detection objective (not imaged through the mounting coverslip). Tiled Z-stack images with 5-6 µm Z-slice spacing were acquired over the full gel volume, with 10% overlap between acquisition fields of view to ensure complete gel coverage. 49-56 Z-stack fields of view were typically required to cover the full gel area, each with 200-300 Z-slices.

Confocal and light sheet microscopy datasets were analyzed using custom analysis scripts in MATLAB®, similar to those described above for purified protein datasets. Zeiss CZI confocal Z-stacks and associated metadata were imported into MATLAB® (MathWorks®) using the MATLAB® Bio-Formats libraries provided by the Open Microscopy Environment[81]. The analysis workflow is described in Supplementary Figure 8. 3D datasets are made up of 2D (X-Y) slice imaged that are each processed to assess the 3D positional data for each separated protein peak). Intensity profiles were background-subtracted by subtracting the average intensity of a 5-pixel (light sheet) or 20-pixel (confocal) border surrounding each X-Y ROI from each ROI pixel at each Z location prior to summing the intensities to generate Z-intensity profiles. Thin (10-pixel for confocal and 5-pixel for light sheet) borders between the ROI and background regions were used to assess the background-subtracted noise of the measurement to compute signal-to-noise ratios for each protein peak. Protein peaks corresponding to separation lanes were quantified (passing quality control) if: (1) there was a segmented fluorescence spot, (2) the Gaussian fit to the Z-intensity profile of the peak region had an R^2 of the Gaussian intensity profile fit of >0.7, and (3) the Gaussian fit had a signal-to-noise ratio (Gaussian peak fit amplitude divided by twice the standard deviation of the background-subtracted noise calculation region over the Z region of the protein peak) of >3. A schematic representing the analysis workflow for tiled light sheet images (similar to the workflow used for confocal images but without the tiled functionality) is presented in Supplementary Figure 9.

3.3 Results

Establishing projection electrophoresis as an analytical tool. In lieu of serial interrogation and electrophoretic analysis of individual mammalian cells, projection electrophoresis **(Figure 1**a) yields synchronous, concurrent analyses of hundreds of single cells. Compared to serial cell measurements, the parallel approach reduces assay-induced protein expression heterogeneity (**Figure 1**b). After in-gel immunoprobing for the protein targets glyceraldehyde 3-phosphate dehydrogenase (GAPDH, involved in glycolysis, transcription, and apoptosis) and polypyrimidine tract-binding protein 1 (PTBP1, RNA-binding protein involved in cellular processes including splicing), projection electrophoresis yields 3D data (with X-Y position describing the originating microwell, Z-position describing protein size, **Figure 1**c-g). Mean Z-direction migration distances were 199±9 μm for PTBP1 (57 kDa) and 346±7 μm for GAPDH (37 kDa). Furthermore, the multifunctional, micropatterned polyacrylamide gel (PAG) serves as the cell isolation device, lysis vessel, separation matrix, and protein capture scaffold. This multifunctional gel thus facilitates *in situ* lysis, electrophoresis, and blotting, mitigating losses incurred in sample transfer steps, while synchronous analysis and fast assay times yield high assay throughput and drastically reduced sampling delays between cells in a population.

a Projection Electrophoresis (EP): parallel single-cell immunoblotting

Projection EP device | 100s of cells in microwells | Simultaneous *in situ* lysis | Simultaneous *in situ* protein separation (Z-direction) | Immunoprobing | Fluorescence imaging readout and data processing

b Capillary EP: serial interrogation of single cells
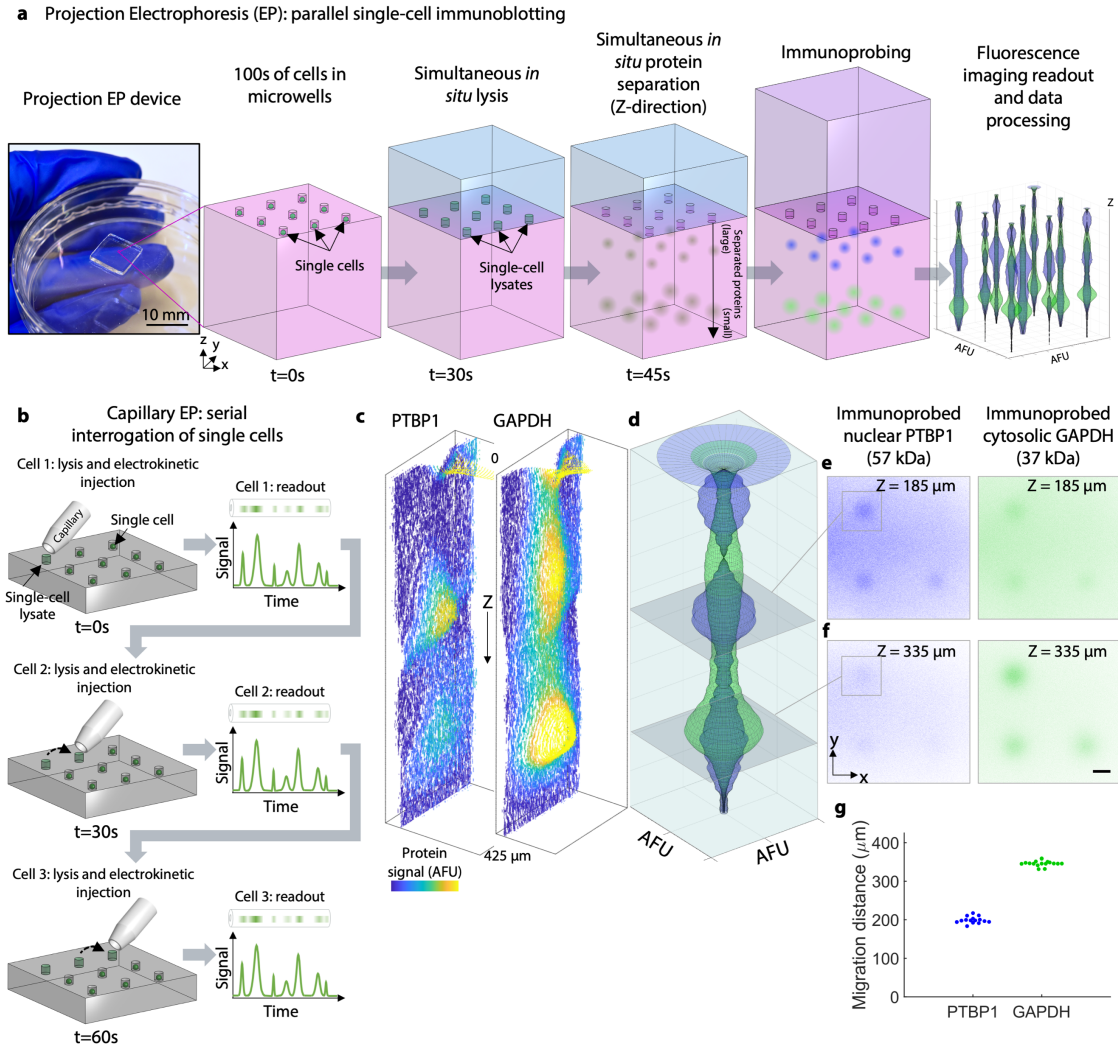
Figure 1. Projection electrophoresis simultaneously lyses and separates both nuclear and cytosolic proteins from hundreds of single cells. **(a)** Projection electrophoresis device photograph and workflow schematic. A 9x9 mm projection electrophoresis polyacrylamide gel contains >1000 microwells that each serve as a separation lane. Cells in polyacrylamide gel microwells are lysed *in situ* using a lysis buffer-soaked hydrogel delivery matrix, and lysate is then electrophoretically injected into the polyacrylamide and proteins separate by size through the depth of the gel. After separation, proteins are covalently linked to the gel matrix using a UV-initiated capture. All cells are lysed and analyzed simultaneously, the active assay time (from cell lysis to photocapture) is less than 90s, and *in situ* analysis reduces potential losses from transfer steps. **(b)** In contrast, capillary electrophoresis analyzes cells in series, with each cell lysed and proteins separated at a different time. **(c-f)** Different visualizations of Z-directional protein separation in a single separation lane. **(c)** X-Z (Y-summed) contour plots of background-subtracted protein signal within the separation lane for nuclear and cytosolic example proteins. Protein signal is visualized as peak height and false-coloured. **(d)** Z-directional intensity profiles (summed fluorescence intensity in arbitrary fluorescence units, AFU, vs. Z) for PTBP1 (nuclear, blue) and GAPDH (cytosolic, green) in the same lane, revolved around the Z-axis to generate a 3D rendering of fluorescence distribution. **(e-f)** Representative confocal X-Y slice images (representative of 9 confocal stacks acquired of different regions of 2 independent separation gels) for separated PTBP1 (blue) and GAPDH (green) at two Z-depths into the gel (**(e)** at the 185 µm depth of the PTBP1 band; **(f)** at the 335 µm depth of the GAPDH band). Each slice image shows 4 separation lanes, 3 of which were occupied by BT474 cells prior to analysis. Overlaid squares depict X-Y regions of interest for the lane plotted in the left and middle sub-

59

panels, over which fluorescence intensities were summed to yield Z-directional intensity profiles. Scale bar represents 50 μm. **(g)** Quantified Z-migration distances for PTBP1 (57 kDa) and GAPDH (37 kDa) from n=15 (PTBP1) and n=17 (GAPDH) separation lanes.

We first sought to verify the separation mechanism governing protein electrophoresis in the concurrent analyses (**Figure 2**a-b). To understand the protein separation mechanism, we assessed electromigration of a ladder of well-characterized protein standards (donkey immunoglobulin anti-mouse IgG, IgG: 150 kDa; bovine serum albumin, BSA: 66.5 kDa; ovalbumin, OVA: 42.7 kDa, each labelled with AlexaFluor® dyes). When purified protein solution is pipetted on top of the gel block (gel block face stippled with microwells), the protein solution preferentially partitions into the microwells (versus the hydrogel), thus providing a convenient, well-controlled means for sample loading into each microwell sample injector. To minimize 3D diffusional spreading during PAGE, we designed an ultra-short separation axis (1 mm, defined by the gel block thickness) and rapid (<1 min) protein PAGE duration. Upon completion of PAGE, the multifunctional gel was toggled from separation matrix to a protein capture scaffold using a 45-s exposure to UV illumination[45].
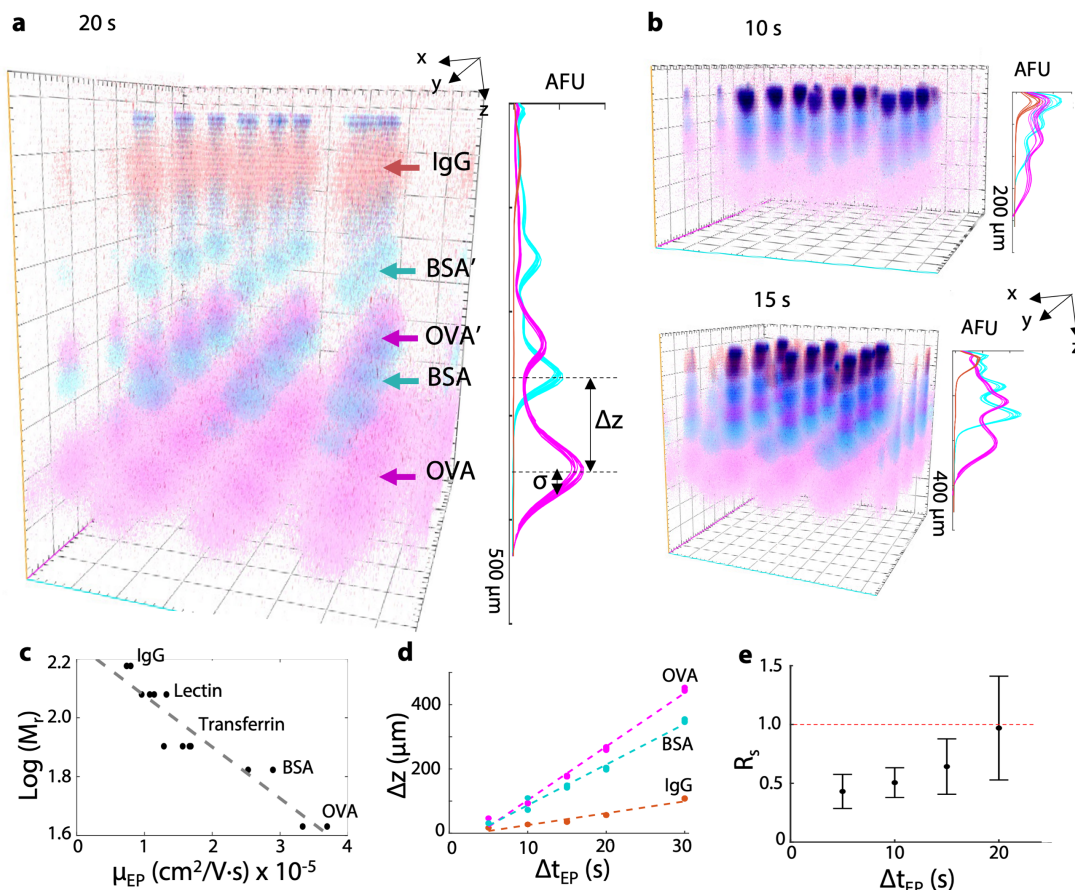
Figure 2. Projection electrophoresis supports protein PAGE. **(a)** Confocal imaging of PAGE of fluorescently labeled protein ladder at 20 s elapsed separation time. Each ladder sample is injected from a 32 μm diameter microwell (x-y plane) with PAGE along the z-axis of the gel block. Summing the background-subtracted fluorescence intensities at each pixel in the x-y separation lane region of each slice image (a 300 pixel, 102 μm square region centered on each microwell) yields a z-intensity profile

for each lane, with peak-to-peak displacement Δz and peak width σ (10%T PA separation gel containing 10% Rhinohide). **(b)** 3D renderings and Z-intensity profiles are plotted for (i) 10s electrophoresis and (ii) 15s electrophoresis in 10%T polyacrylamide gels containing 10% Rhinohide for comparison with the data for 20s electrophoresis shown in (a). **(c)** The electrophoretic mobility of the proteins depends log-linearly on protein molecular weight. Each plotted point represents an electrophoretic mobility calculated from linearly fitting migration distance vs. electrophoresis time data from 11-17 segmented separation lanes in n=5 7%T PA separation gels containing 10% Rhinohide (5 electrophoresis times). Linear fitting yields $\log(M_r)=1.7x10^4\mu_{EP}+2.25$ ($R^2=0.89$). **(d)** Electromigration distance depends linearly on electrophoresis time, thus proteins migrate at constant velocity during PAGE. Migration distances are plotted from protein bands originating from 11-17 nearby microwells in two independent 7%T PA gels containing 10% Rhinohide; 33 mA constant current; 52 V/cm initial, 2 gels for each migration time. Linear fitting yields OVA migration=16.7t-63.42; BSA migration=12.64t-39.3; IgG migration=3.69t-11.54. **(e)** Separation resolution R_s for BSA and OVA peaks in 10%T PAGE gels containing 10% Rhinohide. Each point depicts the mean and standard deviation of the R_s calculation from the median migration distances and peak widths from n=4 independent separation gels.

We observed **(Figure 2**c) a log-linear relationship of electromigration with molecular mass, as expected in size-sieving gel electrophoresis[46]. Further, in this unique format, we observed constant-velocity and size-dependent electromigration for the ladder and additional protein assayed (**Figure 2**d; electrophoretic mobilities of OVA: 3.3-$3.7x10^{-5}$ cm^2/Vs; BSA: 2.5-$2.9x10^{-5}$ cm^2/Vs; transferrin: 1.3-$1.7x10^{-5}$ cm^2/Vs, lectin: 0.96-$1.14x10^{-5}$ cm^2/Vs; IgG: 7.4-$8.0x10^{-6}$ cm^2/Vs). Constant-velocity migration required mitigation of deleterious effects of electrolysis (i.e., buffer pH changes, bubble formation at the electrodes), which increased the R^2 of linear fits to the protein migration data from 0.87 ± 0.06 to 0.97 ± 0.03 for the three ladder protein species (Supplementary Figure 1). For BSA and OVA ladder species, both a protein monomer and dimer are resolvable, as expected in high performance protein PAGE[47–50]. Having established the separation mechanism, we next estimated the PAGE performance by assessing the separation resolution (R_S). For two ladder proteins (OVA, BSA) in a 1-mm thick 10%T PA gel volume (**Figure 2**e), the R_s exceeded 1.0 within 20 s of PAGE, yielding fully resolved species.

Based on the dominant separation mechanism and rapid protein separation, analysis of the purified protein ladder solution suggests that projection electrophoresis is suitable for analytical-quality protein analysis. The high performance of the rapid microfluidic protein analysis described here is in contrast to another 3D system, designed for preparatory Z-direction separation performance, as previously demonstrated for bulk samples using a multilayered gel to coarsely fractionate small proteins (14-77 kDa) from large proteins (20-343 kDa)[44]. In terms of throughput, each purified protein projection electrophoresis gel (100 μm microwell pitch) contains >4000 microwells, facilitating >4000 parallel (replicate) purified protein separations for a total active assay throughput of 44 separations per second (not including readout time). For comparison, Capillary Array Electrophoresis of a single sample yields a throughput of 5 separations per second[15].

Device design is informed by 3D diffusion of target proteins. Given the open microfluidic design of the projection electrophoresis device that uses a microwell array to perform sample isolation and preparation, with an abutting gel volume that performs the analytical functions (protein PAGE, immunoblotting), we sought to understand physics-based factors that set the minimum acceptable microwell-to-microwell spacing (microwell pitch, δ_{well}). The microwell pitch, in turn, sets the maximum number of concurrent protein PAGE separations per projection electrophoresis device. As illustrated schematically in **Figure 3**a, the δ_{well} spacing is influenced

by the length scale of diffusional band broadening (σ_{xy}, in X-Y plane) during protein PAGE along the Z-axis. As design guidelines, the throughput of each single-cell projection electrophoresis device (number of single cells assayed per device) will be a function of ℓ_{well} (sets separation lane density) and overall usable device dimensions (**Figure 3**b). As ℓ_{well} depends linearly on σ_{xy}, the maximum lane density is inversely proportional to σ_{xy}^2, as computed in **Figure 3**c. Two design rules are plotted: at $\ell_{well} > 4\sigma_{xy}$, we would estimate <5% protein overlap between neighboring lanes, while at the more conservative $\ell_{well} > 6\sigma_{xy}$, we would estimate <0.3% protein overlap assuming Gaussian protein distributions.
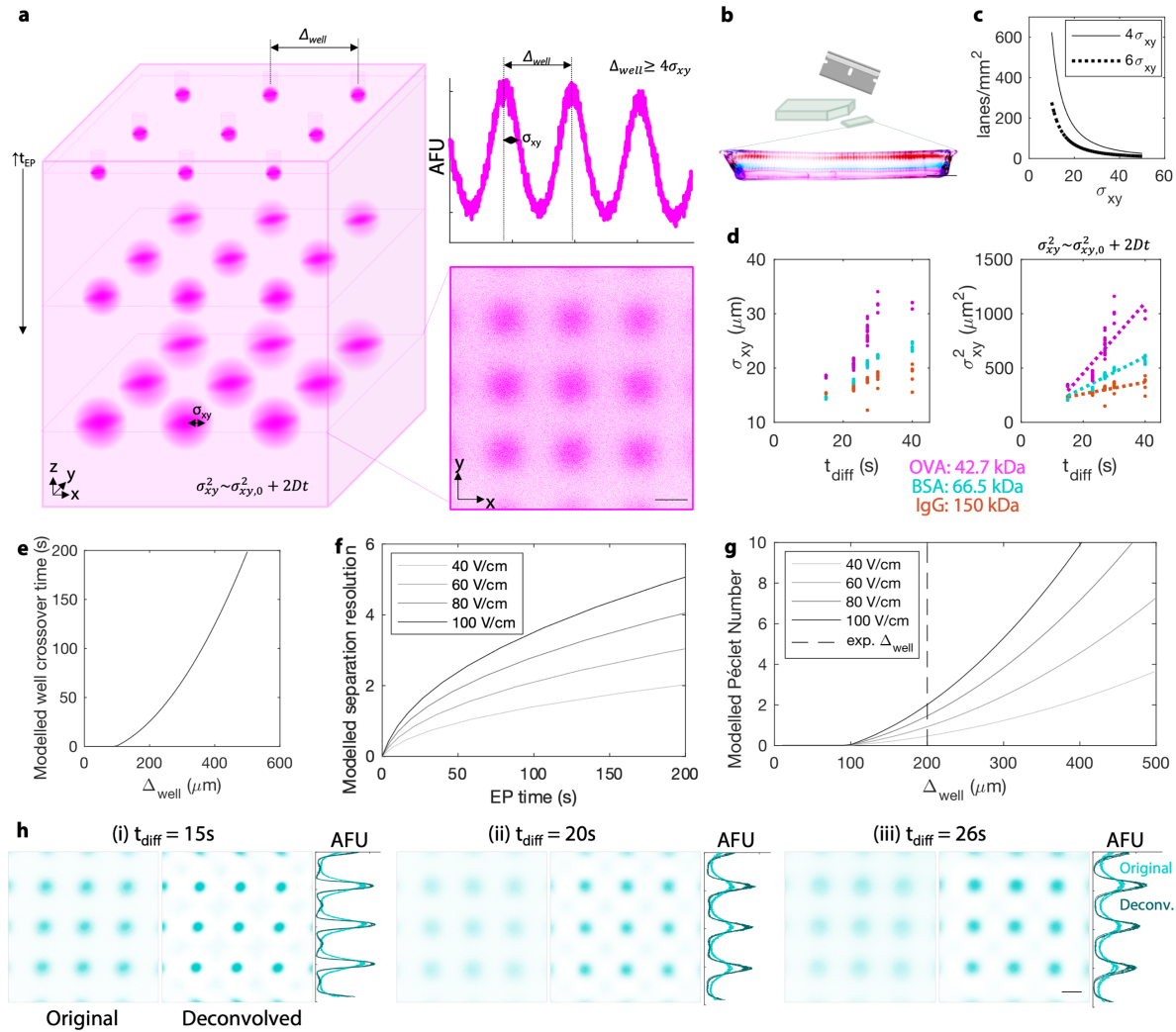
Figure 3. The physics of 3D diffusion dictate projection electrophoresis device design and inform image analyses. **(a)** Lane density (limited by minimum spacing between separation lanes Δ_{well}) is dependent on separated protein x-y band width (σ_{xy}) to avoid microwell-microwell crosstalk. σ_{xy} in turn depends on 3D diffusion of the injected protein. Simulated data shown in left schematic; measured OVA data shown in micrograph and intensity profile (representative of two independent separation gels). Scale bar represents 100 µm. **(b)** Throughput is a function of both lane density and usable gel area; separated protein bands parallel to the gel edges in a cross-sectional image of the gel show uniform migration across the gel. Scale bar represents 1 mm. **(c)** Theoretical maximum lane density at a spacing of $4\sigma_{xy}$ (~5% overlap between lanes) and $6\sigma_{xy}$ (~0.3% overlap between lanes). Maximum lane density is inversely proportional to σ_{xy}^2. **(d)** Measured diffusional x-y band broadening (Gaussian fit peak width σ_{xy}) from purified proteins initially partitioned into 32 µm microwells, as a function of in-gel diffusion time (t_{diff}). Left: σ_{xy} vs. t_{diff}. Right: σ_{xy}^2 vs. t_{diff} with linear fits ($\sigma_{xy}^2 = \sigma_{xy,0}^2 + 2Dt_{diff}$). After 10s EP, we measure $\sigma_{xy} < 30$ µm for all proteins, suggesting that 200 µm microwell spacing is sufficient. Linear fitting yields OVA $\sigma_{xy}^2 = 32.5t_{diff} - 198$ (R²=0.75); BSA $\sigma_{xy}^2 = 14.3t_{diff} + 29.8$ (R²=0.88); IgG $\sigma_{xy}^2 = 5.41t_{diff} + 153$ (R²=0.42). **(e)** Modelled time for ovalbumin bands to diffuse into the neighboring lane, as a function of microwell spacing Δ_{well}. **(f)** Modelled separation resolution for BSA and OVA, as a function of EP time and electric field strength. **(g)** Modelled Péclet number (defined as the ratio of the time to reach a BSA-OVA separation resolution of 1 to the time at which the OVA band is expected to diffuse into the neighboring separation lane. **(h)**

Physics-driven postprocessing. For each confocal slice (BSA, 7%T gel), the original image, that after physics-driven postprocessing (deconvolution of a point spread function modeling 3D diffusion), and summed pre- and post-deconvolution intensity profiles for a 100 µm region surrounding each row of protein bands are shown. Each image pair is scaled to the maximum of the (higher-intensity) deconvolved image. Scale bar represents 100 µm.

During electromigration, protein peaks will diffuse in three dimensions, with diffusion along the Z-axis determining separation resolution (R_S) and diffusion in X-Y determining the minimum _well_. Diffusional spreading of protein bands in all three dimensions depends on protein molecular mass, temperature, time, and gel density (pore size)[51,52]. To assess the impact of protein diffusion on setting _well_, we assessed the well-characterized fluorescently labeled OVA/BSA/IgG protein ladder during protein PAGE in a 7%T gel projection electrophoresis device. For each time point analyzed by confocal imaging, we determined the Z position of the maximum of the summed fluorescence intensity, for an X-Y region of interest surrounding the each microwell injector. At this Z position, we assessed X-Y resolution by Gaussian fitting X and Y intensity profiles and extracting the mean fitted peak width σ_{xy}. For duplicate gels of 5 electrophoresis times, we plotted the squared peak width vs. time in gel, fitting to the expected diffusional peak spreading[51]:

$$\sigma^2 = \sigma_0^2 + 2Dt. \tag{1}$$

For each protein target, σ_0 is related to the injected peak width (dictated by microwell diameter), D is the in-gel diffusion coefficient, and t is the total elapsed time since protein injection. **Figure 3**a shows an example confocal fluorescence data X-Y slice image for OVA and associated _well_ design rule. Applying the analysis to the full protein ladder (**Figure 3**d), yields estimates of _well_, across a range of protein targets and diffusion coefficients ($D_{OVA} \sim 16$ µm^2/s, $D_{BSA} \sim 7$ µm^2/s, $D_{IgG} \sim 2.7$ µm^2/s calculated from linear fits to the plot of σ_{xy}^2 vs. diffusion time). Under the described conditions, the protein target with the largest D (OVA) suggests that a _well_ of 200 µm will satisfy the trade-off of maximizing separation lane density while minimizing separation lane overlap (7%T gels, 10 s protein PAGE). For comparison, top-down MALDI imaging mass spectrometry utilizes a protein spot pitch of 20-200 µm[24].

To further understand the diffusion-driven interdependency of the microwell spacing and separation performance, for the highest diffusivity ladder protein (OVA) we modelled the maximum assay time (the time at which protein signal is expected to bleed into the neighboring lane, from the diffusional peak spreading function above) for a range of microwell spacings (**Figure 3**e), as well as the R_S as a function of electrophoresis time and electric field strength (**Figure 3**f). The separation resolution R_S is modeled as[53]:

$$R_S = \frac{\Delta z}{\frac{1}{2}(4\sigma_1 + 4\sigma_2)} = \frac{\Delta\mu_{EP}Et}{\frac{1}{2}\left(4\sqrt{\sigma_0^2 + 2D_1 t} + 4\sqrt{\sigma_0^2 + 2D_2 t}\right)}, \tag{2}$$

where Δz is the difference in migration distance between the two protein targets, σ_1 and σ_2 are the Z-direction peak widths, $\Delta\mu_{EP}$ is the difference in electrophoretic mobility between the two targets, $\mathbf{E}$ is the electric field, and D_1 and D_2 are the diffusion coefficients for the two targets. Diffusion coefficients are provided in Table 1 of the Methods, with electrophoretic mobilities empirically determined in **Figure 2**d. We next defined a Péclet number as the ratio of the maximum assay time to the time required to reach R_S=1, with results presented in **Figure 3**g and the Péclet number given by:

$$Pe = \frac{t_{\text{band overlap}}}{t_{R_S=1}} = \frac{t_{\Delta\text{well}=6\sigma_{xy}}}{t_{R_S=1}}. \tag{3}$$

At $_{\text{well}}$ = 200 μm (**Figure 3**d), $Pe \sim 1$ for an applied electric field strength of 60 V/cm. As protein band diffusion measurements (**Figure 3**d) suggest measured diffusion coefficients smaller than predicted values, our Péclet analysis is a conservative estimate of the trade-off between separation performance and achievable microwell density. Separation resolution is proportional to electric field $\mathbf{E}$, thus, increasing $\mathbf{E}$ increases the Péclet number. $\mathbf{E}$ is equal to the voltage drop divided by the distance over which the voltage is dissipated. If the distance between electrodes is increased (e.g., by placing separation lanes in series between the electrodes, as configured for 2D immunoblotting[30]), higher driving voltages are required to reach the same $\mathbf{E}$ which can exceed power supply voltage limits. While we demonstrate electric fields of 43-68 V/cm in this work, future research regarding even higher $\mathbf{E}$ operating regimes (e.g., 100 V/cm using 30 V across 0.3 cm) would shed light on limitations arising from regime-relevant physics and chemistry (i.e., Joule heating, electrolysis). Joule heating and electrolysis both increase with electric current. Joule heating reduces separation resolution and introduces nonuniformities (via nonuniform heat dissipation)[53]. Electrolysis generates acid and base ions and creates bubbles that can modulate electrophoretic mobility and disrupt electric field[54] (e.g., pre-optimization projection electrophoresis system depicted in Supplementary Figure 1).

Building on an understanding of the dominant physics, namely diffusion, we next sought to investigate computational approaches to recover starting concentration distributions (here, the microwell array) from endpoint confocal fluorescence images of the protein PAGE (**Figure 3**h). Recovery of starting protein concentration distributions will both enhance separation lane density, and facilitate future reconstruction of complex distributions such as those expected in adherent cells and tissue slices. In microscopy, deconvolution of an experimentally, theoretically, or computationally-determined, microscope-dependent point spread function (psf) recovers spatial resolution by image postprocessing[55–57]. Inspired by deconvolution in microscopy, we explored whether we could represent the final protein projection image ($I(x,y,z,t)$) as the initial protein x-y pattern ($p(x,y,z)$; the spatial arrangement of cells/microwells) convolved with a 'diffusional point spread function' $\text{psf}_{\text{diff}}(x,y,z,t)$, in turn convolved with the imaging point spread function $\text{psf}_{\text{img}}(x,y,z,t)$:

$$I(x, y, z, t) = p_0(x, y, z) \otimes \text{psf}_{\text{diff}}(x, y, z, t)) \otimes \text{psf}_{\text{img}}(x, y, z, t). \tag{4}$$

We chose to describe the diffusional *psf* using 3D point-source diffusion[58]:

$$\text{psf}_{\text{diff}}(x,y,z,t)) = \frac{M}{(4\pi Dt)^{3/2}} \cdot \exp\left(-\left(\frac{x^2+y^2+z^2}{4Dt}\right)\right), \tag{5}$$

where D is again the protein diffusion coefficient, t the elapsed diffusion time, and M the starting number of molecules at the point source. Although we estimated the full 3D point spread function for each protein, we performed 2D deconvolution only on the individual slice images, without using information from neighboring focal planes (as in a "no-neighbors" deconvolution imaging method[59]). We used this approach to simplify processing, while recognizing that the simplification limits a full 3D reconstruction and the signal intensity improvement possible from 3D deconvolution. To perform 2D processing, we deconvolved the 2D function *psf*diff (through the centre of the point spread function, at Z=0) from 2D confocal slice images at the Z-direction migration peak for each protein (the Z position at which the summed intensity for that protein in the image field of view was maximized). We neglected effects of the imaging point spread function, as we expect that the resolution of our measurement is more limited by diffusion (tens of microns for our typical time scales, as shown in **Figure 3**a) than by the resolution of confocal microscopy with high NA objectives (typically sub-micron[60]).

After deconvolution of the protein PAGE images, we observe a considerable improvement in spatial resolution of XY profiles of separated BSA (**Figure 3**h; 5-15s elapsed PAGE duration in (i)-(iii)). Comparing the 'original' to the 'deconvolved' images illustrates that spatial resolution is improved from $\sigma_{xy} = 16\pm2$ μm to $\sigma_{xy} = 8.4\pm0.2$ μm (47%) for 5s electrophoresis (15s total time until photocapture), $\sigma_{xy} = 25.7\pm0.6$ μm to $\sigma_{xy} = 13.1\pm0.6$ μm (49%) for 10s electrophoresis (20s total time), and $\sigma_{xy} = 26.3\pm0.6$ μm to $\sigma_{xy} = 13.3\pm0.5$ (49%) for 15s electrophoresis (26s total time). Further, the localization of the peak centre was unperturbed by reconstruction ($\Delta\mu < 1.1$ μm for all analyzed protein spots, with $\Delta\mu_{\text{avg}} = 0.38$ μm) and the integrated fluorescence signal of each protein sample is minimally perturbed by the reconstruction except when visible artefacts were present in the deconvolved images as shown in the lowest electrophoresis time (i) (average AUCs after postprocessing are within 2.5% of the initial values in (ii-iii), but 24% in (i)). Measured errors in peak center were $\Delta\mu=0.08\pm0.06$ μm (t_{diff}=15s), $\Delta\mu=0.68\pm0.3$ μm (t_{diff}=20s), $\Delta\mu=0.1\pm0.2$ μm (t_{diff}=26s); measured errors in peak AUCs were ΔAUC=23.9$\pm$1.4% (t_{diff}=15s), ΔAUC=0.5$\pm$0.8% (t_{diff}=20s), ΔAUC=3$\pm$2% (t_{diff}=26s) (n=9 ROIs). Under ideal conditions, physics-based postprocessing is expected to report a time-invariant σ_{xy}. We do observe a weak dependence of σ_{xy} on time, which we attribute to estimated model parameters (including diffusion coefficient, in-gel temperature, hydrodynamic radius, gel density, and diffusion time) and depth-dependent imaging artefacts arising from refractive index mismatch between the separation gel and immersion medium (*psf*img was neglected in our analysis). Future study will benefit from refinement of the model; however, the physics-based image postprocessing introduced here offers a means to reconstruct a map of the initial sample specimen from the target concentration distributions in the 3D gel volume, all based on the endpoint fluorescence readout of protein PAGE.

Sample preparation design for single-cell projection electrophoresis. Having considered design of the projection electrophoresis device and assay using a well-characterized protein ladder, we next sought to identify factors important to high-performance protein PAGE of single cells (**Figure 4**). We first assessed settling of single BT474 cells in 25 μm diameter microwells within

the projection electrophoresis gels. **Figure 4**a depicts settled Calcein-stained BT474 breast tumour cells in microwells after gravitational settling and convective wash-off of cells settled outside of microwells. A corresponding full-gel wide-field microscopy image of immunoprobed GAPDH fluorescence after the projection electrophoresis assay is also shown; probed protein bands correlate with settled cell positions. Cell settling efficiencies (populated microwells) were at 43±8% with the number of settled single cells 356±82 per 9x9 mm projection electrophoresis device (n=5 devices). The fraction of microwells occupied by more than one cells was 10±3%. Further optimization of cell settling densities, microwell geometries, settling times, and wash parameters would likely improve these values and thus assay throughput.

After protein solubilization, diffusion-driven dilution of single-cell lysate occurs rapidly in the open microwell geometries. To determine how the concentration of the single-cell protein lysate changes during the lysis and electrophoresis stages of the assay, we used a combination of finite-element modelling (geometries shown in **Figure 4**b) and experimental monitoring of turboGFP-expressing U251 cells during cell lysis (**Figure 4**c) and finite-element modelling during electrophoresis (**Figure 4**d). To compare simulation and experiment, we integrated the 3D protein concentrations over the full Z range of the model to mimic detected wide-field fluorescence intensities (**Figure 4**e-f). Using this metric, after a typical 25s lysis time, we measure 17%±11% of the initial protein intensity. Our simulated profiles overestimate the diffusional dilution of protein, predicting only 2.2% of the initial intensity for in-well lysis after 25s. We attribute the ~15% discrepancy to a possible diffusion barrier on the microwell wall surface, arising from either the presence of Rhinohide® in the gel matrix, or the presence of residual GelSlick® or dichlorodimethylsilane used during gel fabrication. One important consideration for projection electrophoresis is that, in contrast to 2D single-cell immunoblots[20,30,33,34,36,61–65], there is reduced protein 'loss' in in the projection electrophoresis platform – primarily dilution. While other electrophoretic cytometry assays have a fluid layer or lid gel above the thin separation gel, into which protein can diffuse and is lost, in the projection electrophoresis device most (if not all) protein is mobilized into the bulk of the 3D gel when an electric field is applied to initiate PAGE.
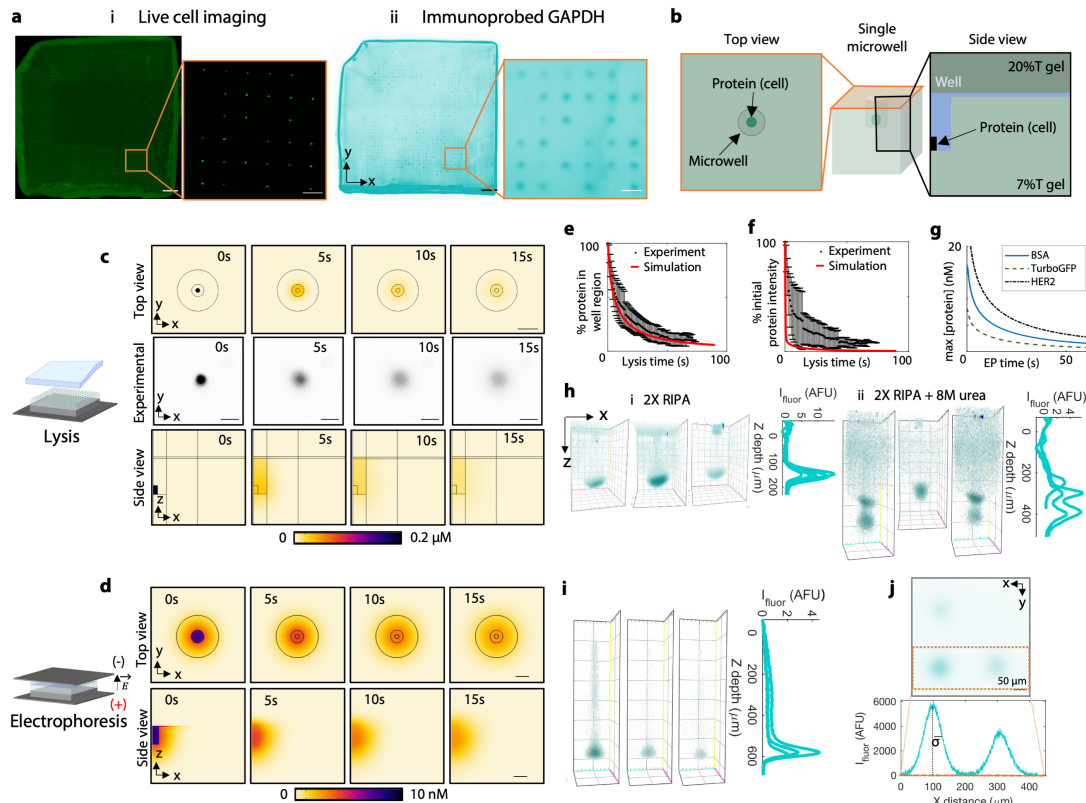
Figure 4. Design and verification of sample preparation for projection electrophoresis of single mammalian cells. (**a**) High-density endogenous protein bands (ii) correspond to single-cell settling in microwells (i). Scale bars represent 1 mm (left full-gel images) and 200 μm (right zoom images). (**b**) Illustration of top-view and side-view geometries shown in protein dilution studies (c-d). (**c**) Modelling and experimental quantification of diffusional dilution during lysis. Simulated and experimental top-view images of diffusional protein dilution during lysis, and side-view simulated results are shown. Simulated initial TurboGFP concentration was 2 μM. Experimental image is representative of 12 monitored cells across 3 independent lysis experiments. Scale bars represent 50 μm. (**d**) Modelling the impact of diffusion during electrophoresis on detectable in-gel protein concentration. Side and top view TurboGFP concentration profiles are shown at different times during electrophoresis. Simulated initial TurboGFP concentration (before lysis and electrophoresis) was 2 μM. Scale bars represent 30 μm. (**e**) Quantification of the percent of protein remaining in the microwell region during lysis (experiment plots mean and standard deviation of N=12 cells across 3 lysis experiments). (**f**) Quantification of the change in the spatial maximum protein concentration as a function of time after protein solubilization (experiment plots mean and standard deviation of N=12 cells across 3 lysis experiments). (**g**) Simulated maximum protein concentration vs. electrophoresis time, for 3 model proteins. (**h**) Representative beta tubulin separations from U251 glioblastoma cells lysed with different buffer formulations (2X RIPA lysis buffer and 2X RIPA including 8M urea), both after 10s electrophoresis. Lysis/EP buffer requires 8M urea for fast protein solubilization and electromigration. (**i**) Maximum intensity projection 3D renderings and Z-intensity profiles of probed GAPDH bands from single BT474 breast tumour cells. (**j**) Microwell packing density (impacting assay throughput) is dependent on protein band diffusion before photocapture. Protein diffusion profiles confirm that a microwell pitch of 200 μm is sufficient to resolve bands from neighboring microwells. After 10s EP, the mean peak width (σ) of the X-Y GAPDH spots is 32±11 μm (mean ± standard deviation of N=47 single-cell separation lanes across 5 replicate separation gels). Depicted confocal slice micrograph is

68

representative of 20 confocal image stacks, across different regions of 5 replicate separation gels. At a microwell pitch of 192 μm (3σ), <0.3% of the signal should bleed into the neighboring lane. Scale bar represents 50 μm.

We then sought to quantify how the maximum protein concentration changes during the analytical single-cell PAGE stage (**Figure 4**g) using finite-element modelling. From an initial protein concentration of 2 μM in a cylinder representing the cell, we estimate maximum protein concentrations of 2.1 nM (turboGFP, 26 kDa), 4.0 nM (BSA, 66.5 kDa), and 6.8 nM (HER2, 185 kDa) after 25s lysis and 20s electrophoresis in **Figure 4**g. We compared the expected diffusional dilution during electrophoresis to that expected in a planar system (Supplementary Figure 2) and found similar dilution during the assay steps in both systems. We note that the planar system is amenable to imaging during electrophoresis, thus our comparison (which predicts similar losses to those reported in our previous work[53]) serves as validation of the numerical model. Diffusional dilution of protein is dependent on both analyte size and gel density. The relatively large-pore-size gels used in this work (7%T) are optimal for large analytes (80-200 kDa), with adaptation for smaller analytes accommodated by moving to higher-density (smaller pore size) separation gels.

In optimizing the projection assay, we sought buffer chemistries to minimize lysis and solubilization times and used diffusive immunoprobing of model proteins β-tubulin and GAPDH using immunoglobulin fragments (F(ab) fragments) to assess solubilization efficacy. Here, we assessed a range of cell lysis and protein solubilization chemistries (**Figure 4**h). Across a range of chemistries, we observed differences in protein electromigration and dispersion, which were dependent on buffer composition and delivery methods. We selected a dual-function lysis and solubilization buffer that utilizes the anionic detergents sodium dodecyl sulphate (SDS) and sodium deoxycholate, augmented with a strong chaotrope (8M urea). Comparing solubilization, electromigration, and dispersion of the model protein β-tubulin from U251 glioblastoma cells lysed both without (i) and with (ii) 8M urea in the lysis buffer, we observed rapid electromigration into the 3D gel from the microwell and lower protein peak dispersion with urea present. Without urea, the 3D protein bands exhibited a hollow, bowl-like shape (concave towards the microwell), rather than the 3D Gaussian distribution which would be expected from diffusion theory. In a sub-set of separation lanes, two β-tubulin peaks were detectable after solubilization with urea lysis buffer (**Figure 4**h), suggesting delayed solubilization for a subset of the β-tubulin molecules, as might be expected depending on the intracellular state of the β-tubulin.

In formulating design guidelines for the dual-function lysis-electrophoresis buffer, we consider two additional points. First, detergents such as SDS and Triton X-100 form micelles of size on the order of nanometers[66,67]. Consequently, we explored the corollary hypothesis that size-exclusion partitioning[68,69] of solutes hinders delivery of lysis reagents from PAG matrices. As PAG density negatively correlates with in-gel concentration of size-excluded species[68], we explored whether lower density (6%T vs. 20%T) polyacrylamide lysis gels may facilitate improved protein solubilization. By moving to 6%T lysis gels, we observed higher apparent GAPDH mobility ($1.08\pm0.03\times10^{-4}$ cm^2/V·s using 6%T lysis gel, compared with $0.83\pm0.08\times10^{-4}$ cm^2/V·s using 20%T lysis gel, n=12-14 separation lanes) and potential reduction in protein band dispersion (Supplementary Figure 3). Second, strong chaotropes like urea solubilize proteins by disrupting hydrogen bonds as well as electrostatic and hydrophobic interactions to unfold hydrophobic protein regions[70]. Urea-based lysis buffers can solubilize different subsets of the proteome, as

compared to RIPA-like buffers[71]. High concentrations of urea (e.g., 8 M) can break down detergent micelles and disturb detergent-protein complexes[72,73]. Urea, as a small molecule, is less susceptible to size-exclusion partitioning from hydrogels. Just as in other protein separations, the ideal lysis buffer depends on the system and target of interest[70]. Analysis of another endogenous target protein, GAPDH, using the 8M urea lysis buffer that better solubilized beta tubulin also yielded protein peaks with low dispersion **(Figure 4**i).

Lastly, we verified the device design suggested by analysis of the well-characterized protein ladder now for the analysis of mammalian cells using the optimized cell preparation protocol (**Figure 4**j). We anticipated that the cell preparation may increase lysate diffusion from that assessed using the idealized protein ladder system in **Figure 3**, both because diffusion of protein targets in each single-cell lysate occurs during the time required for lysis and solubilization and because single-cell PAGE is run at higher temperature (37°C vs. 4°C) to improve protein solubilization. As discussed above, microwell spacing dictates the achievable sample multiplexing on one device. After 10s EP, we measured $\sigma = 32\pm13$ μm for GAPDH (36 kDa) in the X-Y plane. At $_{well} =$ 192 μm (6σ), we estimate that <0.3% of the fluorescent signal from the GAPDH in each cell lysate should bleed into the neighboring lane. Thus, $_{well} = 200$ μm is also sufficient to limit cross-contamination between adjacent separation lanes for GAPDH under these assay conditions.

Immunoblotting of protein targets from hundreds of single mammalian cells. We applied projection electrophoresis to immunoblotting analyses of well-characterized endogenous proteins GAPDH and actinin across populations of individual human BT474 breast cancer cells. As depicted in **Figure 5**, projection electrophoresis concurrently analyzes hundreds of single cells by parallelized separation after near-simultaneous lysis. To expedite full-gel volumetric fluorescence readout of protein immunoblots, we employed light sheet microscopy in **Figure 5**. Comparison measurements using scanning laser confocal microscopy are presented in Supplementary Figure 4. Data processing allows us to visualize immunoblot readouts as maximum intensity 3D renderings (**Figure 5**a), 2D contour plots showing X-Z fluorescence peaks for each fluorescence colour channel (corresponding to a target/antibody pair) (**Figure 5**b), and revolved 1D Z-directional fluorescence intensity plots (**Figure 5**c).

Cells lyse nearly simultaneously (**Figure 5**d). Across 4 replicate experiments, 31/36 monitored cells (86%) lysed within 5 s of placing the lysis gel on top of the microwell gel. Of the 5 remaining cells (all within the same replicate), 2 lysed during the 80 s monitoring period while 3 did not, potentially due to a bubble between the two gels. This near-simultaneous lysis, combined with parallelized electrophoretic separation over the full gel (>1000 separation lanes), facilitates concurrent analysis of hundreds of single cells. **Figure 5**e depicts revolved 1D intensity profiles for the 159 separation lanes within a single projection electrophoresis gel that passed R^2 (>0.7 for Gaussian fit to 1D Z-intensity profile) and SNR (>3) quality control in both protein channels (222 lanes passed these quality controls in the GAPDH channel; 204 lanes passed in the actinin channel). The intensity profiles show a GAPDH peak at a depth of 552 ± 54 μm and an actinin peak at a depth of 165 ± 42 μm (median $\pm$ one standard deviation). The profiles also show another peak in the actinin channel near the depth of the GAPDH peak, potentially due to off-target antibody binding and/or spectral bleed-through between the channels (optical filter sets) of the light sheet microscope.

Projection electrophoresis is compatible with multi-modal imaging of the intact cells before separation, as well as the separated protein bands after the assay. Pre-separation live-cell imaging of intact BT474 cells (**Figure 5**f-g) correlated well with detected probed bands. The *in situ* separations facilitated by projection electrophoresis allow comparison of live-cell fluorescence – prior to projection immunoblotting (via wide-field fluorescence microscopy in **Figure 5**f-g) – and endpoint probed GAPDH signal (via wide-field fluorescence microscopy in **Figure 5**h and light sheet microscopy in **Figure 5**i). The analysis revealed appreciable spatial correlation between live cell imaging prior to separation and wide-field fluorescence images of separated GAPDH (**Figure 5**j-k). Comparison shows 63-74% of detected live cells are correlated with GAPDH detection. In two duplicate separations, 76% and 63% of detected live cells corresponded to probed GAPDH bands, 24% and 37% of detected live cells did not correspond to a probed GAPDH band, and 17% and 22% of probed bands did not visibly correspond to a live cell. This correlation (and potentially cell settling efficiencies and analysis throughput) could potentially be further improved in future work by encapsulating settled cells in hydrogel to mitigate cell loss/movement during manual gel transfer and electrophoresis stack setup.

We observe the expected differential in electrophoretic mobility and nearly equivalent peak widths for the GAPDH (37 kDa) and actinin (100 kDa) targets for a total of 507 (GAPDH) and 303 (actinin) single-cell separations across duplicate separation gels (**Figure 5**l-m). In considering variation in electromigration, the coefficients of variation in electromigration are for GAPDH ~8.5% and for actinin ~27%. Qualitatively, we observe modestly higher electromigration on one side of the gel, on each of two gels (**Figure 5**n-o, Supplementary Figure 5), which is inconsistent with Joule heating-induced electromigration nonuniformity (e.g., higher mobility in the gel center, as observed in bulk separations[42]). Consequently, we attribute the modest, observed electromigration variation to nonuniformities in protein solubilization or electrophoresis (e.g., **E** and/or temperature), or to inaccuracies in gel surface detection (z = 0) during light sheet image analysis. Including a protein-sizing ladder in each separation lane enhances size-based protein identification, as our group has reported in similar 2D single-cell immunoblot devices (either as a ladder of well-defined, cell-endogenous proteins[33] or as ladder protein-conjugated beads[74]). Although from diffusion theory we would expect a larger peak width for the smaller protein target, differences in peak dispersion between targets can result in wider measured peak widths.
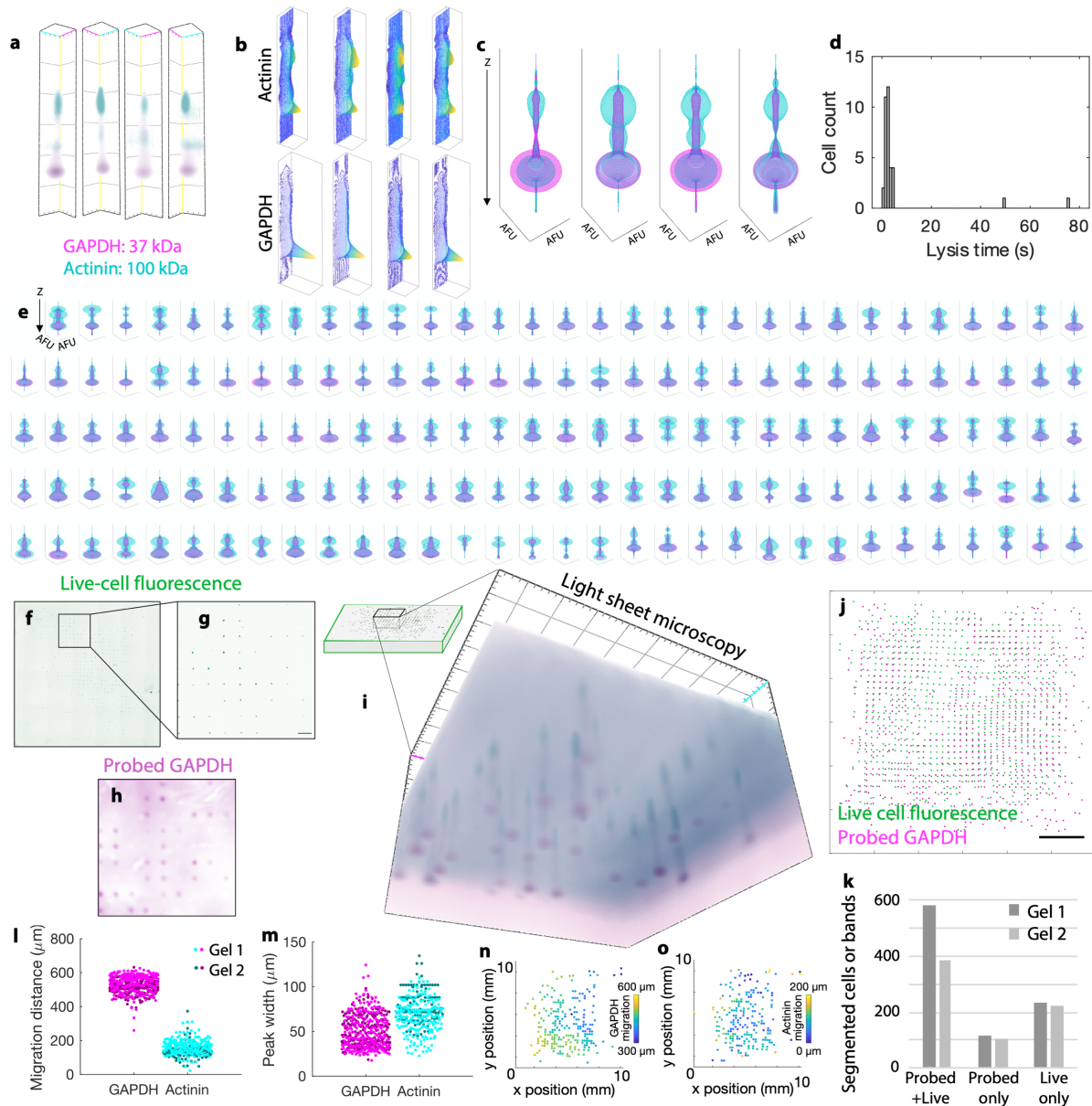
Figure 5. Projection electrophoresis permits simultaneous analysis of hundreds of single cells by concurrent separation after simultaneous lysis. **(a)** Maximum intensity projection 3D renderings of example separation lanes read out by tiled light sheet microscopy. **(b)** X-Z (Y-summed) contour plots of background-subtracted actinin and GAPDH protein signal within the lanes depicted in (a). **(c)** Revolved Z-intensity profiles (arbitrary fluorescence units, AFU, vs. Z) for the four separation lanes depicted in (a-b). Each plot depicts Z-directional intensity profiles (summed fluorescence within each X-Y ROI vs. Z) for GAPDH (magenta) and actinin (cyan), revolved around the Z-axis to generate 3D rendering of fluorescence distribution. **(d)** Histogram quantification shows 86% of U251 cells lyse within 5 s of initiating lysis. **(e)** Quantified fluorescence intensity data for n=159 separation lanes passing quality control for both the GAPDH and actinin channels. Each plot depicts revolved Z-intensity profiles. **(f)** Full-

72

gel wide-field fluorescence image of calcein-stained live BT474 breast tumour cells before analysis. **(g)** Subset of the live cells from (h), within a 1.75x1.75 mm light sheet microscopy field of view (scale bar depicts 200 µm). **(h)** Post-separation wide-field fluorescence image of probed GAPDH signal within the same field of view as (g). (f-h) are representative of N>3 separation gels. **(i)** Maximum intensity projection 3D rendering (representative of duplicate separation gels) of a light sheet microscopy image (same field of view as (g-h)), showing 3D separations of GAPDH and actinin from tens of separation lanes, each corresponding to signal from the settled cells in microwells depicted in (f-g). **(j)** Overlay image of segmented spots corresponding to live BT474 cells in microwells (green) and probed GAPDH bands after separation (magenta), for the same separation gel depicted in (f-i). **(k)** Quantification of correspondence between the segmented live cells and bands (via intensity thresholding) within the same separation lanes as (j). **(l)** Quantified migration distances from a total of n=507 (GAPDH) and n=303 (actinin) lanes passing quality control in two projection electrophoresis gels. **(m)** Quantified Z-direction peak widths for the same bands analyzed in (l). **(n-o)** Spatial map of the variation in GAPDH (n) and actinin (o) electromigration distances across the x-y gel area.

We compared scanning laser confocal microscopy (Supplementary Figure 4) and light sheet microscopy (**Figure 5**) imaging of the same gel devices to acquire volumetric protein immunoblot readouts from the protein PAGE separation lanes. Each imaging modality presents a trade-off in field of view and Z-axis resolution, but the imaging throughput of light sheet microscopy was >10X higher than scanning laser confocal, moving from ~120s/lane readout time down to ~8s/lane, while retaining sufficient Z-axis resolution to localize protein peaks. The laser scanning confocal imaging with 20X NA=1.0 water immersion objective (required for high-resolution optical sectioning) supported a 425 x 425 µm field of view, while light sheet microscopy with 5X detection objective (NA=0.16) provided a much larger 1.75 x 1.75 mm field of view. Because its optical sectioning is facilitated by the light sheet forming objectives forming a thin illumination sheet, light sheet microscopy allows the imaging optical section thickness to be decoupled from the detection objective NA, facilitating the use of lower NA detection objectives while maintaining optical sectioning[75]. The light sheet images acquired here had optical section thicknesses on the order of 10 µm, which should be sufficient to assess the diffusion-limited Z-directional peak widths of tens of microns for our separated protein bands.

Further, light sheet microscopy detected both protein targets with similar expected differential electrophoretic velocity and comparable peak widths of the immunoprobed targets to those measured with confocal (Supplementary Figure 4). Differences may be partly attributed to the impact of slight refractive index mismatch between the hydrogel and water immersion media on apparent confocal Z-depths (Supplementary Note 1). With both readout modalities, we also observe the log-linear relationship between migration distance and molecular weight for endogenous targets that would be expected for a size-sieving separation (Supplementary Figure 6). Given similar results in detection, migration location, and peak width for the model endogenous protein targets, the substantially larger field of view of light sheet microscopy proved beneficial, allowing endpoint imaging and analysis of 10x larger number of immunoblots (imaged separation lanes passing quality control: n=22 with confocal; n=303 actinin and n=507 GAPDH with light sheet microscopy, over two separation gels).

The parallel cell analysis approach described here overcomes shortcomings of serial analysis of cells. Although synchronous cell lysis is also not instantaneous across cells (with biological variation in lysis time on the order of seconds[76]), serial interrogation of individual cells leads to asynchronous analysis with longer time delays between analysis of the first cell and last cell in a population. Considering one published example single-cell enzyme analysis separation, where individual cells are interrogated by a capillary sampler after cell lysis via a UV light pulse[17], we estimate a 104 minute delay between interrogation of the first cell and interrogation of the last cell (219 cells analyzed with an analysis throughput of 2.1 cells/min). In contrast, concurrent analysis of ~300 measurable separation lanes is completed with < 10 s delay between the first and last cell, assuming a small delay in cell lysis arising during the application of the lysis and solubilization buffer. Furthermore, projection electrophoresis uses a single SDS-PAGE sieving gel for hundreds of concurrent single-cell protein-sizing separations. In contrast, serial electrophoresis separations performed in capillaries or microchannels require periodic renewal of sieving matrix between separations to mitigate residual sample and matrix degradation[77]. Consequently, higher-throughput electrophoresis systems often use free solution[17] or sieving polymers[28]. By introducing a new, rapid, and parallelized electrophoresis approach, we demonstrate simultaneous single-cell separations of hundreds of single cells with an active assay time of 2.5 cells/s (from lysis through photocapture), depending on settling efficiency – this represents a >70-fold improvement in assay throughput over serial capillary systems.

Projection electrophoresis addresses key bottlenecks in single-cell protein analysis by achieving rapid (<1.5 min active assay time), synchronous size-based protein separation for hundreds of unfixed cells in parallel, without sample transfer steps that can result in sample losses and changes in sample composition. Detection specificity combines antibody recognition with size-separation to confer proteoform-level specificity even when specific probes do not exist, and avoids the need for pre-separation tagging of proteins for detection. *In situ* cell lysis, separation, and photocapture of protein to the gel matrix mitigates deleterious effects of sample transfer between systems, including losses from adsorption to glassware, potential sample contamination, and sample changes between lysis and separation. Effectively synchronous analysis of hundreds of cells in parallel mitigates artifactual changes in cell population heterogeneity induced by heterogeneous lysis times, while also facilitating high assay throughput. Using rapid whole-cell lysis of unfixed cells, we demonstrate detection of both nuclear and cytosolic proteins. We design and characterize the system by both modelling and measuring the results of microscale physics. Compared with planar (2D) single-cell western blotting, we demonstrate a 10-fold reduction in volume of cell suspension (and thus number of cells) settled to assay the same number of cells, and further throughput improvements may be possible by optimizing parameters for settling efficiency. While 2D devices are conducive to immunoprobing, imaging as readout, and efficient data analysis, projection electrophoresis increases the density of single-cell analyses for the same device footprint, by shifting the separation dimension to the Z-axis, while maintaining similar protein losses and outputting rich 3D information about protein band morphology and dispersion. Important beyond enhancing data density, 3D projection electrophoresis holds promise for future profiling of cellular 'connectomes' by supporting analyses of complex cellular networks such as intact tissue slices and adherent cells cultured on planar hydrogel surfaces[37]. Looking forward, the performance of projection electrophoresis can be improved in future work by moving to larger-area gels to further parallelize analysis, and by using our understanding of the driving small-scale physics to optimize gel materials for targets of interest and thus enable the use of even higher

microwell densities (or adherent cells) and improved separation performance. With a straightforward, open microfluidic format and advantages complementary to existing protein analysis tools, we anticipate that projection electrophoresis will assist in the development of proteoform-level atlases of single-cell diversity.

3.4 References

1. Berg, J., JL, T. & L., S. Chapter 3: Protein Structure and Function. in *Biochemistry*

2. Vogel, C. *et al.* Sequence signatures and mRNA concentration can explain two-thirds of protein abundance variation in a human cell line. *Mol. Syst. Biol.* **6**, 1–9 (2010).

3. Darmanis, S. *et al.* Simultaneous Multiplexed Measurement of RNA and Proteins in Single Cells. *Cell Rep.* **14**, 380–389 (2016).

4. Liu, Y., Beyer, A. & Aebersold, R. On the Dependency of Cellular Protein Levels on mRNA Abundance. *Cell* **165**, 535–550 (2016).

5. Gong, H. *et al.* Single-cell protein-mRNA correlation analysis enabled by multiplexed dual-analyte co-detection. *Sci. Rep.* **7**, 1–8 (2017).

6. Smith, L. M., Kelleher, N. L. & Consortium for Top Down, P. Proteoform: a single term describing protein complexity. *Nat Methods* **10**, 186–187 (2013).

7. Harper, S. J. & Bates, D. O. VEGF-A splicing: the key to anti-angiogenic therapeutics? *Nat. Rev. Cancer* **8**, 880–887 (2008).

8. Arribas, J., Baselga, J., Pedersen, K. & Parra-Palau, J. L. p95HER2 and breast cancer. *Cancer Res.* **71**, 1515–9 (2011).

9. Liu, Y., Chen, X., Zhang, Y. & Liu, J. Advancing single-cell proteomics and metabolomics with microfluidic technologies. *Analyst* **144**, 846–858 (2019).

10. Kennedy, R. T., Oates, M. D., Cooper, B. R., Nickerson, B. & Jorgenson, J. W. Microcolumn Separations and the Analysis of Single Cells. *Science (80-.).* **246**, 57–63 (1989).

11. L., N., T., W. & B.N., R. Practical issues in calculating the sample size for prevalence studies. *Arch. Orofac. Sci.* **1**, 9–14 (2006).

12. Spruessel, A. *et al.* Tissue ischemia time affects gene and protein expression patterns within minutes following surgical tumor excision. *Biotechniques* **36**, 1030–1037 (2004).

13. Lee, T. T. & Yeung, E. S. Quantitative determination of native proteins in individual human erythrocytes by capillary zone electrophoresis with laser-induced fluorescence detection. *Anal. Chem.* **64**, 3045–3051 (1992).

14. Olefirowicz, T. M. & Ewing, A. G. Dopamine concentration in the cytoplasmic compartment of single neurons determined by capillary electrophoresis. *J. Neurosci. Methods* **34**, 11–15 (1990).

15. Simpson, P. C. *et al.* High-throughput genetic analysis using microfabricated 96-sample capillary array electrophoresis microplates. *Proc. Natl. Acad. Sci.* **95**, 2256–2261 (1998).

16. Rogers, B., Gibson, G. T. T. & Oleschuk, R. D. Bundled capillary electrophoresis using microstructured fibres. *Electrophoresis* **32**, 223–229 (2011).

17. Dickinson, A. J., Armistead, P. M. & Allbritton, N. L. Automated capillary electrophoresis system for fast single-cell analysis. *Anal. Chem.* **85**, 4797–4804 (2013).

18. Hargis, A. D., Alarie, J. P. & Ramsey, J. M. Characterization of cell lysis events on a

microfluidic device for high-throughput single cell analysis. *Electrophoresis* **32**, 3172–9 (2011).

19. Wheeler, A. R. *et al.* Microfluidic Device for Single-Cell Analysis. *Anal. Chem.* **75**, 3581–3586 (2003).

20. Sinkala, E. *et al.* Profiling protein expression in circulating tumour cells using microfluidic western blotting. *Nat. Commun.* **8**, 14622 (2017).

21. Budnik, B., Levy, E., Harmange, G. & Slavov, N. SCoPE-MS: mass spectrometry of single mammalian cells quantifies proteome heterogeneity during cell differentiation. *Genome Biol.* **19**, 161 (2018).

22. Zhu, Y. *et al.* Proteomic Analysis of Single Mammalian Cells Enabled by Microfluidic Nanodroplet Sample Preparation and Ultrasensitive NanoLC-MS. *Angew. Chem. Int. Ed. Engl.* 1–6 (2018). doi:10.1002/anie.201802843

23. van Remoortere, A. *et al.* MALDI imaging and profiling MS of higher mass proteins from tissue. *J. Am. Soc. Mass Spectrom.* **21**, 1922–1929 (2010).

24. Aichler, M. & Walch, A. MALDI Imaging mass spectrometry: current frontiers and perspectives in pathology research and practice. *Lab Invest* **95**, 422–431 (2015).

25. Do, T. D. *et al.* Optically Guided Single Cell Mass Spectrometry of Rat Dorsal Root Ganglia to Profile Lipids, Peptides and Proteins. *ChemPhysChem* **19**, 1180–1191 (2018).

26. Burnette ', W. N. " Western Blotting " : Electrophoretic Transfer of Proteins from Sodium Dodecyl Sulfate-Polyacrylamide Gels to Unmodified Nitrocellulose and Radiographic Detection with Antibody and Radioiodinated Protein A. *Anal. Biochem.* **112**, 195–203 (1981).

27. Towbin, H., Staehelin, T. & Gordon, J. Electrophoretic transfer of proteins from polyacrylamide gels to nitrocellulose sheets: procedure and some applications. *Proc. Natl. Acad. Sci.* **76**, 4350–4354 (1979).

28. Jin, S. *et al.* Multiplexed Western Blotting Using Microchip Electrophoresis. *Anal. Chem.* **88**, 6703–10 (2016).

29. Wood, D. K., Weingeist, D. M., Bhatia, S. N. & Engelward, B. P. Single cell trapping and DNA damage analysis using microwell arrays. *Proc Natl Acad Sci U S A* **107**, 10008–10013 (2010).

30. Hughes, A. J. *et al.* Single-cell western blotting. *Nat. Methods* **11**, 749–55 (2014).

31. Sinkala, E. *et al.* Profiling protein expression in circulating tumour cells using microfluidic western blotting. *Nat. Commun.* **8**, 14622 (2017).

32. Rosàs-Canyelles, E., Dai, T., Li, S. & Herr, A. E. Mouse-to-mouse variation in maturation heterogeneity of smooth muscle cells. *Lab Chip* **18**, 1875–1883 (2018).

33. Kang, C.-C. *et al.* Electrophoretic cytopathology resolves ERBB2 forms with single-cell resolution. *npj Precis. Oncol.* **2**, 10 (2018).

34. Yamauchi, K. A. & Herr, A. E. Subcellular western blotting of single cells. *Microsystems Nanoeng.* **3**, 16079 (2017).

35. Tentori, A. M., Yamauchi, K. A. & Herr, A. E. Detection of Isoforms Differing by a

Single Charge Unit in Individual Cells. *Angew. Chemie* **128**, 12619–12623 (2016).

36. Yamauchi, K. A., Tentori, A. M. & Herr, A. E. Arrayed isoelectric focusing using photopatterned multi-domain hydrogels. 16–18 (2018). doi:10.1002/elps.201700386

37. Zhang, Y., Naguro, I. & Herr, A. E. In Situ Single-Cell Western Blot on Adherent Cell Culture. *Angew. Chemie - Int. Ed.* **58**, 13929–13934 (2019).

38. Lin, J.-M. G. *et al.* Linking invasive motility to protein expression in single tumor cells. *Lab Chip* **18**, 371–384 (2018).

39. Tillberg, P. W. Expansion Microscopy : Improving Imaging Through Uniform Tissue Expansion. (Massachusetts Institute of Technology, 2016).

40. Tomer, R., Ye, L., Hsueh, B. & Deisseroth, K. Advanced CLARITY for rapid and high-resolution imaging of intact tissues. (2014). doi:10.1038/nprot.2014.123

41. Burnette, W. N. 'Western blotting': Electrophoretic Transfer of Proteins from Sodium Dodecyl Sulfate-Polyacrylamide Gels to Unmodified Nitrocellulose and Radiographic Detection with Antibody and Radioiodinated Protein A. *Anal. Biochem.* **112**, 195–203 (1981).

42. Ventzki, R. & Stegemann, J. High-throughput separation of DNA and proteins by three-dimensional geometry gel electrophoresis: Feasibility studies. *Electrophoresis* **24**, 4153–4160 (2003).

43. Englert, C. R., Baibakov, G. V & Emmert-buck, M. R. Layered Expression Scanning : Rapid Molecular Profiling of Tumor Samples Advances in Brief Layered Expression Scanning : Rapid Molecular Profiling of Tumor Samples. 1526–1530 (2000).

44. Zhu, L., Tangrea, M. A., Mukherjee, S. & Emmert-Buck, M. R. Layered electrophoretic transfer - A method for pre-analytic processing of histological sections. *Proteomics* **11**, 883–889 (2011).

45. Hughes, A. J., Lin, R. K. C., Peehl, D. M. & Herr, A. E. Microfluidic integration for automated targeted proteomic assays. *Proc. Natl. Acad. Sci. U. S. A.* **109**, 5972–7 (2012).

46. Ferguson, K. A. Starch-gel electrophoresis—Application to the classification of pituitary proteins and polypeptides. *Metabolism.* **13**, 985–1002 (1964).

47. Properties, T. H. The Hydrodynamic Properties of Bovine Serum Albumin Monomer and Dimer *. **7**, 4261–4272

48. Mary, T. & Basrett, I. By THEODORE PETERS, JR. The Mary Imogene Basrett Horpital, Cooperrtown, New. **37**, (1985).

49. Sah, H. Stabilization of proteins against methylene chloride / water interface- induced denaturation and aggregation. **58**, 143–151 (1999).

50. Oliva, A. & Farin, B. Comparative study of protein molecular weights by size-exclusion chromatography and laser-light scattering. **25**, 833–841 (2001).

51. Miller, C. C. The Stokes-Einstein Law for Diffusion in Solution. *Prod. Roy. Soc. Lond.* **106**, 724–749 (1924).

52. Park, I. H., Johnson, C. S. & Gabriel, D. A. Probe Diffusion in Polyacrylamide Gels as Observed by Means of Holographic Relaxation Methods: Search for a Universal Equation.

Macromolecules **23**, 1548–1553 (1990).

53. Vlassakis, J. & Herr, A. E. Joule Heating-Induced Dispersion in Open Microfluidic Electrophoretic Cytometry. *Anal. Chem.* acs.analchem.7b03096 (2017). doi:10.1021/acs.analchem.7b03096

54. Macounová, K., Cabrera, C. R., Holl, M. R. & Yager, P. Generation of natural pH gradients in microfluidic channels for use in isoelectric focusing. *Anal. Chem.* **72**, 3745–3751 (2000).

55. Sarder, P. & Nehorai, A. Deconvolution methods for 3-D fluorescence microscopy images. *IEEE Signal Process. Mag.* **23**, 32–45 (2006).

56. Sibarita, J. B. Deconvolution microscopy. *Adv. Biochem. Eng. Biotechnol.* **95**, 201–243 (2005).

57. McNally, J. G., Karpova, T., Cooper, J. & Conchello, J. A. Three-Dimensional Imaging by Deconvolution Microscopy. *Methods* **19**, 373–385 (1999).

58. Pattle, R. E. Diffusion From an Instantaneous Point Source With Concentration Dependent Coefficient. *Quart. J. Mech. Appl. Math.* **12**, 407–409 (1959).

59. Monck, J. R., Oberhauser, A. F., Keating, T. J. & Fernandez, J. M. Thin-section ratiometric Ca2+ images obtained by optical sectioning of fura-2 loaded mast cells. *J. Cell Biol.* **116**, 745–759 (1992).

60. Pawley, J. B. *Biological Confocal Microscopy*. (2006).

61. Duncombe, T. A. *et al.* Hydrogel Pore-Size Modulation for Enhanced Single-Cell Western Blotting. *Adv Mater* **28**, 327–334 (2016).

62. Kang, C.-C. C. *et al.* Single cell-resolution western blotting. *Nat Protoc* **11**, 1508–1530 (2016).

63. Kang, C.-C. C., Lin, J.-M. G. M., Xu, Z., Kumar, S. & Herr, A. E. Single-cell Western blotting after whole-cell imaging to assess cancer chemotherapeutic response. *Anal Chem* **86**, 10429–10436 (2014).

64. Tentori, A. M., Yamauchi, K. A. & Herr, A. E. Detection of Isoforms Differing by a Single Charge Unit in Individual Cells. *Angew Chem Int Ed Engl* **55**, 12431–12435 (2016).

65. Su, E. J. & Herr, A. E. Electrophoretic cytometry of adherent cells. *Lab Chip* **17**, 4312–4323 (2017).

66. Duplâtre, G., Ferreira Marques, M. F. & Da Graça Miguel, M. Size of sodium dodecyl sulfate micelles in aqueous solutions as studied by positron annihilation lifetime spectroscopy. *J. Phys. Chem.* **100**, 16608–16612 (1996).

67. Stetsenko, A. & Guskov, A. An overview of the top ten detergents used for membrane protein crystallization. *Crystals* **7**, (2017).

68. Tong, J. & Anderson, J. L. Partitioning and diffusion of proteins and linear polymers in polyacrylamide gels. *Biophys. J.* **70**, 1505–1513 (1996).

69. Su, A., Smith, B. E. & Herr, A. E. In Situ Measurement of Thermodynamic Partitioning in Open Hydrogels. *Anal. Chem.* **92**, 875–883 (2019).
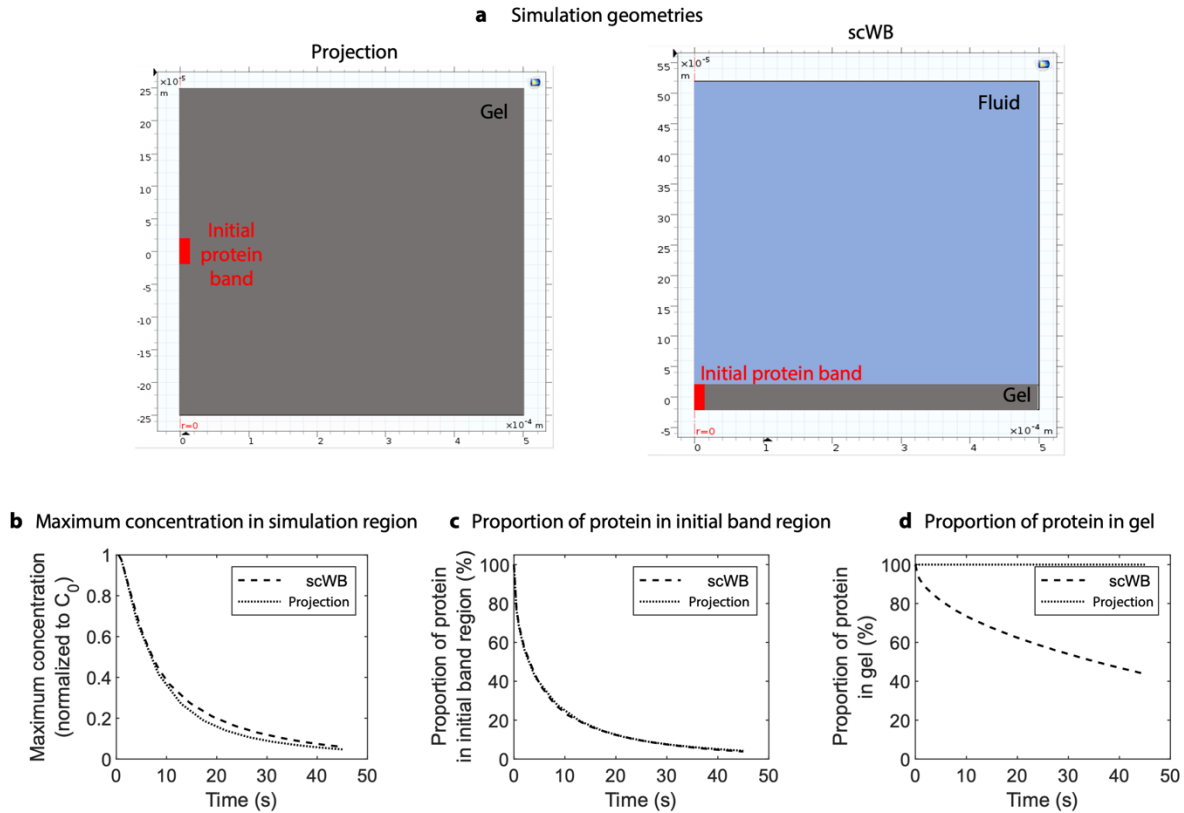
70.   Rabilloud, T. Solubilization of proteins for electrophoretic analyses. *Electrophoresis* **17**, 813–829 (1996).

71.   Ngoka, L. C. M. Sample prep for proteomics of breast cancer: Proteomics and gene ontology reveal dramatic differences in protein solubilization preferences of radioimmunoprecipitation assay and urea lysis buffers. *Proteome Sci.* **6**, 1–24 (2008).

72.   Wiśniewski, J. R., Zougman, A., Nagaraj, N. & Mann, M. Universal sample preparation method for proteome analysis. *Nat. Methods* **6**, 359–362 (2009).

73.   Glatter, T., Ahrné, E. & Schmidt, A. Comparison of different sample preparation protocols reveals lysis buffer-specific extraction biases in gram-negative bacteria and human cells. *J. Proteome Res.* **14**, 4472–4485 (2015).

74.   Kim, J. J., Chan, P. P. Y., Vlassakis, J., Geldert, A. & Herr, A. E. Microparticle Delivery of Protein Markers for Single-Cell Western Blotting from Microwells. *Small* **1802865**, 1–11 (2018).

75.   Huisken, J., Swoger, J., Del Bene, F., Wittbrodt, J. & Stelzer, E. H. K. Optical sectioning deep inside live embryos by selective plane illumination microscopy. *Science (80-.).* **305**, 1007–1009 (2004).

76.   Brown, R. B. & Audet, J. Current techniques for single-cell lysis. *J. R. Soc. Interface* **5**, (2008).

77.   Luo, S., Feng, J. & Pang, H. M. High-throughput protein analysis by multiplexed sodium dodecyl sulfate capillary gel electrophoresis with UV absorption detection. *J. Chromatogr. A* **1051**, 131–134 (2004).

78.   Gumuscu, B. & Herr, A. E. Separation-encoded microparticles for single-cell western blotting. *Lab Chip* **Advance**, (2020).

79.   Schindelin, J. *et al.* Fiji : an open-source platform for biological-image analysis. **9**, 676–682 (2012).

80.   Schneider, C. A., Rasband, W. S. & Eliceiri, K. W. NIH Image to ImageJ: 25 years of image analysis. *Nat. Methods* **9**, 671–675 (2012).

81.   Linkert, M. *et al.* Metadata matters: Access to image data in the real world. *J. Cell Biol.* **189**, 777–782 (2010).

82.   Crocker, J. C. & Grier, D. G. Methods of Digital Video Microscopy for Colloidal Studies. *J. Colloid Interface Sci.* **179**, 298–310 (1996).

83.   Blair, D. & Dufresne, E. The Matlab Particle Tracking Code Repository. (2008).

84.   Wilkins, D. K. *et al.* Hydrodynamic radii of native and denatured proteins measured by pulse field gradient NMR techniques. *Biochemistry* **38**, 16424–16431 (1999).

85.   A.G., O., Preston, B. N. & Wells, J. D. On the transport of compact particles through solutions of chain-polymers. *Proc. R. Soc. London* **333**, 297–316 (1973).

86.   Baselga, J., Hernández-Fuentes, I., Masegosa, R. M. & Llorente, M. A. Effect of Crosslinker on Swelling and Thermodynamic Properties of Polyacrylamide Gels. *Polymer Journal* **21**, 467–474 (1989).

87.   Liu, C. H. *et al.* Enhanced cell viability and cell adhesion using low conductivity medium

for negative dielectrophoretic cell patterning. *Biotechnol. J.* **5**, 1005–1015 (2010).

3.5 Supplemental Information
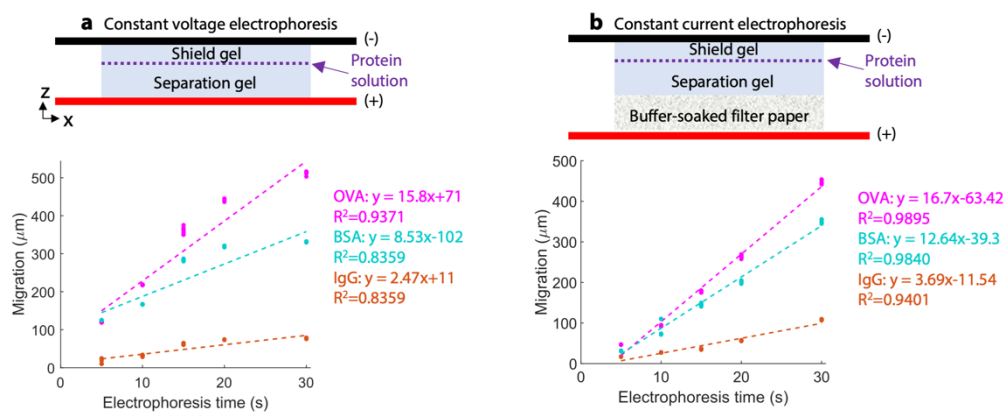
Supplementary Figure 1. Optimization of Z-directional electrophoresis system to facilitate constant-velocity migration. **(a)** Shows a cross-sectional view of the setup before optimization. The separation gel is in direct contact with the anode, and the electric field was supplied as constant voltage. Linear fits to the migration data are poor, with migration slowing at increasing electrophoresis times. **(b)** Depicts the system after optimization. A buffer-soaked filter paper is placed between the separation gel and the anode to mitigate pH changes due to electrolysis at the electrode surface, and the electric field was supplied as constant current. Linear fits to the migration data are improved.

a Simulation geometries

Projection

scWB

**b** Maximum concentration in simulation region **c** Proportion of protein in initial band region **d** Proportion of protein in gel

Supplementary Figure 2. Comparison of simulated in-gel protein dilution during electrophoresis for standard single-cell western blotting and Z-direction electrophoresis. **(a)** 2D axisymmetric simulation geometries. **(b)** Comparison of maximum concentration in the simulation region, normalized to the initial concentration in the protein band (C_0). **(c)** Proportion of the protein in the initial simulation band region. **(d)** Proportion of protein retained in the gel.

a GAPDH: 20%T lysis gel **b** GAPDH: 6%T lysis gel
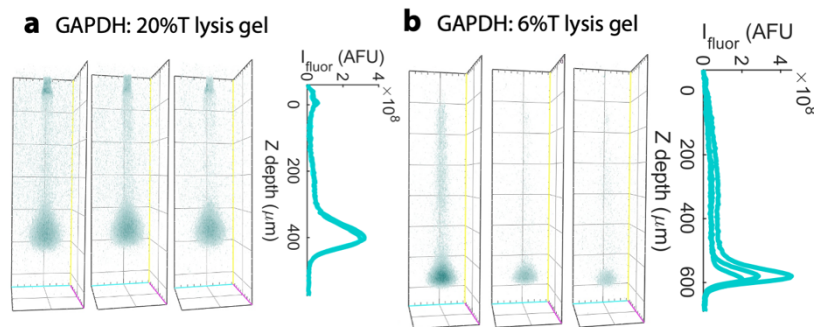
Supplementary Figure 3. Representative 3D renderings (left) and summed fluorescence Z-intensity profiles (right) of GAPDH separations from BT474 breast tumour cells after lysis using **(a)** a 20%T lysis gel, and **(b)** a 6%T lysis gel, both using 2X RIPA + 8M urea lysis buffer and after 10s electrophoresis. By moving to 6%T lysis gels, we observed higher apparent GAPDH mobility ($1.08\pm0.03\times10^{-4}$ cm^2/V·s using 6%T lysis gel, compared with $0.83\pm0.08\times10^{-4}$ cm^2/V·s using 20%T lysis gel, n=12-14 separation lanes) and potential reduction in dispersion of the protein band towards the microwell.
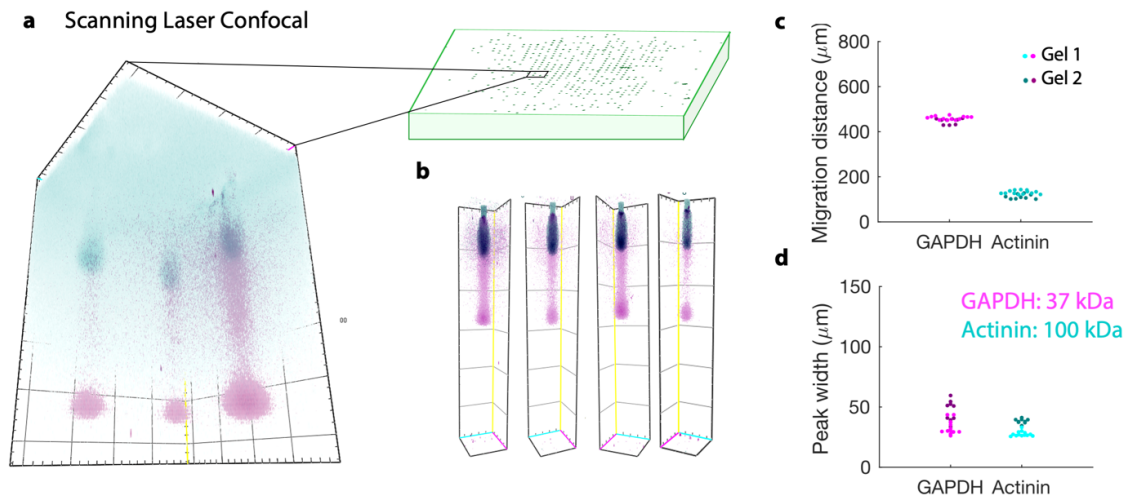
Supplementary Figure 4. Comparison imaging by scanning laser confocal microscopy of the same projection electrophoresis separation gels analyzed in Figure 5. **(a)** a scanning laser confocal field of view compared to the size of the separation gel. **(b)** Representative individual separation lanes read out by scanning laser confocal microscopy. **(c)** quantification of migration distance for GAPDH (37 kDa) and actinin (100 kDa). **(d)** quantification of Z-directional peak width for the separated bands of the same protein targets. For (c-d), individual dots are plotted for two independent separation gels. Dots corresponding to n=13 (gel 1) and n=9 (gel 2) separation lanes are plotted.
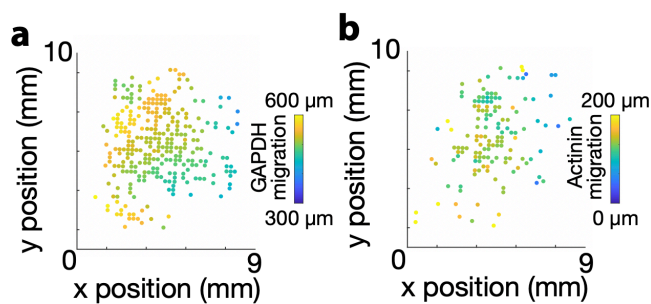
Supplementary Figure 5. Spatial map of the variation in **(a)** GAPDH and **(b)** actinin electromigration distances across the x-y gel area, for the duplicate separation gel (first gel is presented in Fig. 5n-o)
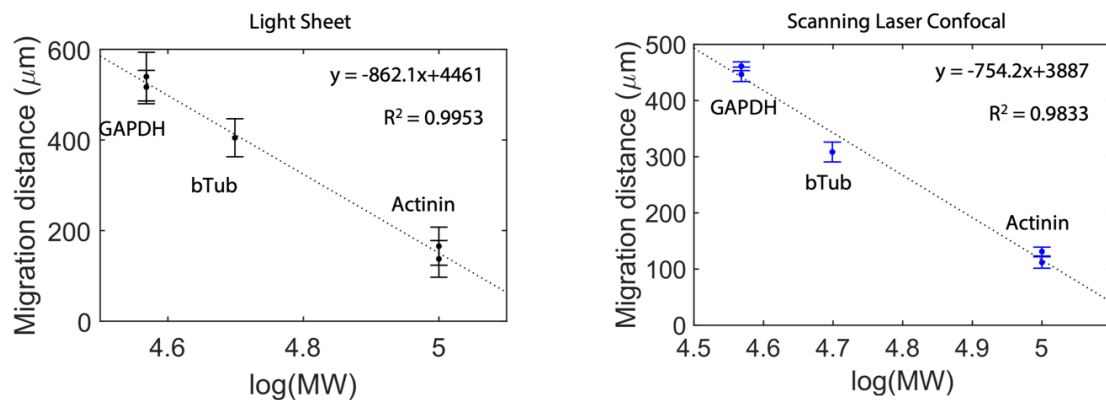
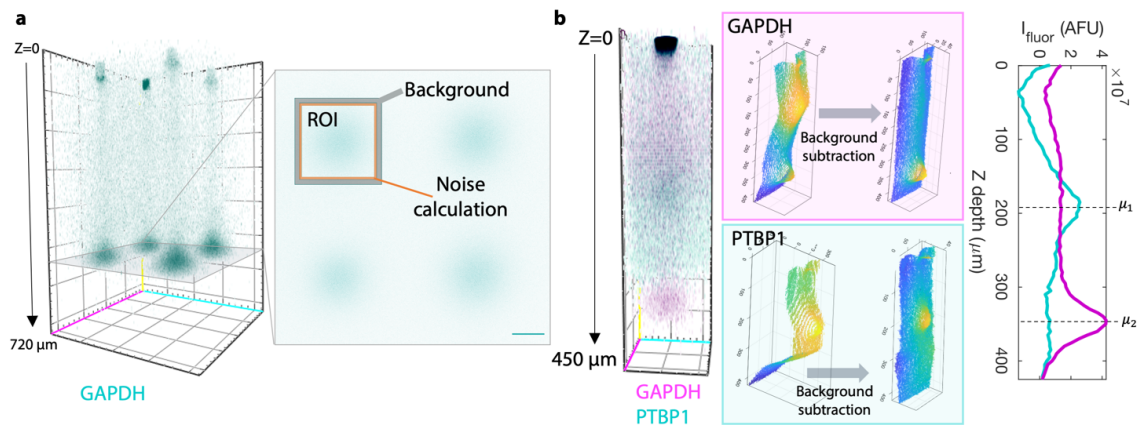**Supplementary Figure 6**. Quantification distance of migration distance vs. log(molecular weight) for three endogenous protein targets measured from single BT474 breast tumour cells using light sheet (left) and scanning laser confocal (right) microscopy readouts for the Projection Electrophoresis assay. Both readout methods show the expected log-linear relationship affirming size separation. Each point plots the mean and standard deviation of quantifiable separation lanes from a single separation gel (duplicate gels for GAPDH and actinin; a single gel for beta tubulin). For the light sheet analysis, 100-300 separation lines were quantified to yield each plotted point; for the scanning laser confocal analysis, 9-13 separation lanes were quantified to yield each plotted point. For this experiment, beta tubulin was electrophoretically probed with Ms anti-beta tubulin primary (GeneTex GTX11312, 1:15 dilution) and Dk anti-Ms AlexaFluor 647 secondary (Invitrogen A31571, lot 2045337, 1:10 dilution) antibodies.

a) Affix 1 mm spacers to silicon wafer with SU-8 micropost structures

b) Add acrylamide gel precursor to micropost structures

c) Place silanized glass slide on spacers, remove bubbles in precursor, and wait for chemical polymerization of polyacrylamide gel

d) Remove glass slide from wafer, demolding gel from mold

e) Use razor blade to trim excess gel and dice into freestanding gel pieces

f) Slide razor blade between glass and gel to release gels

Supplementary Figure 7. Substrate-free released gel fabrication process.

Supplementary Figure 8. Data processing for three-dimensional projection electrophoresis datasets from immunoprobed separations from single BT474 cells. **(a)** 3D data is composed of stacks of X-Y slice images. Each slice image is processed to isolate the region of interest ('ROI') for each separation lane, as well as small adjacent surrounding regions for background subtraction ('Background') and to calculate the noise of the background-subtracted signal ('Noise calculation'). Scale bar represents 450 μm. **(b)** The ROI corresponding to each separation lane is also a 3D dataset (rendering, left), which can be collapsed into a 2D (X-Z) image by summing in Y (middle), or collapsed into a summed 1D intensity profile by summing all pixels in X and Y within the ROI region (right). Subtraction of the average background region intensity at each Z-depth from each pixel in the ROI (middle column) isolates the signal from the single-cell separation, clearly showing separated, immunoprobed protein peaks corresponding to GAPDH (top) and PTBP1 (bottom). Gaussian fitting to the background subtracted 1D intensity profiles yields migration distance, peak width, and signal-to-noise ratio information for each separation lane.
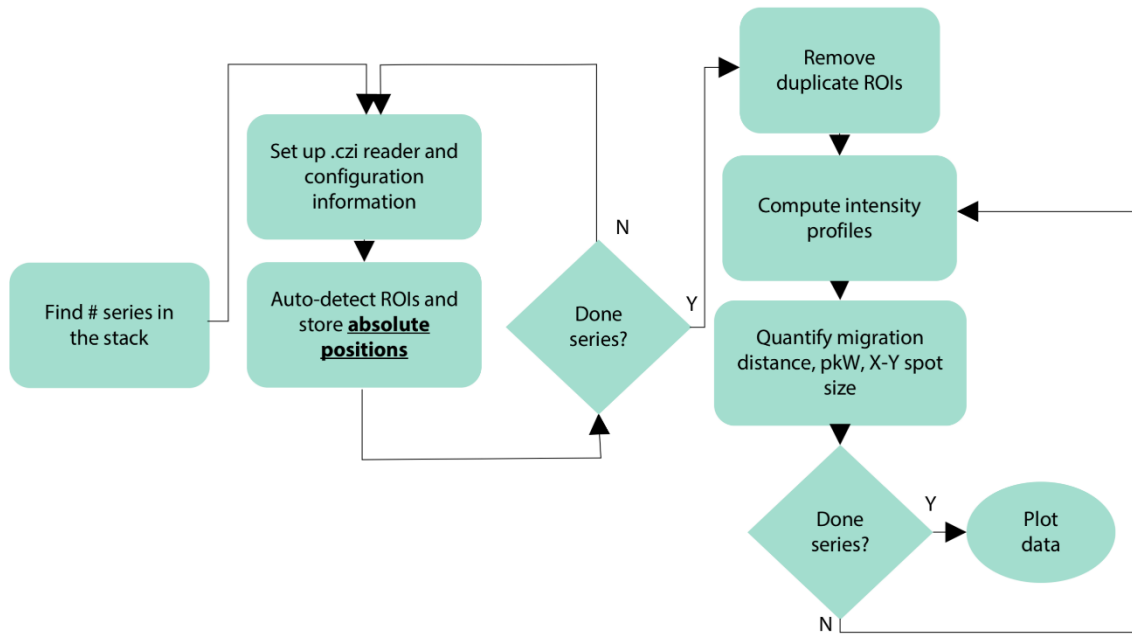
Supplementary Figure 9. Schematic diagram of image analysis software for tiled light sheet images.

Gel type (thickness)	Gel density	Stock acrylamide	Rhinohide	BPMA	Buffer	Initiator(s)	Polymerization time	Fabrication setup
Purified protein: separation (1 mm)	7%T or 10%T	30% (37.5:1) stock; final concentration 7% or 10% w/v Sigma-Aldrich: A3699	10% v/v final from stock	3 mM from 100 mM stock in DMSO	10% (v/v) final concentration 10X tris-glycine; stored in modified RIPA	0.08% APS (Sigma-Aldrich: A3678), 0.08% TEMED (Sigma-Aldrich: T9281)	60 mins	Methacrylate functionalized glass slide and silanized silicon wafer mould
Purified protein: shield (500 μm)	20%T	30% (37.5:1) stock; final concentration 20% w/v	10% v/v final from stock	none	10% (v/v) final concentration 10X tris-glycine; stored in run buffer	0.08% APS, 0.08% TEMED	60 mins	Gel Slick® (Lonza: 50640) treated glass plate and glass slide
Well gels for single cell separations and in-well lysis tests (1 mm)	7%T	30% (37.5:1) stock; final concentration 7% w/v	4.66% v/v final concentration from stock	3 mM from 100 mM stock in DMSO	10% (v/v) final concentration 10X tris-glycine; stored in PBS (lysis monitoring) or 1X tris-glycine (single cell separations)	0.08% APS, 0.08% TEMED	60 mins	Methacrylate functionalized glass slide and silanized silicon wafer mould
Lysis shield gels for in-well lysis tests (1 mm)	20%T	30% (37.5:1) stock; final concentration 20% w/v	10% v/v final from stock	none	None; stored in modified RIPA	0.08% APS, 0.08% TEMED	60 mins	Gel Slick® treated glass plate and glass slide
Lysis shield gels for single-cell separations (1 mm)	6%T or 20%T	30% (37.5:1) stock; final concentration 6% or 20% w/v	10% (20%T) or 4.66% (6%T) v/v final from stock	none	10% (v/v) final concentration 10X tris-glycine; stored in 2X modified RIPA and transferred to 2X RIPA containing 8M urea for >10 minutes prior to separation.	0.08% APS, 0.08% TEMED	60 mins	Gel Slick® treated glass plate and glass slide

Supplementary **Table 1.** Fabrication conditions for the various types of polyacrylamide gels used in this work.

Supplementary **Table 2.** Projection electrophoresis buffers.

1X tris-glycine and 0.5% Triton X-100	1X tris-glycine	1X RIPA and 1X tris-glycine	2X RIPA and 2X tris-glycine	2X RIPA and 8M Urea
10X tris-glycine: 10% v/v Bio-Rad 1610734	10X tris-glycine: 10% v/v Bio-Rad 1610734	10X tris-glycine: 10% v/v Bio-Rad 1610734	10X tris-glycine: 20% v/v Bio-Rad 1610734	Urea: 8M final (Sigma-Aldrich U5378)
Triton X-100: 0.5% v/v Sigma-Aldrich: X100	MilliQ Water: 90% v/v	SDS: 0.5% w/v Sigma-Aldrich #L3771	SDS: 1% w/v Sigma-Aldrich #L3771	10X tris-glycine: 20% v/v Bio-Rad 1610734
MilliQ Water: 89.5% v/v	--	Sodium Deoxycholate: 0.25% w/v Sigma-Aldrich #D6750	Sodium Deoxycholate: 0.5% w/v Sigma-Aldrich #D6750	SDS: 1% w/v Sigma-Aldrich #L3771
--	--	Triton X-100: 0.1% v/v Sigma-Aldrich: X100	Triton X-100: 0.2% v/v Sigma-Aldrich: X100	Sodium Deoxycholate: 0.5% w/v Sigma-Aldrich #D6750
--	--	MilliQ Water: 89.9% v/v	MilliQ Water: 79.8% v/v	Triton X-100: 0.2% v/v Sigma-Aldrich: X100
--	--	--	--	MilliQ Water: 79.8% v/v

Supplementary Note 1. Consideration of refractive index mismatch on measured z-location in confocal microscopy.

One consideration when comparing light sheet and confocal microscopy is refractive index mismatch between the gel and the objective immersion medium. In confocal microscopy, mismatch in sample vs. immersion medium refractive index results in distortion of the imaging point spread function, as well as distortion of the apparent scanned distance in z:

$$\Delta f = \frac{n_2}{n_1} \frac{\left[1 - \left(\frac{n_1}{n_2}\sin\theta_1\right)^2\right]^{1/2}}{\cos\theta_1} \Delta z,$$

Where Δf is the distance in z scanned by the focal spot, Δz is the distance in z scanned by the objective, n_1 is the objective immersion medium, n_2 is the sample medium, and θ_1 is the angle at which the marginal rays from the objective approach the top of the sample[1]. Although this equation derived from geometric optics is helpful in qualitatively understanding the effects of refractive index mismatch, experimental data often do not follow this relationship (likely due to the high sensitivity to θ_1)[1]. In contrast, with light sheet microscopy we may not expect this distortion of apparent Z-directional distances because the position of the sectioned focal plane is controlled by the physical position of the light sheet within the sample, rather than by the optics of the detection objective. From this distortion function, we would expect to measure migration distances from confocal images shorter than those measured with light sheet microscopy (as n_2, or the gel refractive index, is slightly higher than the water immersion medium n_1). Comparing Supplementary Fig. 4 and **Figure 5l,** we indeed observe that confocal migration distances (Supplementary Fig. 4) are shorter than those measured from light sheet (**Figure 5**l).

Supplementary References

1. Diaspro, A.; Federici, F.; Robello, M. Influence of Refractive-Index Mismatch in High-Resolution Three-Dimensional Confocal Microscopy. *Applied Optics* **2002**, *41*, 685–690.

4. Microgel-membrane chips for expedited and enhanced immunoprobe delivery to gel by electrotransfer

4.1   Introduction

'In-gel' immunoassays find broad utility in characterizing biological systems, including by 3D protein localization in tissue,[1] cellular secretion,[2] and protein mass[3] and charge variants[4] in single-cells. In such immunoassays, the hydrogel acts as a protein scaffolding matrix, immobilizing target analytes in-gel for subsequent detection by diffusive immunoprobing of the gel matrix. However, the analytical sensitivity of in-gel immunoassays suffers from inefficient diffusive probe delivery to gel, as small gel pores relative to large macromolecule probes hinder probe loading to the gel matrix. Specifically, diffusive probe mass loading to a hydrogel is hindered by size-exclusion partitioning, which reduces the diffusive equilibrium concentration of antibody probes in a hydrogel matrix compared to their concentration in free solution.[5] The impact that inefficient probe delivery to gel has on target protein – antibody probe reaction kinetics is that both the (i) maximum equilibrium immunocomplex formation and (ii) rate of immunocomplex formation can be drastically reduced.[6]

To enhance the total probe mass delivered to in-gel immunoassays, electrotransfer probing has recently been developed by drawing inspiration from gel-to-membrane protein electrotransfer used in conventional Western blotting.[7,8,9] Electrotransfer probing drives probe delivery to gel by applying an electric field across an electrically conductive, free-standing stack of a probe reservoir layered onto an in-gel immunoassay. Critical to the functionality of electrotransfer probing is being able to conduct electrical current through the entirety of the probe reservoir and in-gel immunoassay stack. As a result, electrotransfer probing has only been applied to free standing gels; specifically, thick, mm-scale in-gel immunoassays that are mechanically robust enough to maintain structural integrity without being grafting to a glass slide support substrate.[7,8,10]

Yet, an important class of in-gel immunoassays utilize microns-thin gels grafted onto mechanically robust, but electrically nonconductive, glass slide support. Such 'microgel' immunoassays are powerful tools with applications in massively parallelized protein and DNA electrophoresis,[3,11,12,13] but suffer from the same analytical sensitivity challenges conferred by diffusively-driven in-gel immunoprobing. Thus, to expand the applicability of electrotransfer probing to microgel immunoassay chips, there is a need to develop a mechanically robust, yet electrically conductive and imaging-amenable support material to replace glass in microgel chips.

Here, we introduce a microgel-membrane chip that supports rapid and enhanced delivery of probe the microgel immunoassay chips by electrotransfer. In developing this chip, we reengineer the conventional microgel chip to support electrotransfer probe loading by grafting the microgel to an electrically conductive membrane (instead of an electrically nonconductive glass slide) via novel membrane silanization and chip fabrication methods. We additionally establish engineering design rules for mitigating diffusive probe losses during electrotransfer probe loading, and characterize the electrical conductivity of silane-treated membranes. Finally, we demonstrate that our electrically conductive microgel-membrane chip supports rapid electrotransfer probe loading, and

results in greater probe mass loading to the microgel in less time compared to diffusive probe loading.

4.2   Experimental Section

Membrane Silanization.
To facilitate covalent binding of polyacrylamide gel (10%T, 3.5C) to the nanoporous membranes (regenerated cellulose, Spectra Por RC Dialysis Tubing, 3.5 kDa MWCO, #132725T), a membrane silanization method was developed with inspiration from glass slide silanization protocols[14] and fabrication techniques for hybrid gel-cellulose materials.[15,16,17] A detailed procedure is described in the Supporting Information.

Microgel-Membrane Chip Fabrication.
The microgel-membrane chip is fabricated by: (i) layering a hydrated membrane onto a glass slide and allowing the membrane to dry, (ii) applying a polyacrylamide gel precursor solution onto a SU-8 micropost patterned silicon wafer, (iii) placing the membrane-glass slide assembly onto the precursor solution and allowing the gel to polymerize and covalently graft to the membrane, (ii) removing the polymerized gel from the wafer and peeling away the microgel-membrane chip from the glass support. Gel precursor solution was prepared as previously described.[14]

**Electrical Conductivity Measurements.**
The electrical conductivity measurements were performed using an electrotransfer system composed of two buffer reservoirs (1× Tris-glycine). A detailed procedure of experimental operation is provided in the Supporting Information.

Probe Loading Experiments and Image Analysis.
Imaging was performed on a fluorescence microarray scanner (Genepix 4300A, Molecular Devices). Analysis of in-microgel fluorescence images was performed using custom scripts in ImageJ and Matlab. A detailed procedure of experimental operation is provided in the Supporting Information.

4.3   Results and Discussion

Electrotransfer probe loading in the microgel chip is facilitated by grafting a thin (50 μm) microgel layer onto a silane-treated nanoporous membrane (Figure 1A,B). Conventionally, microgels are grafted onto support materials (e.g., glass, GelBond) to prevent microgel deformation during assay performance. The membrane prevents microgel deformation but is electrically conductive. The free-standing microgel-membrane chip supports delivery of probe molecules into the microgel matrix by electrotransfer for (i) enhanced total probe mass in microgel and (ii) reduced timescales of probe delivery (Figure 1C).
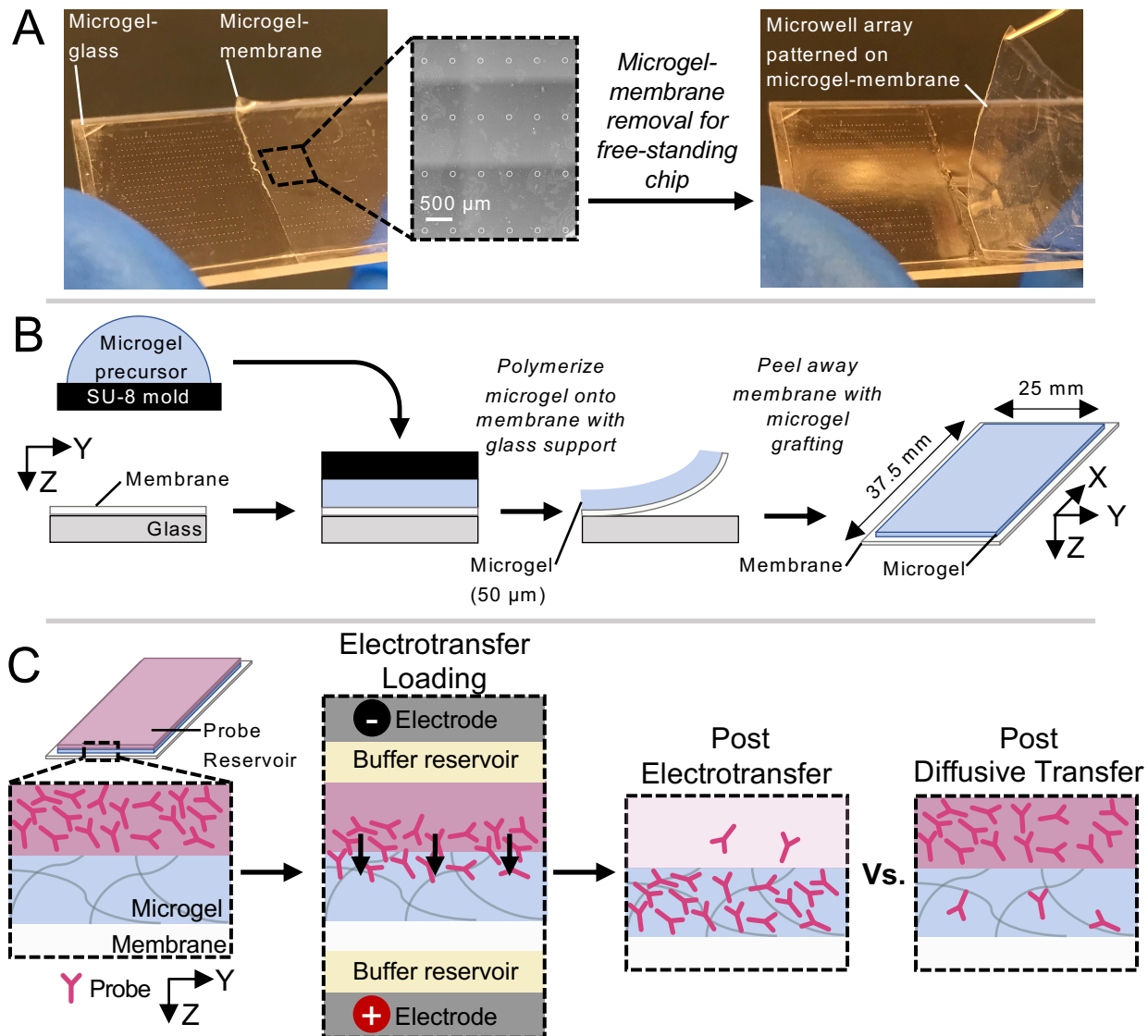
Figure 1. Microgel-membrane fabrication method results in a free-standing chip that supports delivery of probe molecules into the microgel by electrotransfer. (A) Brightfield image of microgel-membrane chip first supported by glass slide, then removed from the glass slide to produce a freestanding microgel-membrane chip. (B) Polyacrylamide microgels are grafted onto membranes using silanization chemistry atop an SU-8 mold that patterns microwells into the microgel layer. To polymerize the polyacrylamide gels onto membranes, polyacrylamide gel precursor was cast in a layered assembly involving: full glass slide, nanoporous membrane, polyacrylamide precursor solution, microwell patterned wafer. (C) Electrotransfer probe loading to the microgel chip offers improved total probe loading mass and reduced loading timescales.
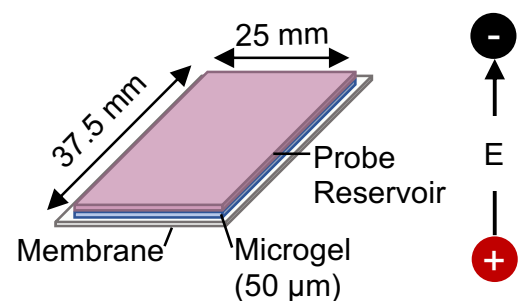
Minimizing Diffusive Probe Losses During Probe Loading.

We first sought to understand diffusive probe losses from open microgel layers during electrotransfer probe loading in two electrotransfer system designs: 'out-of-plane' electrotransfer system (Figure 2A) and 'in-plane' electrotransfer system (Figure 2B). As probe molecules are electromigrated through the microgel, the molecules also undergo three-dimensional diffusion. Diffusive losses of probe molecules from the microgel can occur as probe molecules diffuse out of the microgel into the surrounding environment. We thus aimed to design an electrotransfer system to minimize the diffusive loss of probe during electrotransfer loading of probe to the microgel.

To assess the diffusive loss of probe expected during electromigration in the 'out-of-plane' and 'in-plane' electrotransfer systems, we defined a Peclet number (Pe) as the ratio of the time for diffusive probe loss from the microgel (t_D) to the time to electrotransfer probe into the microgel (t_E). The Pe number for the 'in-plane' system ($Pe_{Lateral}$) is given by

$$Pe_{Lateral} = \frac{t_D}{t_E} = \frac{\left[\frac{Z^2}{2 \cdot D}\right]}{\left[\frac{Y}{\mu \cdot E}\right]}$$
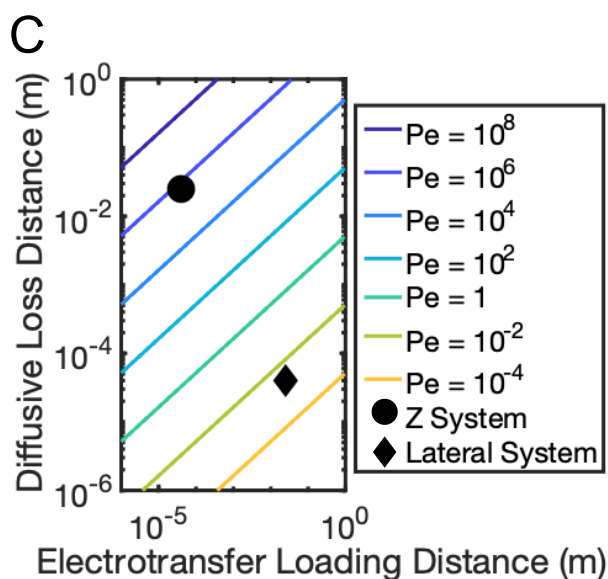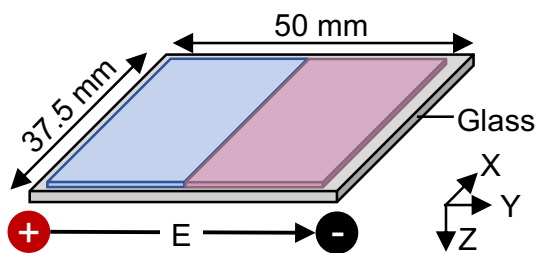
Figure 2. Peclet analysis of electrotransfer systems indicates 'out-of-plane' design minimizes diffusive probe loss during electrotransfer loading. (A) Schematic showing the 'out-of-plane' electrotransfer system. (B) Schematic showing the 'in-plane' electrotransfer system. (C) A Peclet analysis of electrotransfer probe loading shows that the Peclet number in 'out-of-plane' system is ~$10^8 \times$ greater than in 'in-plane' system.

where Z is the microgel thickness (50 μm), D is the diffusion coefficient of probe in the microgel (2.4 μm²/s), Y is the width of the microgel (25 mm), μ is the electrophoretic mobility of probe in the microgel (1.81×10^{-9} m²/Vs), previously determined[7] and E is the applied electric field (100 V/cm). The Pe for the 'out-of-plane' system (Pe_Z) is calculated as

$$Pe_Z = \frac{t_D}{t_E} = \frac{\left[\frac{Y^2}{2 \cdot D}\right]}{\left[\frac{Z}{\mu \cdot E}\right]}$$

We hypothesized that due to the disproportional length scales of the microgel thickness in Z (50 μm) compared to the mm-scale length and width of the microgel chip in X and Y (25 mm and 37.5 mm), electrotransfer loading of probe in the 'out-of-plane' system would minimize expected diffusive losses.

Results of this analysis are presented in Figure 2C and indicate that the Peclet number in the 'out-of-plane' electrotransfer system is ~$10^8\times$ greater than in the 'in-plane' system. The disproportionate length scales (in Z vs. X-Y) specifically minimize diffusive probe losses in the 'out-of-plane' electrotransfer system as (i) the electromigration distance, and thus probe loading time, is shortest in the Z axis and (ii) the migration distances for diffusive losses are longest in X and Y axes. The Pe analysis in electrotransfer probing thus provides a design rule for minimizing diffusive probe losses, and indicate that minimal losses occur in the 'out-of-plane' electrotransfer system format.

Investigating the Fidelity of the Microgel-Membrane Chip Fabrication Process.
As the membranes had not been previously demonstrated as a microgel support material, we aimed to assess the fidelity of the microgel-membrane chip fabrication process in comparison to conventional microgel-glass chip fabrication. To aid in fidelity assessments, we pattern microwell features into the microgel layer of both chip types, and compare dimensions of the microwell feature across chips. We anticipated that there would be no significant difference in the dimensions of microwell features patterned into the microgel-membrane and microgel-glass chips.

Microgel-membrane and microgel-glass chips were fabricated with a fluorescent dye (RhodamineB) included in the gel precursor solution to visualize polymerized gel features and allow for comparison between the two chip types (Figure 3A; additional information provided in the Supporting Information). We anticipated that Rhodamine B would be present in both the microgel and membrane layers, as the molecular mass of Rhodamine B (~472 Da) is below the molecular weight cut-off of the membrane (3.5 kDa). The height and diameter of the microwell structure were quantified.

We observe no significant difference in the height and diameter of the microwell structure between microgels fabricated in microgel-glass chips and microgel-membrane chips (n = 8, p > 0.05 for both dimensions, Mann-Whitney U-test, Figure 3B). Interestingly, Rhodamine B molecules appear to aggregate at the interface of microgel and membrane layers in the microgel-membrane chip. We attribute the Rhodamine B aggregation at the microgel-membrane interface to non-specific

hydrophobic interactions between Rhodamine B and the silane present on the membrane surface.[18]
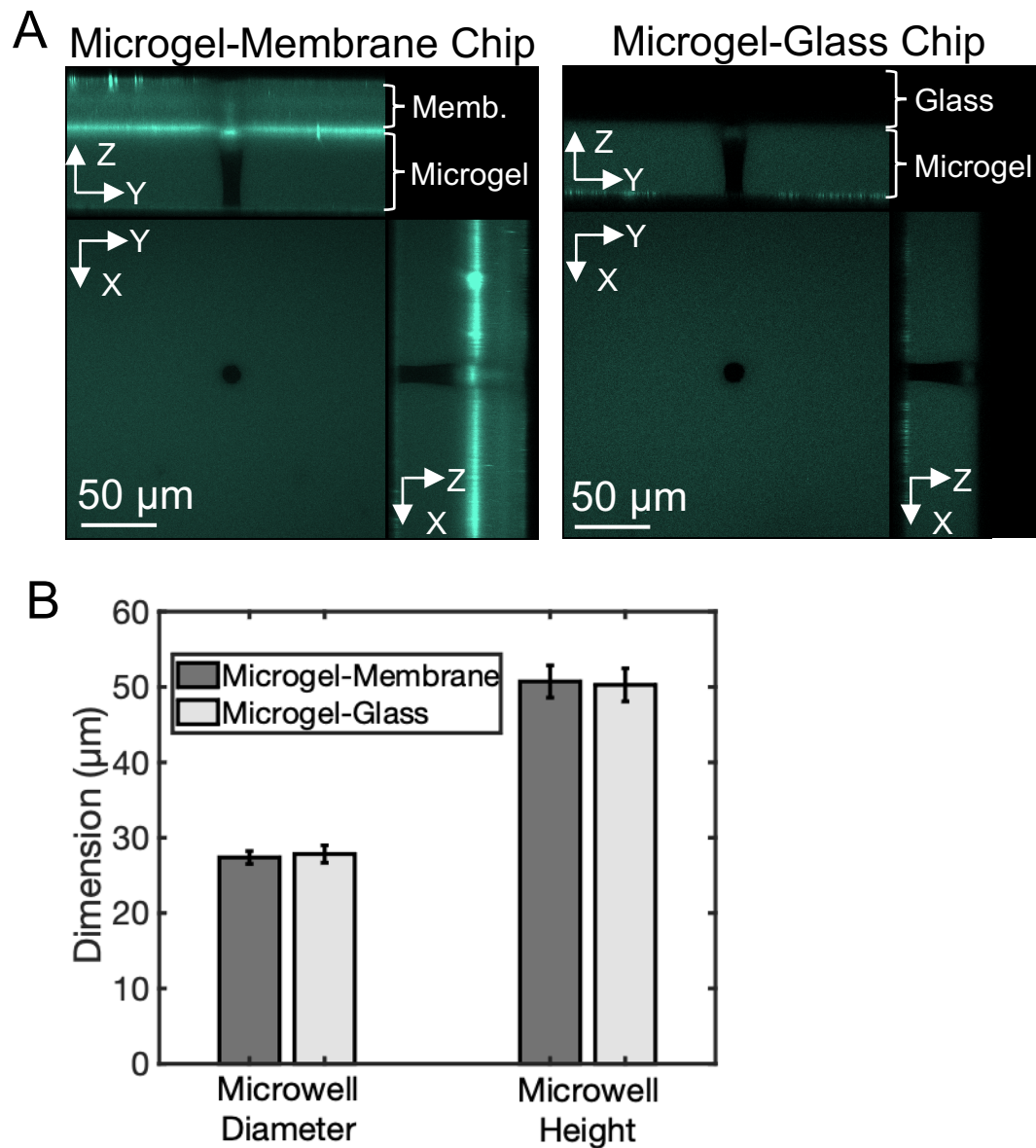
Figure 3. Microwell patterning into microgel-membrane chips. (A) Fluorescent confocal microscopy images of a single microwell in a microgel immunoassay chip composed of microgel-glass layers and microgel-membrane layers. Rhodamine B fluorescence shown in turquoise. (B) The microgel-membrane fabrication technique does not perturb the height and diameter of individual microwells compared to the conventional microgel-glass chip fabrication technique.

**Assessment of Membrane Electrical Conductivity Post-Silanization.**

We next sought to characterize the electrical conductivity of the membranes after silane treatment. To do so, we used an electrotransfer system composed of three layers: two identical buffer reservoirs that sandwich a material under investigation (membrane, glass, or no membrane). A constant voltage was applied to the electrotransfer system and the system can be represented by an electrical circuit in which each material layer is described by a resistor in series (Figure 4A).

No electrical current was detected in the electrotransfer system that included a glass layer, indicating that the electrical current was below the minimum electrical current operating limit of the power supply at all time points (Figure 4B). This supports our understanding of the incompatibility of microgel-glass chips with electrotransfer probing systems. We observe that the initial electrical current ($t = 0$ s) for the system with a membrane is $67.2\% \pm 5.1\%$ of the initial electrical current of the system with no membrane ($p < 0.05$, Mann-Whitney U test; Figure 4B). For the final electrical current ($t = 60$ s), we observe that the final electrical current for the membrane system is $67.2\% \pm 8.9\%$ of the final electrical current of the no membrane system ($p < 0.05$, Mann-Whitney U test; Figure 4). We additionally observe that the electrical current decays over the 60 s of applied constant voltage in both of the electrotransfer systems that included either the membrane or no membrane (Figure 4B). The electrical current time decay is expected as gas products of electrolysis that form at the electrode plates may act to increase the resistivity of the buffer reservoirs over time.[7,19] Additionally, the electrical current time decay may be caused by liquid evaporation from the buffer reservoir as a result of joule heating in the electrotransfer system.[10,20,21,22,23] Time-varying buffer reservoir resistivity and joule heating in the electrotransfer system can have detrimental impacts on probe electrotransfer performance, including non-uniform rates of probe electromigration or probe molecule denaturation via excessive system heating, as has been described in previous electrotransfer systems.[19,24,22,23] Further studies of this work would build on the engineering design of similar electrotransfer systems to mitigate the adverse impacts of joule heating and electrolysis on molecule transport.[7,10]

To specifically investigate the intrinsic properties of the membrane (i.e. electrical conductivity) and disassociate our investigation from the time-dependent impacts of the preliminary electrotransfer system assembly, we calculated the electrical conductivity of the membrane using the initial electrical current ($t = 0$ s). Using the electrical circuit representation in Figure 4A, we first calculated the resistance at $t = 0$ s of the individual buffer reservoir, R_{Buffer}, and the membrane, $R_{Membrane}$, and find that $R_{Buffer} \sim R_{Membrane}$ (Figure 4C). Thus, for the electrotransfer system including a membrane (Figure 4A), the total resistance of the two buffer reservoirs is twice as large as the total resistance of the single membrane, as shown in Figure 4C. To calculate the electrical conductivity of the membrane and the buffer reservoir layers, we scale R_{Buffer} and $R_{Membrane}$ by the dimensions of each material layer and observe $\sim 10^3 \times$ lower electrical conductivity of the membrane than the buffer reservoir (Figure 4D). Importantly, while the membrane is less electrically conductive than the buffer reservoir, the membrane is quite thin (20 μm vs. 2 cm per buffer reservoir), and thus the total resistance of the membrane layer is comparable to the resistance of each buffer reservoir. We additionally compare our experimentally determined electrical conductivities of the buffer reservoir and membrane to a previously reported glass electrical conductivity value and note that the membrane is $>10^{10} \times$ more electrically conductive than glass.[25] Ultimately, while the membrane is less electrically conductive than the buffer reservoir, the membrane offers $>10^{10} \times$ improvement in electrical conductivity in comparison to glass as a support material in conventional microgel chips.

Electrotransfer Probe Loading to Microgel-Membrane Chips.

Finally, we sought to implement electrotransfer probe loading in the microgel-membrane chips. We hypothesized that electrotransfer probe loading (as compared to conventional diffusive probe loading) would result in (i) expedited timescale of probe delivery to microgel and (ii) enhanced total mass of probe delivered to microgel. To evaluate the performance of electrotransfer probe loading, microgel-membrane chips were fabricated as described in Figure 1, and the electrotransfer system shown in Figure 5A was assembled. The probe reservoir is composed of agarose gel
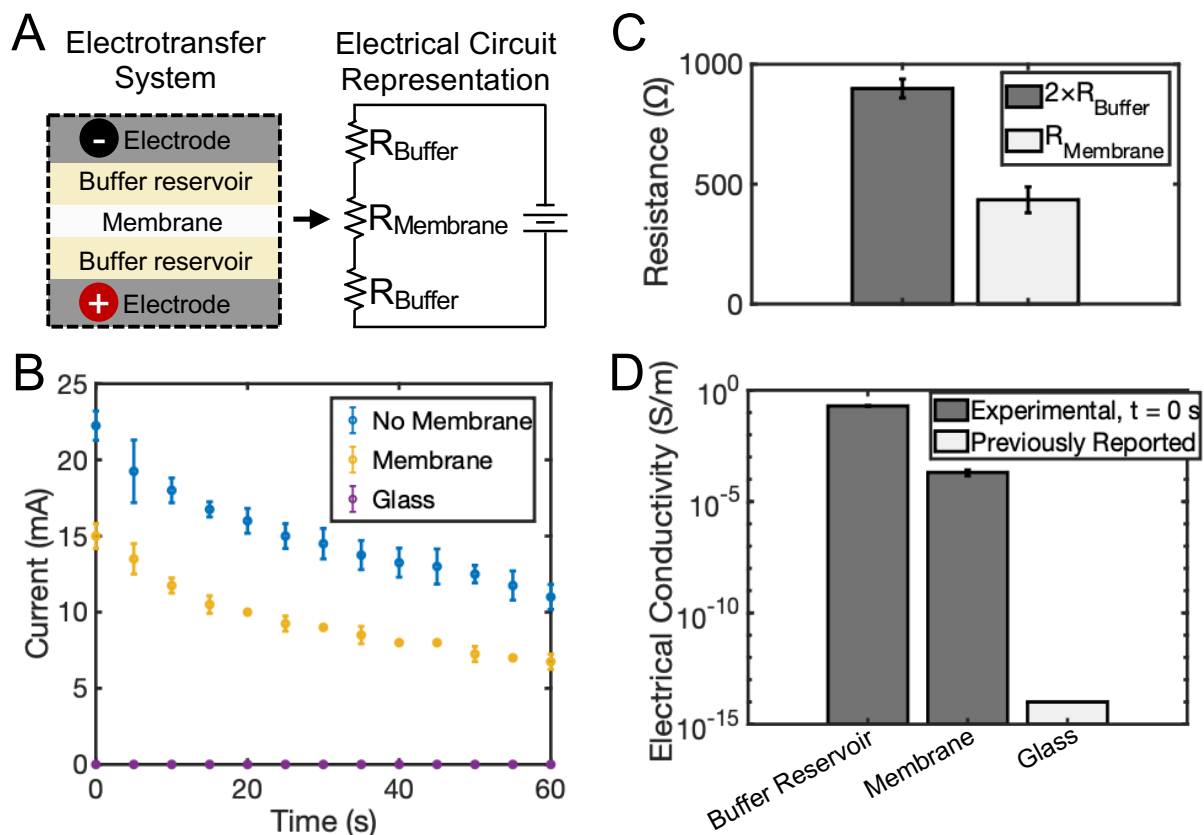

Figure 4. Electrical properties of the membrane (post-silanization) in comparison to buffer reservoir and glass. (A) Schematic of the electrotransfer system (not to scale) and an electrical circuit analog. (B) Electrical current over time through the electrotransfer system assemblies composed of two buffer reservoirs sandwiching either: (i) no membrane, (ii) membrane (post-silanization), or (iii) glass. (C) Resistance of each layer of the electrotransfer system is determined using the electrical circuit analog. (D) The electrical conductance of the buffer reservoir and membrane are calculated and compared to previously reported glass electrical conductivity values. (n = 4 per condition)

(100 μm thick), and was fabricated protocol described in previous electrotransfer probing systems.[7] To ensure probe electromigration out of the probe reservoir, the following electrotransfer parameters were chosen: 50 V/cm electric field, applied for 1 min. These electrotransfer conditions correspond to probe electromigration in agarose of >300 μm, >3× greater than the 100 μm probe reservoir (assumes electrophoretic mobility of probe in agarose of 1.16×10^5 cm^2/Vs, previously

characterized[7]). In the diffusive conditions, we replicate conventional diffusive probing strategies in microgel-glass chips by not removing the microgel-membrane assembly from the glass slide support used during chip fabrication (Figure 1B).[14]

We observe that 1 min of electrotransfer loading results in $79.85 \pm 26.43\times$ greater in-microgel probe fluorescence than 1 min of diffusive loading, and $5.01 \pm 1.67\times$ greater in-microgel probe fluorescence than 1 hr of diffusive loading ($p < 0.05$ Mann-Whitney U test; Figure 5C). As expected, we additionally observe a $15.94 \pm 3.88\times$ increase in in-microgel probe fluorescence from the 1 min diffusive condition to the 1 hr diffusive condition, indicating that 1 min of diffusive transfer is insufficient time to reach transport equilibrium ($p < 0.05$ Mann-Whitney U test; Figure 5C). Taken collectively, our results support our hypothesis and engineering design of the microgel-membrane chip as a system that supports electrotransfer probe delivery to the microgel, resulting in (i) enhanced total probe mass in microgel and (ii) reduced timescales of probe delivery
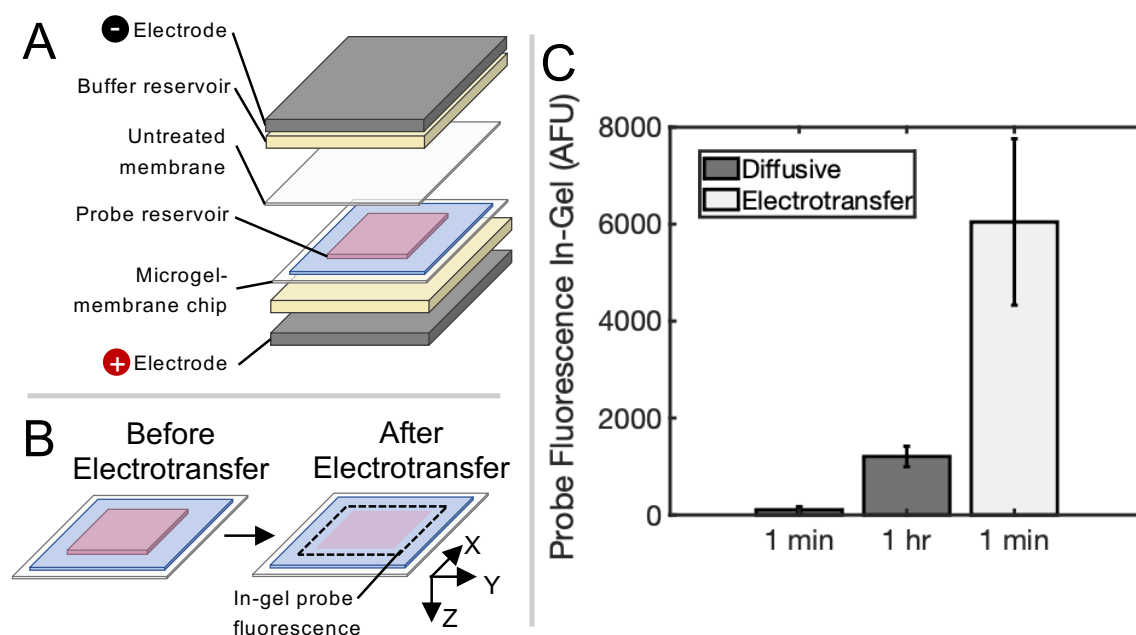
Figure 5. Electrotransfer probe loading to the microgel-membrane chip results in enhanced total probe mass in microgel and reduced timescales of probe delivery. (A) Schematic of the assembly used in electrotransfer probe loading to microgel-membrane chip. (B) Fluorescent probe delivered into the microgel is measured by imaging the surface of the microgel chip after electrotransfer. (C) Electrotransfer probe loading for 1 min results in greater probe delivered to microgel than diffusive probe loading for 1 min and 1 hr ($n = 4$ for each condition, $p < 0.05$ for all pair-wise condition comparisons, Mann-Whitney U test).

(compared to conventional diffusive probing). Interestingly, we observe an increase in the coefficient of variation (CV) of probe loaded in microgel by electrotransfer compared to the diffusive loading (28.4% in 1 min electrotransfer, 17.5% in 1 hr diffusive). Further studies are required to reduce run-to-run variability in total probe delivered to the microgel by electrotransfer. Our future work may be informed by previous electrotransfer probing systems that have achieved <5% CV in total probe delivered to mm-scale hydrogels by mitigating adverse impacts of

electrolysis on run-to-run variability.[7,10] In particular, (i) pH changes in the buffer reservoir may be prevented by increasing buffering capacity, (ii) temperature variability may be reduced by incorporating robust heat dissipation mechanisms, and (iii) resistivity variability in the buffer reservoir may be mitigated by incorporating a gas bubble removal mechanism.

4.4   Conclusions

We introduced a microgel-membrane chip that supports rapid and enhanced electrotransfer probe delivery to microgel layers, overcoming a fundamental challenge to probe delivery to microgel immunoassays. Our design involves performing an analytical investigation of electrotransfer probe loading systems, and establishing a Peclet number as a design guideline for minimizing diffusive probe losses during electrotransfer probe loading. We additionally describe a fabrication method for the novel microgel-membrane chips, involving grafting a polyacrylamide microgel to a membrane via membrane silanization chemistry. Further, we assess key traits of the microgel-membrane chip, including microgel fabrication fidelity and the electrical conductivity of silane-treated membranes. Lastly, we observe 1 min of electrotransfer probe loading in our microgel-membrane chip to result in ~80× greater probe delivery than 1 min of diffusive delivery, and ~5× greater probe delivery than 1 hr of diffusive delivery. We see these findings being applied to critically advance throughput and analytical sensitivity of microgel-based single-cell separation technologies. Next steps of this work include the identification of sources of variability in total probe mass delivered to microgel by electrotransfer and implementation of the microgel-membrane chip for in-gel immunoblotting by electrotransfer probing.

4.5 References

1 K. Chung, J. Wallace, S.-Y. Kim, S. Kalyanasundaram, A. S. Andalman, T. J. Davidson, J. J. Mirzabekov, K. A. Zalocusky, J. Mattis, A. K. Denisin, S. Pak, H. Bernstein, C. Ramakrishnan, L. Grosenick, V. Gradinaru and K. Deisseroth, *Nature*, 2013, **497**, 332–337.

2 D. C. Appleyard, S. C. Chapin and P. S. Doyle, *Anal. Chem.*, 2011, **83**, 193–199.

3 A. J. Hughes, D. P. Spelke, Z. Xu, C.-C. Kang, D. V Schaffer and A. E. Herr, *Nat. Methods*, 2014, **11**, 455–464.

4 A. M. Tentori, K. A. Yamauchi and A. E. Herr, *Angew Chem Int Ed Engl*, 2016, **55**, 12431–12435.

5 H. Park, C. S. Johnson and D. A. Gabriel ', *Macromolecules*, 1990, **23**, 1548–1553.

6 J. A. Goodrich and J. F. Kugel, *Binding and Kinetics for Molecular Biologists*, Cold Spring Harbor Laboratories Press, Cold Spring Harbor, 2007.

7 A. P. Mourdoukoutas, S. M. Grist and A. E. Herr, *Anal. Methods*, , DOI:10.1039/d0ay01203c.

8 S.-Y. Kim, J. H. Cho, E. Murray, N. Bakh, H. Choi, K. Ohn, L. Ruelas, A. Hubbert, M. McCue, S. L. Vassallo, P. J. Keller and K. Chung, *Proc. Natl. Acad. Sci. U. S. A.*, 2015, **112**, E6274-83.

9 H. Towbin, T. Staehelin and J. Gordon, *Proc. Natl. Acad. Sci.*, 1979, **76**, 4350–4354.

10 S. M. Grist, A. P. Mourdoukoutas and A. E. Herr, *Nat. Commun. 2020 111*, 2020, **11**, 1–17.

11 T. A. Duncombe and A. E. Herr, *Lab Chip*, 2013, **13**, 2115.

12 S. Li, Z. Wen, B. Ghalandari, T. Zhou, A. R. Warden, T. Zhang, P. Dai, Y. Yu, W. Guo, M. Liu, H. Xie and X. Ding, *Adv. Mater.*, , DOI:10.1002/adma.202170172.

13 D. K. Wood, D. M. Weingeist, S. N. Bhatia, B. P. Engelward, B. P. E. Designed, D. M. W. Performed and B. P. E. Analyzed Data, , DOI:10.1073/pnas.1004056107/-/DCSupplemental.

14 C.-C. C. Kang, K. A. Yamauchi, J. Vlassakis, E. Sinkala, T. A. Duncombe and A. E. Herr, *Nat Protoc*, 2016, **11**, 1508–1530.

15 M. Abdelmouleh, S. Boufi, A. ben Salah, M. Naceur Belgacem and A. Gandini, *Langmuir*, 2002, **18**, 3203–3208.

16 M. Abdelmouleh, S. Boufi, M. N. Belgacem, A. P. Duarte, A. Ben Salah and A. Gandini, *Int. J. Adhes. Adhes.*, 2004, **24**, 43–54.

17 M. Abdelmouleh, S. Boufi, M. N. Belgacem, A. Dufresne and A. Gandini, *J. Appl. Polym. Sci.*, 2005, **98**, 974–984.

18 Yide Han, Weiwei Li, Jing Zhang, Hao Meng, Yan Xu and Xia Zhang, *RSC Adv.*, 2015, **5**, 104915–104922.

19 R. Ventzki, S. Rüggeberg, S. Leicht, T. Franz and J. Stegemann, *Biotechniques*, 2007, **42**, 271–279.

20 J. Vlassakis and A. E. Herr, *Anal. Chem.*, 2017, **89**, 12787–12796.

21 L. Zhu, M. A. Tangrea, S. Mukherjee and M. R. Emmert-Buck, *Proteomics*, 2011, **11**, 883–889.

22 A. Goldman and D. W. Speicher, *Curr. Protoc. Protein Sci.*, 2015, **82**, 10.7.1.

23   R. Ventzki and J. Stegemann, *Electrophoresis*, 2003, **24**, 4153–4160.

24   Y. Akazawa-Ogawa, H. Nagai and Y. Hagihara, *Biophys. Rev.*, 2018, 10, 255–258.

25   N. P. Bansal and R. H. Doremus, *Handbook of Glass Properties*, Elsevier Inc., 2013.

4.6   Supporting Information

Chemicals/Reagents.

Acetic acid (#A6283), 3-(trimethoxysilyl)propyl methacrylate (#662275), 30% T, 3.4%C acrylamide/bis-acrylamide (29:1) (#A3574), N,N,N′,N′-tetramethylethylenediamine (TEMED, #T9281), ammonium persulfate (APS, A3678), 1.5% w/v Ultrapure low melting point agarose (Invitrogen, #16520050), Donkey antirabbit Alexa-Fluor 647-labeled secondary antibodies (Invitrogen, #A31573).

Membrane silanization.

First, the membranes were cut into 25 x 37.5 mm single sheets (not tubes), soaked in ethanol for 48 hours, and air dried for 24 hours. Then, silane solution was prepared by mixing: 140 mL 3-(3-(trimethoxysilyl)propyl methacrylate), 210 mL acetic acid, 350 mL DI water. The silane solution was degassed in a sonicator for 10 min. Next, the membranes were submerged in silane solution for 2 hrs, subsequently air dried for 48 hrs, then heated at 120C for 2 hrs in oxygen deprived atmosphere (vacuum furnace). Finally, membranes were washed by agitating in baths of (1 min each bath): (1) methanol, (2) DI water, (3) methanol, (4) DI water. Silanized membranes were stored with desiccant in a sealed container at 4C until use.

Investigating the Fidelity of the Microgel-Membrane Chip Fabrication Process.

Microgel-membrane and microgel-glass chips were fabricated with a fluorescent dye (RhodamineB) included in the gel precursor solution to visualize polymerized gel features and allow for comparison between the two chip types. After polymerization, gels were exposed to UV light to photocapture Rhodamine B in gel. The gels were subsequently diffusively washed in DI water for 48 hrs to remove unbound Rhodamine B molecules. Hydrated microgel-membrane and microgel-glass chips were then imaged using fluorescence confocal microscopy and Rhodamine B was used as a proxy for gel and membrane location.

Assessment of Membrane Electrical Conductivity Post-Silanization.

To evaluate the electrical conductivity of the membranes, the membranes were used to separate two buffer reservoirs and an electric field was applied across the assembled system. Buffer reservoirs were each composed of 2 mm thick filter papers soaked in 1× Tris-glycine and electric field of 50 V/cm was applied for 60 s by interfacing the buffer reservoirs with graphite electrode plates connected to a high voltage power supply (4 cm electrode-to-electrode spacing, 20 V applied, constant voltage). The resulting electrical current through the system was measured while the electrical potential difference was applied. To compare the electrical current conductivities of the membranes to positive and negative control systems, we assembled additional systems in which

an electrical potential difference was applied across two buffer reservoirs separated by either a No. 1 glass cover slip (negative control) or no separation material (positive control). The electrical conductivity of each system was assessed by using the initial electrical current (time = 0s) and the final electrical current (time = 60 s).

Electrotransfer Probe Loading to Microgel-Membrane Chips.

We fabricated microgel-membrane chips as described in Figure 1 of the Main Text. To replicate conventional diffusive probing strategies in microgel-glass chips, the microgel-membrane assembly was not removed from the glass slide used during chip fabrication. In electrotransfer conditions, the microgel-membrane was removed from the glass slide so that the microgel-membrane chip was freestanding and compatible with electrotransfer probing. To contain probe in a defined reservoir prior to electrotransfer delivery, a 100 μm thick agarose gel layer containing probe was layered on top of the microgel-membrane chip. The microgel-membrane chip and probe reservoir were sandwiched by two buffer reservoirs, each composed of 2 mm thick filter papers soaked in 1× Tris-glycine. To electrotransfer probe, an electric field of 50 V/cm was applied for 60 s by interfacing the buffer reservoirs with graphite electrode plates connected to a high voltage power supply (4 cm electrode-to-electrode spacing, 20 V applied, constant voltage). After probe delivery, excess probe remaining in the fluid layer above the microgel chip was washed off the microgel surface by briefly (~2 s) dipping the microgel in 1× Tris-glycine. The probe was then immobilized in gel using a UV-mediated benzophenone photocapture chemistry, as previously described.[5] To assess the efficacy of probe loading into the microgel, the probe fluorescence in microgel was measured before and after probe loading, and the difference in probe fluorescence in-gel was calculated (Figure 5B). Antibody probe reservoir were 1:10 dilutions from stock in either: 2% BSA/TBST (diffusive), or 1.5% agarose in 1× Tris-glycine (electrotransfer). 5 μg of antibody per 25 x 37.5 mm chip.

5. Simulated and Experimental Feasibility of Using an Offset Electrode Configuration for Direct Electrotransfer

5.1. Introduction

Problem

Conventional western blotting protocols involve multiple hands-on steps that are time consuming. Furthermore, during the blotting step when proteins are transferred from the separation gel to the membrane, there is a risk of over transferring smaller molecular weight species such that they pass through the membrane. To address both of these concerns, Thermo Fisher Scientific designed a prototype electrotransfer system with an "offset" electrode configuration that would leverage electrotransfer of protein in both the vertical and lateral dimensions. The offset design has the potential to 1) prevent over transferring smaller-sized species, retaining smaller proteins laterally on the blotting membrane as larger proteins elute from the gel and 2) simplify the conventional western blot workflow by minimizing handling. However, due to the addition of the lateral dimension, non-uniformities arise in electric field and path length, as expected from theory, resulting in performance losses such as lower transfer efficiency, particularly with higher molecular weight targets and protein band dispersion. Thus, we determined the operational regimes and performance losses for gel to membrane electrotransfer of separated proteins using an 'offset electrode configuration' compared to conventional vertical electrotransfer.

Method

To investigate the impact of electrode placement on the electric field magnitude and electrical current path, we developed a finite element analysis model (COMSOL Multiphysics®) to predict the electric field magnitude and electrical current path in various electrotransfer system designs, and used the results to develop a modeling framework to approximate protein migration velocity (and thus electrotransfer transfer times) as functions of gel density, protein size, and EZ. We then experimentally validated the results of the model using the offset electrode configuration with standard 1 mm thick gels and thin (~100 μm) gels, comparing transfer performance to the standard vertical electrotransfer. Due to the losses observed in the offset electrode configuration system, we proposed and modeled alternative electrode designs to increase EZ magnitude and reduce non-uniformity of protein electrotransfer times.

Major Results

In the initial offset electrode configuration (Gen 1.0), modeling results indicated that the EZ magnitude is 10-1-10-4 lower than in conventional electrotransfer, which adversely impacts electrotransfer protein velocities of large molecule weight species in particular. These modeling results were experimentally confirmed, as poor electrotransfer of large molecular weight species was observed in the Gen 1.0 system. As predicted by the models, attempts to increase the EZ magnitude for the large molecular weight species did not improve elution of larger molecular weight species from the gel. Furthermore, reducing gel thickness by a single order of magnitude did not make up for the >102-fold difference in EZ to improve transfer performance. To increase

the EZ magnitude, alternative 'offset' electrode assemblies were designed with the following modifications: reduced electrode spacing from 20 mm to 1 mm (Gen 1.1 system), inclusion of multiple anodes with one on either side of the cathode (Gen 2.0 system), and a wire mesh anode placed directly below the cathode (Gen 2.1 system). Investigation of the EZ magnitudes in the alternative systems was performed by modeling analysis: the Gen 1.1 system EZ ranges from 10-1 to 10-3, the Gen 2.0 system EZ ranges from 10-1 to 10-2, and the Gen 2.0 system EZ ranges from 100 to 10-1, compared to conventional electrotransfer Ez magnitudes.

Outcome/Conclusions
The offset electrode configurations resulted in non-uniform, lower EZ magnitude compared to the conventional vertical electrode configuration. The reduced EZ magnitude adversely impacts protein transfer time, as protein migration velocity is linearly related to EZ and this is particularly detrimental for transfer of large molecular weight species. Experimentally, large molecular weight species were not able to transfer and adjustments to increase the electric field were not sufficient to improve transfer performance. Alternative geometries that maintain comparable EZ to the standard vertical electrotransfer geometry, such as the wire mesh electrode directly below the gel, may result in less performance loss during transfer and would require additional experimental investigation to assess efficacy of large molecular weight species transfer in such systems.

5.2. Results and Discussion

Investigation of EZ in Conventional and Gen 1.0 Electrotransfer Systems by Modeling Analysis
To investigate the impact of electrode placement on the electric field magnitude and electrical current path, we developed a finite element analysis model (COMSOL Multiphysics®) to predict the electric field magnitude and electrical current path in various electrotransfer system designs (Figure 1). We applied this modeling analysis to a conventional electrotransfer system (Figure 1A-C), as well as to an electrotransfer system involving an offset electrode arrangement (Gen 1.0 device; Figure 1D-F).

As expected, modeling analysis in the conventional system indicates that current path is parallel to the Z-axis throughout the entire electrotransfer system (Figure 1A), and thus the magnitude of electric field that contributes to protein electrotransfer (parallel to the Z-axis, E_Z; V/cm) is uniform throughout the entire electrotransfer system (Figure 1B). To specifically evaluate the magnitude of E_Z in the active protein electrotransfer region in relation to the average magnitude of E_Z in the entire electrotransfer system, we plotted a dimensionless E_Z at the gel-membrane interface as a function of X-location (Figure 1C). The dimensionless E_Z is determined by dividing the magnitude of the X-location specific E_Z by the average magnitude of E_Z in the entire electrotransfer system, facilitating direct comparison of E_Z at the active protein electrotransfer region to the average E_Z in the system.

We observe dimensionless $E_Z = 1$ at all X-locations, indicating uniform E_Z magnitude that is additionally equivalent to the average Ez magnitude in the electrotransfer system.

Application of our modeling analysis to the Gen 1.0 device shows that the electrical current path is non-uniform throughout the electrotransfer system and includes components in X and Z dimensions (Figure 1D). We additionally find that the E_Z magnitude is non-uniform, particularly at the gel-membrane interface (Figure 1E). To compare the E_Z magnitude in the Gen 1.0 device to the average E_Z in the conventional system, we non-dimensionalized the E_Z at the gel-membrane interface in the Gen 1.0 device by dividing E_Z by the average E_Z in the conventional system. The dimensionless E_Z is plotted as a function of X-location, showing that the E_Z magnitude is 10^{-1}-10^{-4} lower than in conventional electrotransfer (Figure 1F).

As expected, modeling analysis in the conventional system indicates that current path is parallel
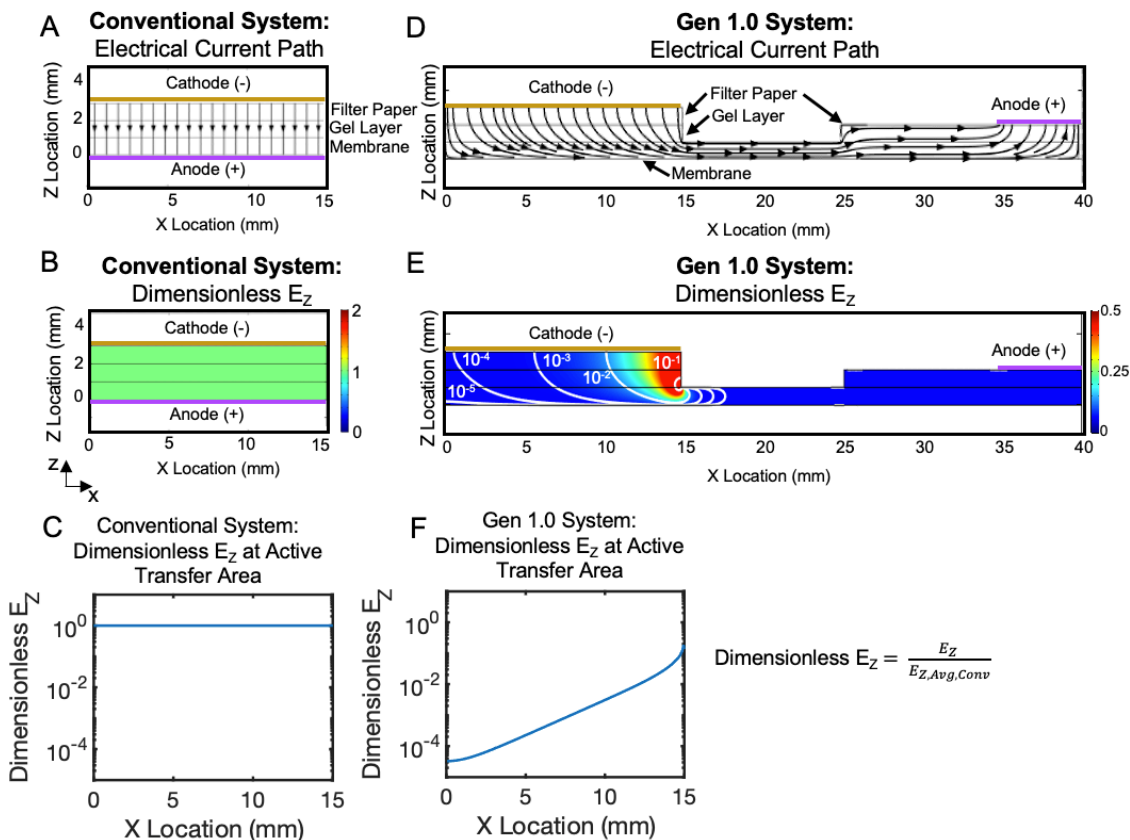
Figure 1: In the conventional electrotransfer system, (A) the electrical current path is uniform and parallel to the Z-axis and (B) the electric field magnitude in Z, E_Z, is uniform throughout the gel. (C) The E_Z in the conventional system at the active transfer area is thus also uniform in X. In the Gen 1.0 electrotransfer system, (D) the electrical current path is non-uniform in Z and includes components in X and Z and (E) the E_Z is non-uniform throughout the gel. (F) The E_Z in the Gen 1.0 system at the active transfer area is non-uniform in X and increases with proximity to the anode (+).

to the Z-axis throughout the entire electrotransfer system (Figure 1A), and thus the magnitude of electric field that contributes to protein electrotransfer (parallel to the Z-axis, E_Z; V/cm) is uniform throughout the entire electrotransfer system (Figure 1B). To specifically evaluate the magnitude of E_Z in the active protein electrotransfer region in relation to the average magnitude of E_Z in the

entire electrotransfer system, we plotted a dimensionless E_Z at the gel-membrane interface as a function of X-location (Figure 1C). The dimensionless E_Z is determined by dividing the magnitude of the X-location specific E_Z by the average magnitude of E_Z in the entire electrotransfer system, facilitating direct comparison of E_Z at the active protein electrotransfer region to the average E_Z in the system. We observe dimensionless $E_Z = 1$ at all X-locations, indicating uniform E_Z magnitude that is additionally equivalent to the average E_Z magnitude in the electrotransfer system.

Application of our modeling analysis to the Gen 1.0 device shows that the electrical current path is non-uniform throughout the electrotransfer system and includes components in X and Z dimensions (Figure 1D). We additionally find that the E_Z magnitude is non-uniform, particularly at the gel-membrane interface (Figure 1E). To compare the E_Z magnitude in the Gen 1.0 device to the average E_Z in the conventional system, we non-dimensionalized the E_Z at the gel-membrane interface in the Gen 1.0 device by dividing E_Z by the average E_Z in the conventional system. The dimensionless E_Z is plotted as a function of X-location, showing that the E_Z magnitude is 10^{-1}-10^{-4} lower than in conventional electrotransfer (Figure 1F).

Investigation of EZ in Conventional and Gen 1.0 Electrotransfer Systems by Modeling Analysis

Using the results of our electric field modeling analysis, we sought to develop a modeling framework to approximate protein migration velocity (and thus electrotransfer transfer times) as functions of gel density, protein size, and E_Z. Protein electromigration velocity (v; cm/s) is linearly proportional to the electric field strength and the electrophoretic mobility (μ; cm^2/Vs)

$$v = \mu E$$

The Ferguson relation describes protein electromigration in polyacrylamide gel electrophoresis as

$$\mu = 10^{-K_r * \%T}$$

where K_r is the retardation coefficient, and %T is the total acrylamide concentration[1]. K_r is related to the size of the protein and the sieving quality of the separation matrix, and follows a linear relationship with molecular weight for most proteins[2,3]

$$K_r = A + B * MW$$

where A and B are empirically determined constants that are unique to a particular system. Ultimately, a governing equation for protein velocity that incorporates gel density, protein molecular weight, and electric field strength can be described as

$$\mu = 10^{-(A+B*MW)*\%T}$$
$$v = E_Z * 10^{-(A+B*MW)*\%T}$$

As approximations of A and B in our system, we accepted values determined in previous studies using similar polyacrylamide gel electrophoresis systems (A = -0.001, B = 2.2*10^{-3})[4]. To describe protein electromigration velocity in our electrotransfer systems, we can input E_Z (from Figure 1 modeling analysis) and the range of MW and %T of interest.

We demonstrate this modeling framework as a tool to relate μ to any combination of MW and %T by plotting the μ for protein targets with MW ranging from 5 to 200 kDa in distinct, uniform %T gels from 4 to 14%T (Figure 2A). For protein targets that have undergone electrophoretic separations in a %T gradient gel, protein MW can be spatially encoded across the gradient gel such that a high to low MW distribution overlays a low to high %T gradient; large MW proteins exist in low %T gel regions, and small MW proteins exist in high %T gel regions. To model protein
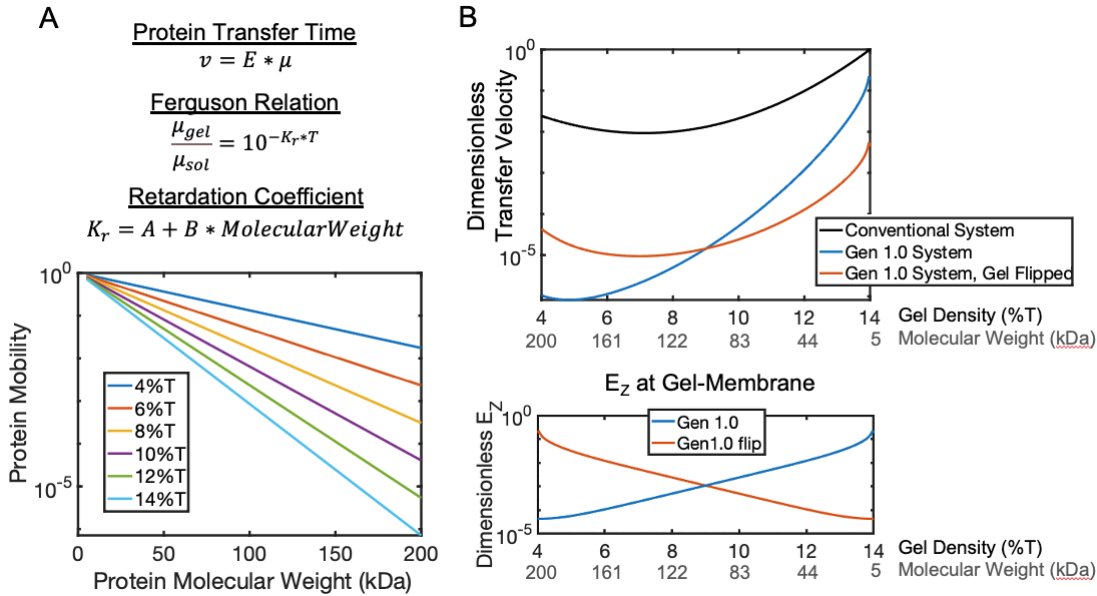
Figure 2: (A) Protein transfer time depends on the electric field and protein electrophoretic mobility. Electrophoretic mobility depends on the gel pore size, determined by %T, and the molecule's retardation coefficient which, in a denatured system, scales linearly with protein molecular weight. (B) Taking all these factors into account and modeling the dimensionless transfer time, the transfer time of the largest protein in the offset system (blue line) is 10^{-5} slower than the convectional vertical electrotransfer due to the lower electric field in that region of the gel (blue line). Reversing the orientation such that the higher molecular weight proteins are in the region with highest electric field, in the offset system (orange line), reduces the transfer time, but it is still 10^2 slower transfer than conventional system.

transfer velocity resulting from this combination of non-uniform spatial distributions of MW and %T, we plot protein transfer velocity as a function of a %T gradient gel (4 to 14%T, linearly increasing) and size separated protein MW distribution (200 to 5 kDa, linearly decreasing), considering the electric field profiles in a conventional electrotransfer system, the Gen 1.0 device, and a Gen 1.0 device with the gel orientation flipped with respect to the electrode arrangement (Figure 2B, top). Electric field profiles in the Gen 1.0 and Gen 1.0 with flipped gel orientation are shown in Figure 2B, bottom, with respect to the %T and MW distributions. In the conventional electrotransfer system, the electric field is spatially uniform. The transfer velocities are all non-dimensionalized by dividing all the transfer velocities by the fastest moving analyte (a 5 kDa protein in a 14%T gel under the electric field in the conventional electrotransfer system). We thus

developed an analytical model to approximate protein transfer velocity as functions of gel %T, protein MW and applied E_Z. We applied this framework to determine transfer velocities of size separated proteins in a gradient gel with three different electrotransfer systems; a conventional system, the Gen 1.0 device, and a Gen 1.0 device with a flipped gel orientation. In the Gen 1.0 system, protein transfer velocities were 10^{-1} to 10^{-4} slower than in the conventional system. In the Gen 1.0 system with the gel orientation flipped, protein transfer velocities were 10^{-1} to 10^{-3} slower than in the conventional system. Our modeling analysis indicates that the Gen 1.0 device is a tool to shape non-uniform spatial distributions of E_Z in an electrotransfer system, but adversely impacts protein electrotransfer velocities compared to conventional electrotransfer systems.

Experimental Investigation of Protein Transfer Efficiency using Offset Electrode Configurations

To experimentally validate the simulated models, we tested the offset transfer using standard 1mm-thick gels with standard semi-dry transfer buffer (Figure 3A). To improve transfer, we tested 1) increasing voltage to increase E-field and 2) reversing the gel orientation during electrotransfer to place larger molecular weight proteins closer to anode where there is higher magnitude E-field (Figure 3B). Based on the linear relationship between electrophoretic mobility and electric field strength, we hypothesize that increasing the electric field will improve transfer of larger MW proteins in the offset transfer geometry compared to the original offset set up

To test the impact of gel orientation during transfer we ran two samples of iBright Protein Standard ladder via conventional PAGE using a 14%T Tris-glycine gel and 1x Tris-Glycine run buffer. After the separation, the gel was then cut in half, and one separation lane was reversed to have opposite orientation to the other lane. During the offset transfer, there was one lane with the original orientation with larger molecular weight proteins closer to the cathode (weaker E-field) and one lane with reverse orientation with larger molecular weight proteins closer to the anode (stronger E-field). Both gels were transferred to the same nitrocellulose membrane simultaneously using the offset electrode configuration transfer system. Pierce™ 1-Step Transfer Buffer was used for the transfer step. The nitrocellulose membrane was then imaged to compare protein transfer and signal of the two orientations. All gels were run using the same settings for the separation. We tested the reverse orientation at three different voltages during electrotransfer to determine if the
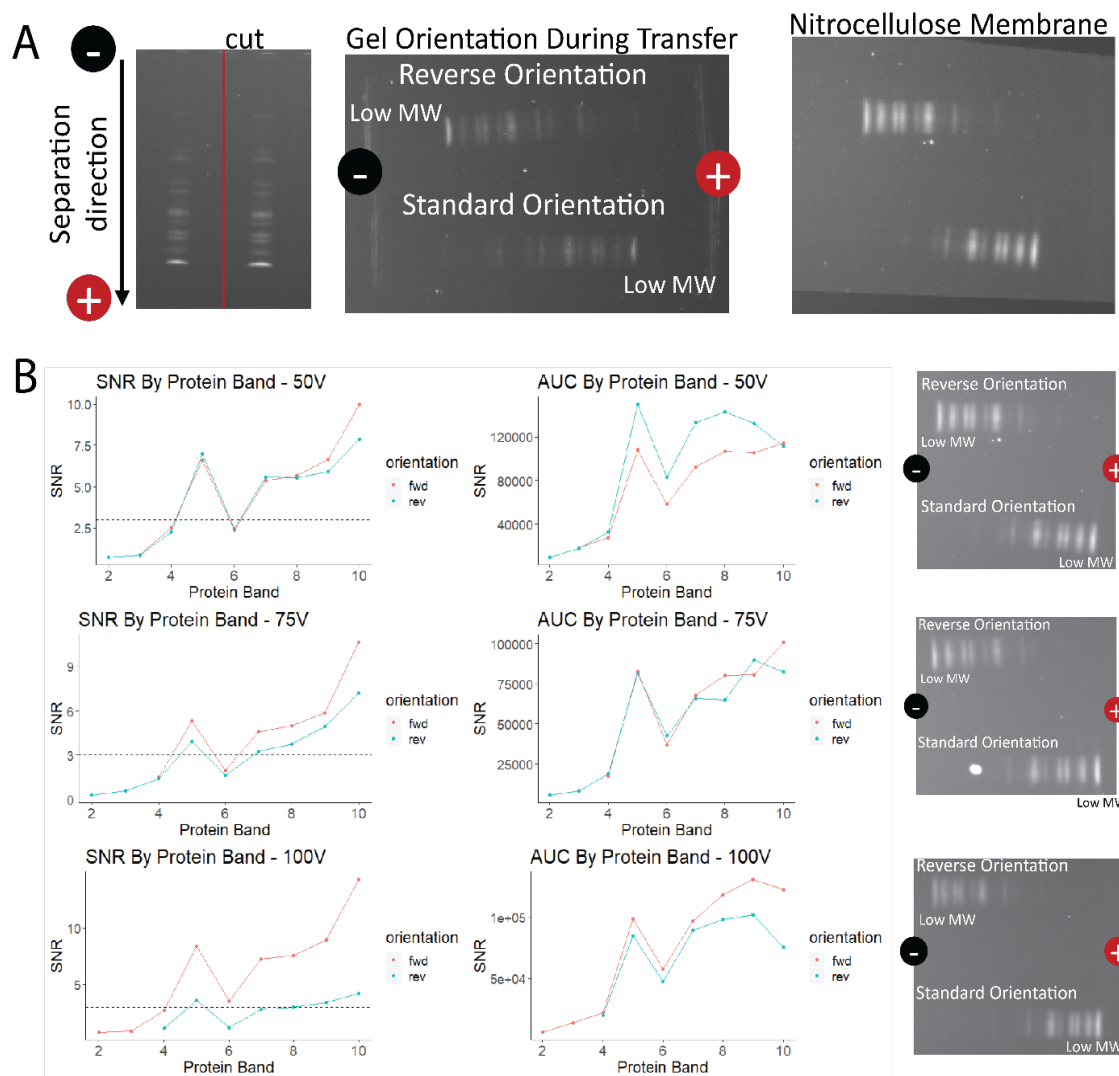
Figure 3: (A) Experimental schematic: Protein ladder was run using conventional PAGE using a 14%T Tris-glycine gel. Offset transfer was performed with one lane with smaller MW proteins closer to the anode where the E-field is highest. The other lane had the reverse orientation such that the larger MW proteins were in the region of higher E-field. (B) SNR, AUC and fluorescence image of detected protein bands transferred to the nitrocellulose membrane for each voltage setting (50V, 75V, and 100V) and both gel orientations.

combined effect of reverse orientation and higher electric fields would improve transfer. We tested three different voltages: 50V, 75V and 100V and electrodes were spaced 5 cm apart for all 3 conditions for average electric fields of 10 V/cm, 15V/cm and 20 V/cm. The nitrocellulose membranes post-transfer were imaged using the iBright using the same imaging settings (exposure time and optical zoom) and area under the curve and SNR of the proteins bands was quantified (Appendix S1). For analysis, protein band 10 refers to the smallest MW protein, regardless of orientation.

We observed that regardless of orientation, only the lower molecular weight proteins were eluted from the gel and transferred out of the gel to the nitrocellulose membrane. This aligns with the predicted results from the model indicating that the transfer velocity of smaller molecular weight species will always be higher than larger molecular weight species (Figure 2B). Furthermore, the relatively small increases in electric field, compared to the orders of magnitude difference in the models, did not substantially improve the detectable (SNR >3) transfer of high molecular weight proteins. We note that faint bands corresponding to larger molecular weight proteins were visible by eye in the reverse orientation compared to the standard orientation, but none of the additional bands had an SNR >3. This further verifies the modeling that the z-direction mobility of the high MW proteins is not high enough to leave the gel, even in the highest E-fields in the offset system. We also note that the higher voltage condition (100V), did not result in increased dispersion of smaller molecular weight bands as previously observed. there was not dispersion of the lower MW that had been previously observed. We hypothesize that the lower current in the current run (6-9 mA) compared to previous run (30-40 mA). To reduce variation, it will be important to standardize the protocol (e.g. cutting the wicks all to the same size, loading the same volume of buffer, cutting the NC membranes and gels to the same size).

Experimental Investigation of Protein Transfer Efficiency in Thin-Gel Assemblies
We next investigated if reducing gel thickness reduces transfer such that offset transfer of large molecular weight protein is feasible (Figure 4). We compared transfer of protein separation from a standard 1 mm thick gel and vertical semi-dry transfer (Figure 4A) to a thin-gel separation and offset electrode configuration transfer (Figure 4B). Protein transfer time scales linearly with distance and inversely with electric field. Based on the results of the models, the Z-direction electric field in the offset system varies by $>10^2$-fold, however we can only reduce the distance (thickness of the gel) by a factor of 10 (from 1mm thick gels to 100 μm). To perform electrotransfer of protein using thin gels, we first fabricated thin (~125 μm) 8%T fsPAGE gels on top of NetFix (60 μm) to provide mechanical support for handling the gel during transfer. The total thickness of the thin gel was ~185 μm (Appendix S2). Purified BSA protein labeled with Alexa Fluor 555 was run using horizontal fsPAGE (Appendix S2). After running the separation, the blot transfer was run using the offset electrode configuration to transfer both the BSA monomer and dimer to a nitrocellulose membrane. The offset transfer was run for 3 minutes at 75V, with electrodes spaced 5 cm apart (15 V/cm).

We observed that the smaller BSA monomer (66 kDa) was successfully transferred to the nitrocellulose membrane, but the larger BSA dimer (132 kDa) was not. The thin gels do not appear to improve transfer of large molecular weight proteins out of the gel in the offset electrode configuration as the single order of magnitude reduction in transfer distance does not make up for the several orders of magnitude difference in transfer velocity between larger and smaller molecular weight species. Additionally, the post-transfer protein band of the BSA monomer on the nitrocellulose membrane had a greater band width than the protein band in-gel potentially indicating that protein travelled down and laterally from the gel to the membrane.
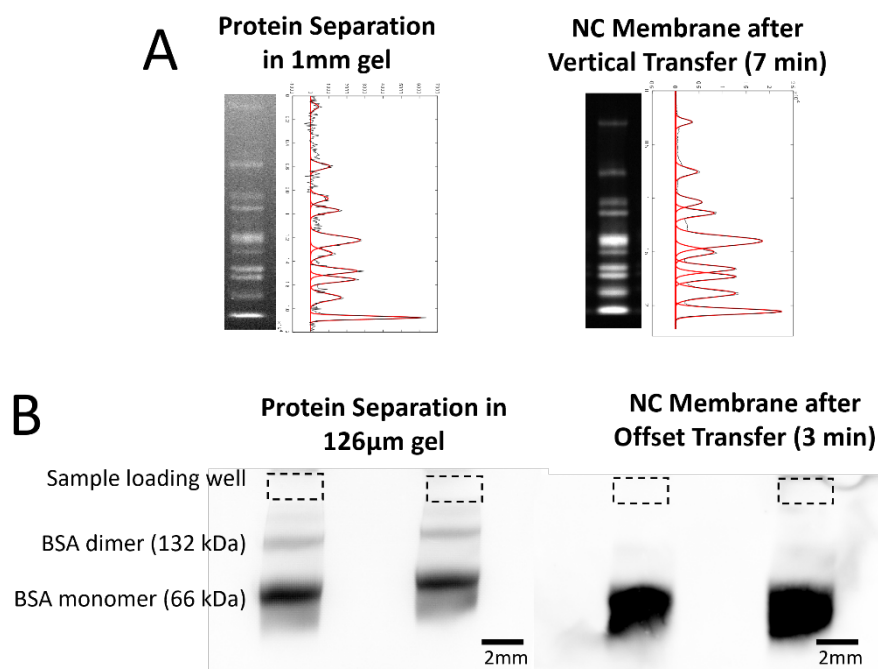
Figure 4: (A, Left) Protein ladder separation in 1mm gel prior to transfer using conventional vertical PAGE tank system. (A, Right) Nitrocellulose membrane post-transfer using standard vertical semi-dry transfer system. (B, Left) Purified protein (BSA monomer and dimer) in gel following fsPAGE horizontal separation using a ~125 μm thick gel. (B, Right) Nitrocellulose membrane post-transfer using offset electrode configuration

Investigation of E_Z in Gen 1.1 Electrotransfer System by Modeling Analysis

To increase E_Z magnitude and reduce non-uniformity of protein electrotransfer times compared to the Gen 1.0 device, we sought to investigate new electrode configurations for reduced voltage loss across active transfer area (gel-membrane boundary). We first sought to increase E_Z magnitude by reducing the electrode spacing in the Gen 1.0 system (Gen 1.1 system; Figure 5 A,B). By reducing the electrode spacing from 20 mm (Gen 1.0) to 1 mm (Gen 1.1), we observe a 10^1 increase in E_Z magnitude (Figure 5 C). While this validates our assumptions of the design rule that minimizing electrode spacing can maximize E_Z magnitude, E_Z min the Gen 1.1 system is still 10^{-1} to 10^{-3} lower than in the conventional electrotransfer system.
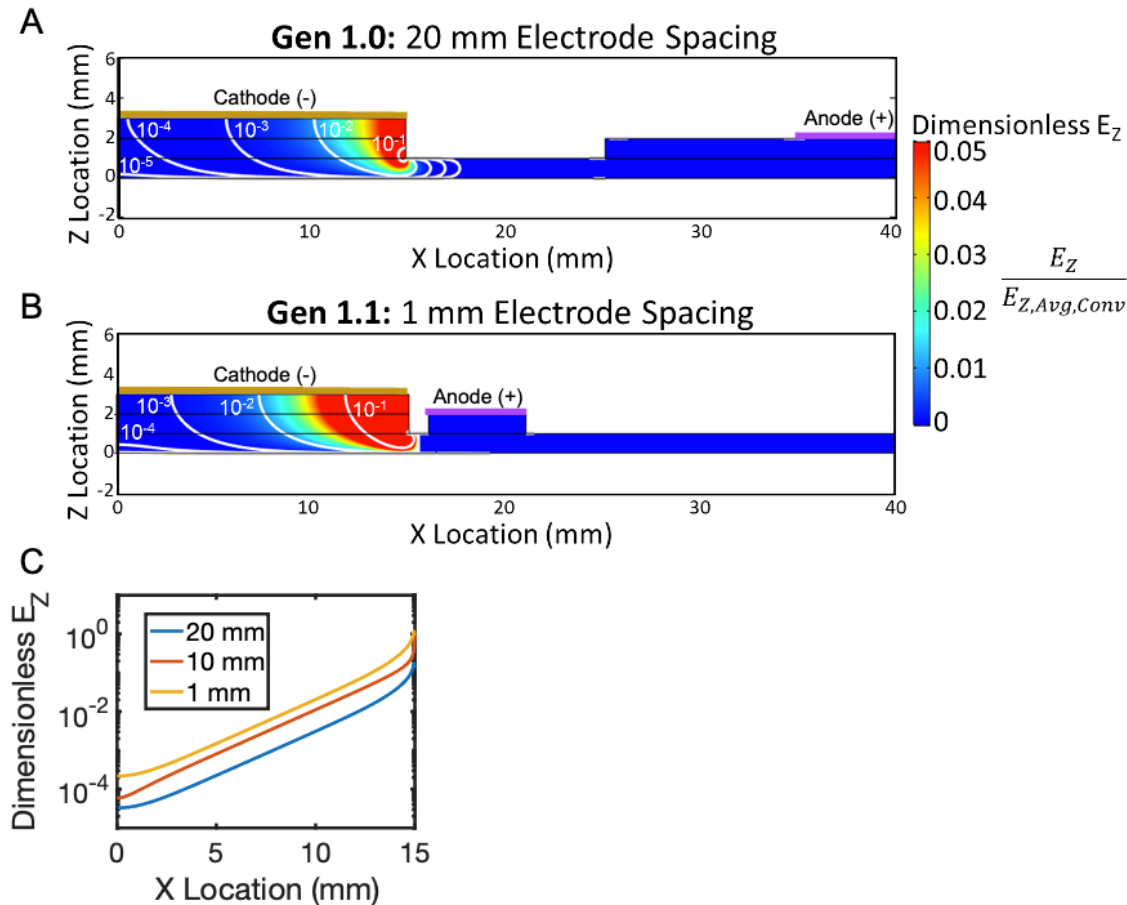
Figure 5: (A,B) The Gen 1.1 electrotransfer system aims to increase E_Z magnitude at the active transfer area by reducing spacing between the cathode and anode from 20 mm in the Gen 1.0 system to 1mm in the Gen 1.1 system. (C) E_Z magnitude in the active transfer area is an order of magnitude larger in the Gen 1.1 system than Gen 1.0 system.

Investigation of E_Z in Redesigned Gen 2.0 and 2.1 Electrotransfer Systems by Modeling Analysis

We next sought to increase E_Z over the active transfer area by using multiple anodes as a method to reduce electrode spacing at both ends of the cathode (Gen 2.0 system; Figure 6 A,B). In this Gen 2.0 assembly, we use learnings from the Gen 1.1 system to inform the Gen 2.0 electrode separation design and include 1 mm of spacing between cathode edges and each anode. We observe the E_Z magnitude at each edge of the cathode in the Gen 2.0 design to be 10^{-1} lower than in the conventional electrotransfer system (Figure 6C). This represents an improvement over the Gen 1.1 system, where E_Z at the edges of the cathode were 10^{-1} (proximal to lone anode) and 10^{-1} (distal to lone anode) lower than in the conventional electrotransfer system. Additionally, we observe that in the Gen 2.0 system, the E_Z minimum is 10^{-2} lower than the conventional system (instead of 10^{-3} in Gen 1.1) and occurs in the center of the gel.

114
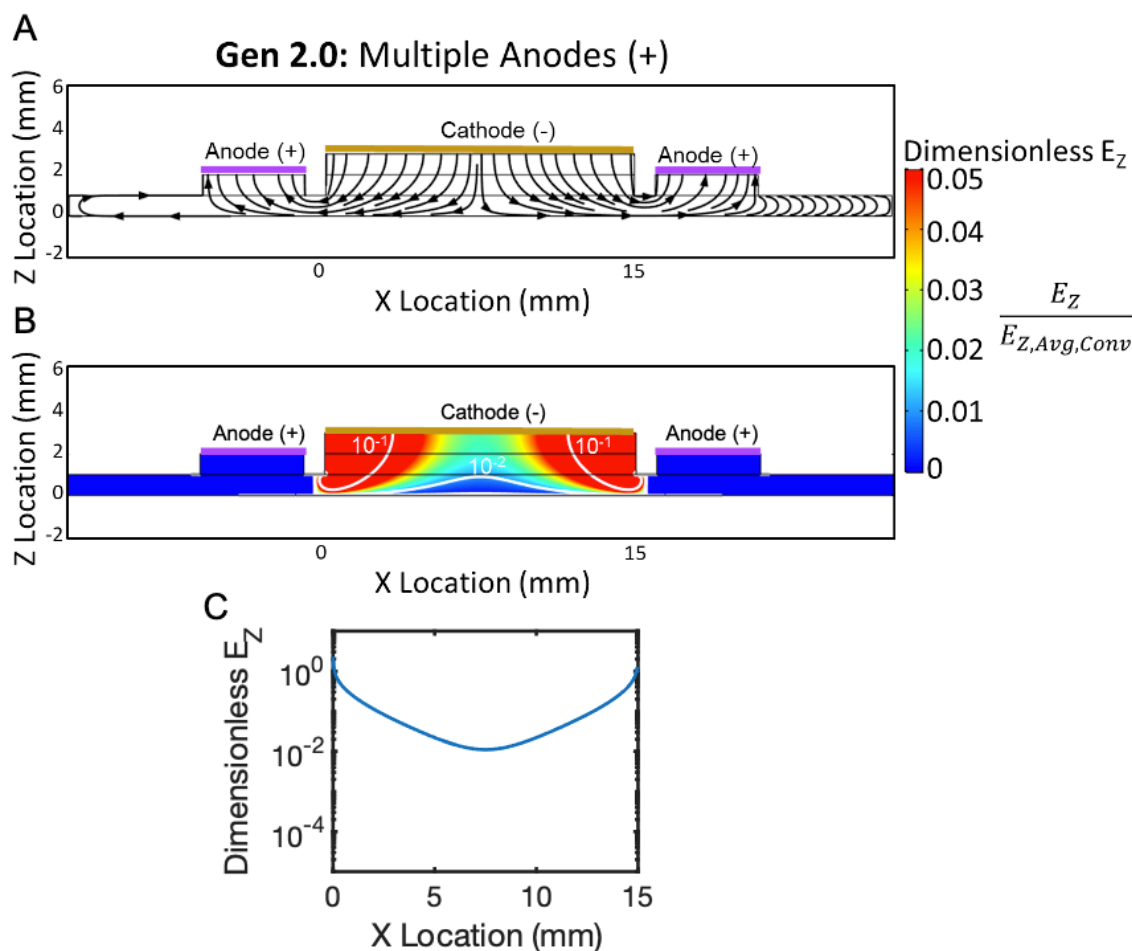
Figure 6: (A,B) The Gen 2.0 system aims to increase E_Z magnitude at the active transfer area by including multiple anodes, one on either side of the cathode. (C) E_Z magnitude at each edge of the active transfer area is has a value of 10^{-1}, but the gel center has a minimum E_Z value of 10^{-2}.

Lastly, we sought to increase E_Z over the active transfer area by using a wire electrode mesh placed directly below the electrotransfer assembly (Gen 2.1 system; Figure 7 A,B). Use of a wire electrode mesh (as opposed to an electrode plate) would permit membrane visualization as well as access of fluid reagents to the membrane (critical for immunoprobing proteins immobilized in membrane) without disassembling the electrode arrangement. Using a wire electrode mesh with 1 mm diameter wires spaced 5 mm apart, we observe minimum E_Z values 10^{-1} lower than in conventional systems (Figure 7C). The E_Z minimums occur at the midpoint between each electrode wire. Maximum E_Z values occur directly above each electrode wire and are 10^0, indicating no difference between the Gen 2.1 system and the conventional electrotransfer systems at these locations.
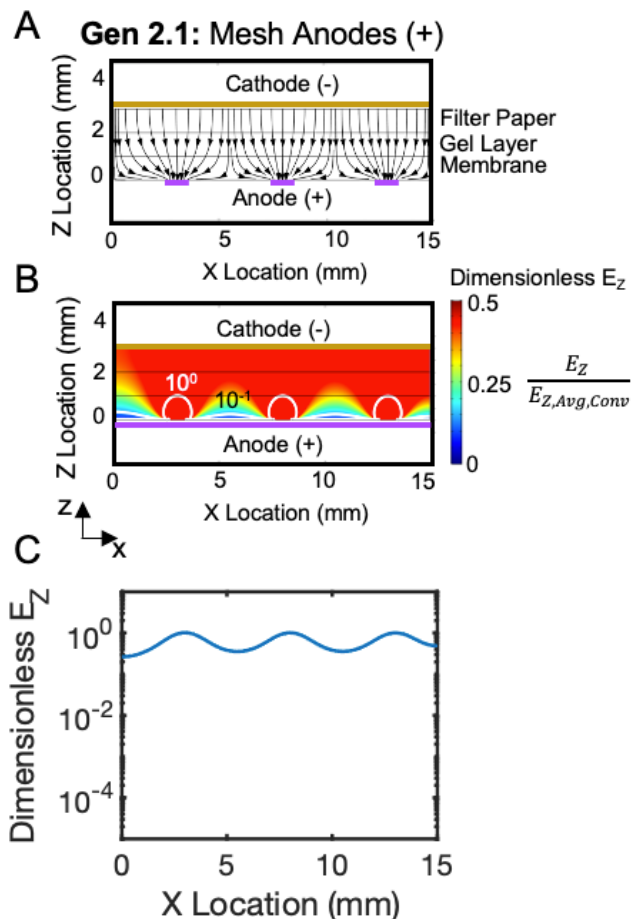
Figure 7: (A,B) The Gen 2.1 system aims to increase E_Z magnitude at the active transfer area by including a mesh of wire electrodes directly below the capture membrane. (C) E_Z magnitude is at minimums of 10^{-1} between each wire electrode, and E_Z maximums of 10^0 directly above each wire.

From our modeling analysis, we observe that the E_Z magnitude is 10^{-1} to 10^{-4} lower at the active transfer area when using offset electrode assemblies as compared to the conventional electrotransfer system. Reduced magnitude of E_Z adversely impacts protein transfer time, as protein migration velocity is linearly related to E_Z. Thus, 10^{-1}-10^{-4} lower E_Z magnitude results in 10^1-10^4 longer electrotransfer times. The use of a wire mesh electrode introduces maximum E_Z values of 10^0, and minimum E_Z values of 10^{-1}. Further investigation of the Gen 2.1 system would be required to determine its compatibility with protein electrotransfer, as limited buffer capacity and introduction of gas products via electrolysis may present additional challenges to protein migration. The results of the E_Z magnitudes at the active transfer area for all electrotransfer systems are summarized for direct visual comparison in Figure 8.
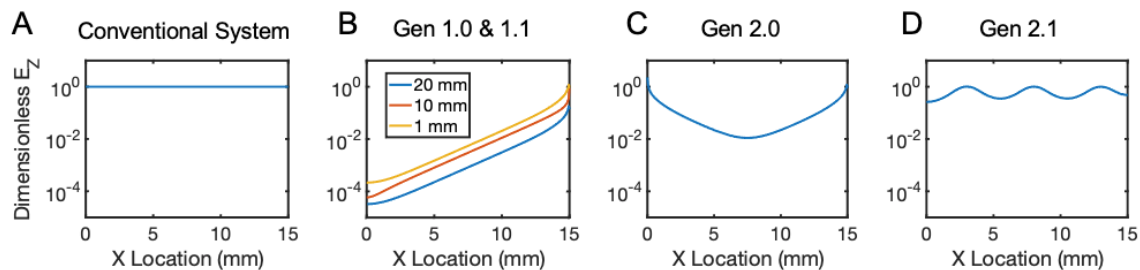
Figure 8: Comparison of the E_Z magnitude at the active transfer area in all electrotransfer system: (A) conventional system, (B) Gen 1.0 and Gen 1.1, (C) Gen 2.0, and (D) Gen 2.1.
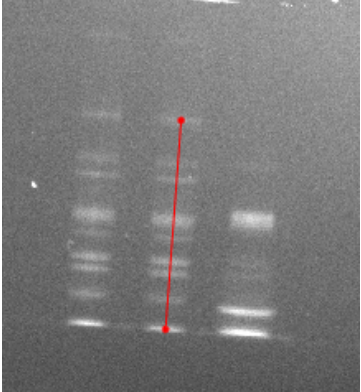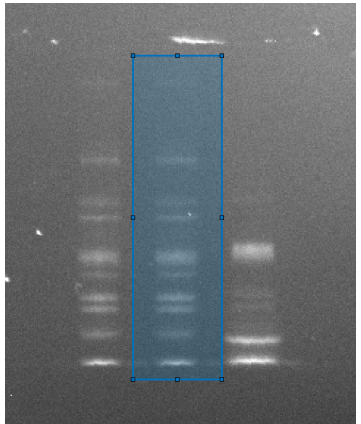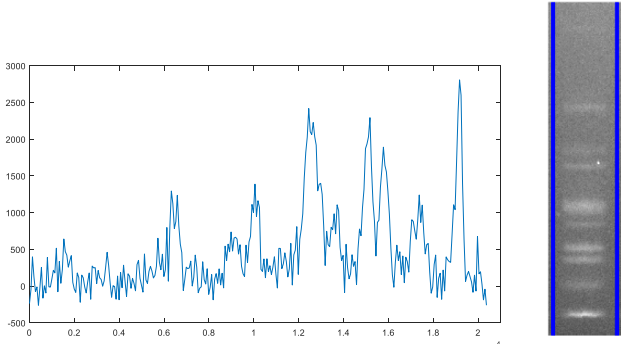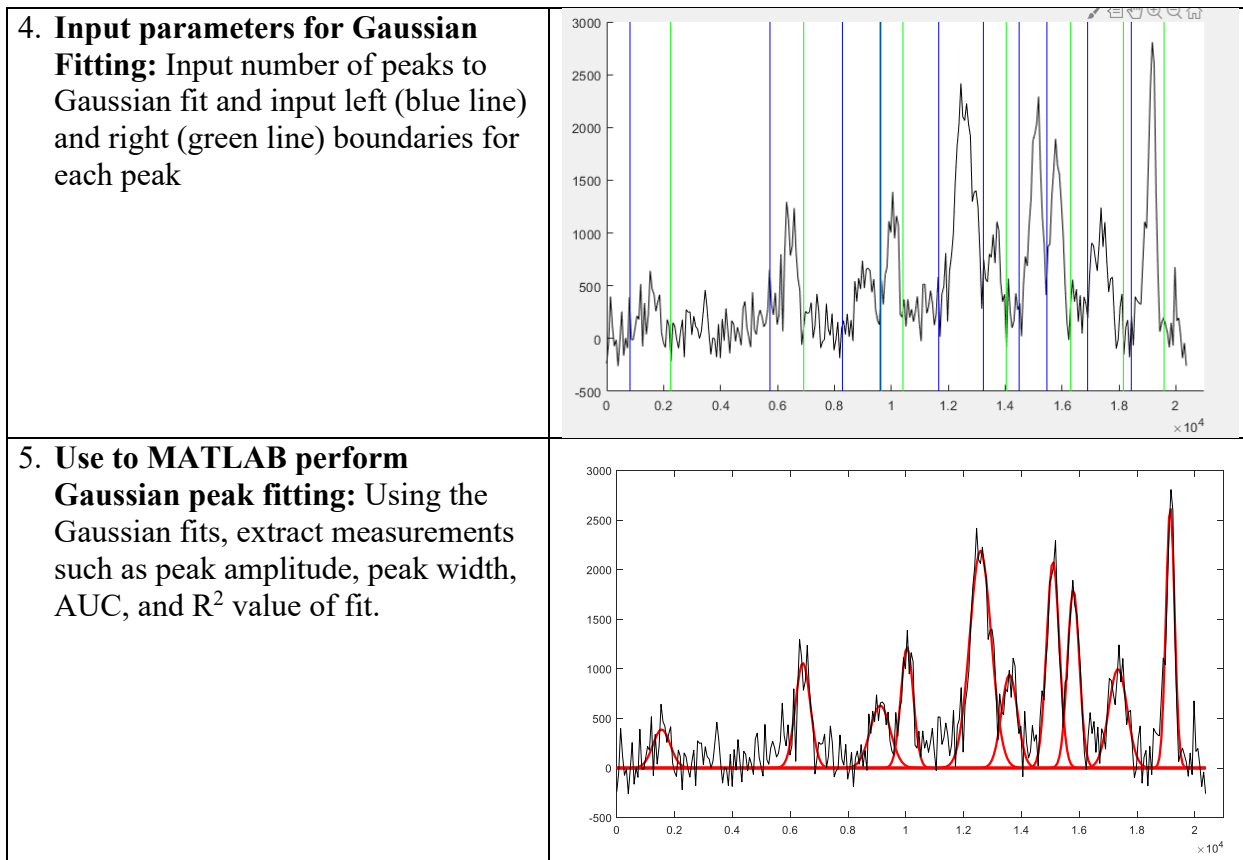
5.3.   Conclusion & Next Steps

Here, we investigated an offset electrode configuration as a system for gel to membrane protein electrotransfer. Our investigation involved a modeling analysis of the electric field magnitude and electrical current path resulting from electrode placement, and an experimental investigation of protein electrotransfer transfer using the offset electrode arrangements with conventional 1mm and thin (100μm) gels. Our modeling analysis indicates that the electric field magnitude is 10^{-1} to 10^{-3} lower than in conventional electrotransfer systems, presenting a challenge to electrotransfer of large molecular weight proteins in the offset electrode system. The results of the modeling analysis are supported by our experimental investigation of protein electrotransfer, as we observed poor electrotransfer of large molecular weight species in the offset electrotransfer system (compared to conventional electrotransfer system) regardless of gel thickness. To mitigate voltage loss across active electrotransfer areas, we investigated the design of Gen 2.0 electrotransfer systems with alternative electrode configurations via a modeling analysis of the electric field magnitude and electrical current path in the Gen 2.0 systems.

Our proposed next steps for this study involve continuing the investigation of Gen 2.0 electrotransfer systems beyond the initial modeling analysis. Specifically, we propose (i) investigation of the physical assembly of proposed Gen 2.0 electrotransfer systems and (ii) experimental investigation of gel to membrane protein electrotransfer in Gen 2.0 electrotransfer systems. We propose that the experimental investigation of gel to membrane protein electrotransfer in Gen 2.0 systems would be performed in thin (~100 μm thick) gels using NetFix as a gel support material, and would include an analysis of protein dispersion during electrotransfer. Additional challenges to using thin gel systems include limited buffering capacity of the electrotransfer system. Conception of Gen 2.0 systems with sufficient buffering capacity during minimum electrotransfer time required for protein elution would thus be an additional next step.

5.4. Appendix

S1 MATLAB Image analysis script to quantify AUC and SNR from gels and nitrocellulose membranes imaged on the iBirght

|	
1. **Rotate and Align the Image:** Import raw TIFF image into MATLAB. Select the middle of band near the top and bottom to draw a reference line to rotate the image to the straight.	
2. **Select ROI:** Manually draw box around lane to analyze.	
3. **Generate Intensity Profile:** Background subtraction performed using a gutter region on the left and right (blue lines). Then an average intensity profile is generated for peak fitting	

4. **Input parameters for Gaussian Fitting:** Input number of peaks to Gaussian fit and input left (blue line) and right (green line) boundaries for each peak	
5. **Use to MATLAB perform Gaussian peak fitting:** Using the Gaussian fits, extract measurements such as peak amplitude, peak width, AUC, and R^2 value of fit.	

S2 NetFix Gel Fabrication and fsPAGE protocol (adapted from T. A. Duncombe and A. E. Herr, Lab on a Chip, 2013)

To perform offset transfer with thin gels, we fabricated thin gels with NetFix to perform fsPAGE separation and then offset transfer. The fsPAGE separation system[5] typically utilizes thin gels (100-200 μm tall) fabricated on a glass slide to perform horizontal protein separations. Here, we have adapted the system, fabricating thin gels on NetFix to run the horizontal protein separation.

NetFix Thin Gel Fabrication process:

First to adhere the NetFix to the glass slide, a ~20 μL drop of gel precursor solution (before adding APS and TEMED) was pipetted onto the glass slide and a Western Blot Roller was used to roll across the NetFix to adhere the NetFix to the glass slide and remove any bubbles. TEMED and APS were added to the remaining gel precursor before it was pipetted onto the SU-8 wafer mold. Then the glass slide with NetFix was placed on top of the wafer, with the NetFix side face down, to sandwich the gel precursor in between the wafer and glass slide (Appendix Fig 1). The NetFix
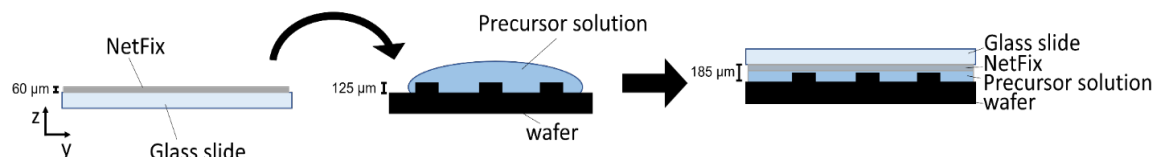
Appendix Figure 1: Schematic of step-by-step NetFix gel fabrication.

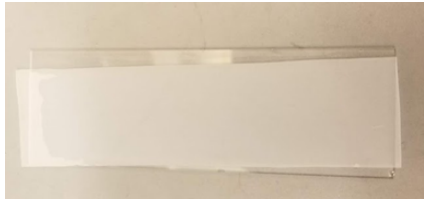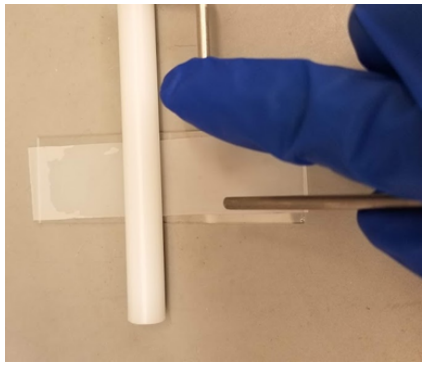sits on top of the SU-8 wafer posts that form the sample wells in the gel. NetFix add about 60 μm
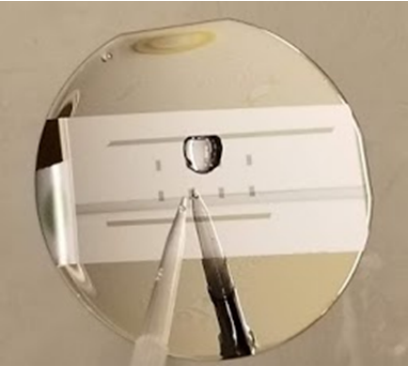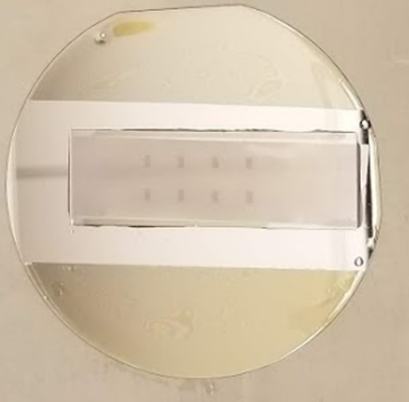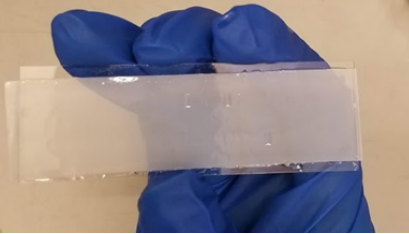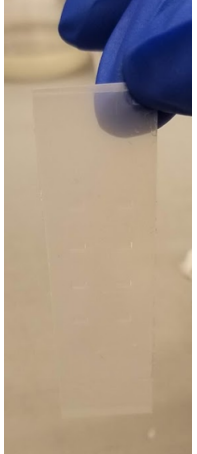
119

to the total gel thickness, which is primarily determined by the height of the SU-8 wafer features. Gels were polymerized for 20 minutes before lifting off of the wafer. With the NetFix support, gels can be removed from the glass slide to be free standing and easily handled without breaking. Gels were incubated in fsPAGE run buffer solution until sample loading and electrophoresis.
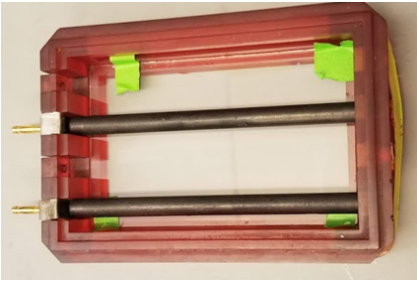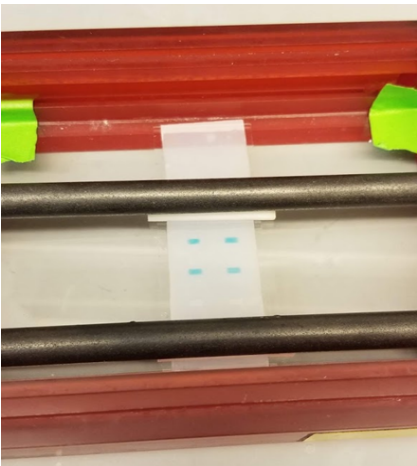
For standard fsPAGE, the run buffer is a 1x Tris-Glycine solution with 10% glycerol and 0.5% Triton X-100. A purified protein solution containing 3μM BSA-AF555 was prepared in the fsPAGE run buffer.

To perform the fsPAGE separation, the NetFix gel was gently dried with Kimwipe to remove excess buffer before being placed on a dry glass slide which provided a uniform flat surface. Serva electrode wicks were cut in half and pre-soaked in fsPAGE run buffer before being attached to carbon electrodes using rubber bands. The wicks were gently blotted on a Kimwipe to remove excess buffer before the carbon electrodes (with wicks facing downward toward the gel surface) were placed on the surface of the gel, 3 cm apart. Then 0.3-0.5 μL of protein solution was loaded into each well. The separation was run for 3 min at 300V (100V/cm) and protein migrated laterally through the gel. After separation, the electrophoresis chamber was disassembled and the NetFix gel was removed from the glass slide and transferred to the offset electrode configuration transfer system.

Detailed fsPAGE protocol

2. Place NetFix on top of a drop of gel precursor on a clean unsilanized glass slide	
3. Use a Western blot roller to remove any air bubbles from the NetFix membrane and gel precursor solution	

4. Add TEMED and APS to remaining gel precursor and pipette ~250 µL on SU-8 wafer with posts. Be sure to treat SU-8 wafer with gel slick before gel fabrication so prevent gel from sticking to wafer.	
5. Place NetFix slide on top of gel precursor to sandwich (NetFix side facing the wafer). Let gel polymerize for ~15-20 minutes	
6. After gel polymerization, lift slide with polymerized gel off of wafer	
7. Gently peel the NetFix-gel off of the glass slide	

8. Place NetFix-gel on a glass slide and in the fsPAGE electrophoresis chamber. Place wicks soaked in run buffer on the surface of the gel	\n\nfsPAGE electrophoresis chamber\n\n
9. Place electrodes on top of the wicks and then fill the wells with 0.5 µL of protein sample	
10. Connect electrode to power source and run separation	

5.5. References

(1) Ferguson, K. A. Starch-Gel Electrophoresis-Applications to the Classification of Pituitary Proteins and Polypeptides. *Metabolism* **1964**, *13* (10), 985–1002.

(2) Rodbard, D.; Chrambach, A. Unified Theory for Gel Electrophoresis and Gel Filtration. *Proc. Natl. Acad. Sci.* **1970**, *65* (4), 970–977. https://doi.org/10.1073/pnas.65.4.970.

(3) Morris, C. J. 0 R.; Morris, P. Molecular-Sieve Chromatography and Electrophoresis in Polyacrylamide Gels. *Biochem. J* **1971**, *124*, 517–528.

(4) Herr, A. E.; Singh, A. K. Photopolymerized Cross-Linked Polycrylamide Gels for on-Chip Protein Sizing. *Anal. Chem.* **2004**, *76* (16), 4727–4733. https://doi.org/10.1021/ac049686u.

(5) Duncombe, T. A.; Herr, A. E. Photopatterned Free-Standing Polyacrylamide Gels for Microfluidic Protein Electrophoresis. *Lab Chip* **2013**, *13* (11), 2115–2123. https://doi.org/10.1039/c3lc50269d.

6 Conclusions

In this dissertation, we aimed to contribute to the advancement of proteoform-specific detection assays, with the broader goal of improving our understanding of cell-state in healthy and disease conditions. In this effort, we identified a need to improve the analytical sensitivity of proteoform detection in open hydrogel electrophoretic cytometry assays, and we thus designed novel immunoprobing strategies and immunoassay formats to meet this need.

Specifically, in chapter 2, to improve analytical detection sensitivity and reduce overall immunoprobing duration in mm-scale free-standing hydrogel immunoassays, we develop an electrotransfer probing systems for such assays. In chapter 3, to improve throughput of single-cell electrophoretic cytometry assays, we design 3D projection electrophoresis for single-cell immunoblotting. In chapter 4, to improve the total mass of probe delivery and expedite the rate of probe delivery to microgel electrophoretic cytometry immunoassays, we introduce a microgel chip designed to overcome size-exclusion partitioning through electrotransfer probe loading to microgel chips. In chapter 5, we reengineer gel-membrane electrotransfer systems in conventional western blotting to (i) prevent over transferring smaller-sized species, retaining smaller proteins laterally on the blotting membrane as larger proteins elute from the gel and (ii) simplify the conventional western blot workflow by minimizing user handling.

Overall, we see the advancement of assays capable of proteoform-specific measurements at the single-cell level as leading to an improved understanding of the role that proteoforms play in biology and to better inform therapeutic interventions in disease.

Appendix: Towards an Assay for Dual Secreted Protein and Intracellular Proteoform Measurement from Single Cells

A.1   Introduction

Cellular protein secretions play essential roles in many biological processes, including in diseases like cancer through induced tumor formation, metastasis, and other processes.[1,2] These cellular secretion profiles can express tremendous heterogeneity at the single-cell level, and quantitation of single-cell secreted proteins is an important metric for understanding biological systems. The development of assays for single-cell secreted protein measurement has thus been an active field of research for several decades.

The earliest single-cell secretomic devices began with open designs that involved incubating a cell in media directly on a surface that is functionalized to capture secreted proteins.[3] In the late 80's Kendall and Hymer developed such a technique called cell blotting. Cell blotting involves pipetting cell suspension onto a transfer membrane (like PVDF), and incubating this in media while cells secrete hormones that are captured by the transfer membrane over several hours.[4] After washing and blocking steps, the membrane can be immunostained for single-cell secreted protein readouts. Other easy to use open devices build on the ELISA assays, and are called Elispot and FluoroSpot.[5] These techniques involve the same procedure of applying cell suspension to a functionalized capture surface, and use immunosandwich based protein detection, and either chemiluminescent or fluorescence-based readout.

While these open designs enable easy fabrication and reagent exchange, which is crucial in applications such as secretome response to drug treatment, a critical limitation of these open designs is that unconfined protein diffusive permits precious target secreted proteins to freely dilute in the surrounding incubation media. This is especially problematic given the variability in protein secretion rates, ranging from hormone secretion of ~10^5 molecules per second, to 10^4 antibody secretion from hybridoma cells, and down to 100 molecules or less per second for cytokines, which have been implicated in a range of processes including cell proliferation, disease progression, and others.[6,7,8] To place protein secretion rates in context of intracellular protein abundance, the mean cellular protein abundance is ~170,000 molecules, meaning that a 10 molecule/sec secretion rate requires >4.5 hours to reach mean intracellular protein abundance. Ultimately, while open assay designs are powerful tools for specific applications, they permit unimpeded diffusion-driven-dilution of secreted proteins, and in turn limit assay sensitivity.

To prevent this diffusion-driven dilution of secreted proteins, secretomic assays with closed microwell designs were developed to preserve protein concentration after secretion. In one example device from the Love Lab, cells are settled into a PDMS microwell array, and the array is sealed with a glass slide that has been patterned with capture antibodies through a technique known as microengraving.[7,8] This enclosed system is incubated on the scale of hours, typically dependent on target protein secretion rate, and then disassembled for captured secreted protein

readout by fluorescence immunosandwiching. This microengraving device has been applied to detect secreted antibodies from single-hybridoma cells (slide is patterned with secondary antibody, primary anti-body is captured, and fluorescently labelled antigen is introduced to complete the immunosandwich), as well as single-cell secreted antigens, as well as to detect proteins with secretion rates as low as 1-10 molecules per second. To perform highly multiplexed secretomic analyses, single-cell barcoding chips use enclosed microwells and finely patterned capture antibody "barcodes" to detect multiple secreted protein at once. Initial demonstrations of this chip facilitated 14-plexed secreted protein detection and have since improved to over 40 secreted targets from individual cells.[9,10]

However, while enclosed microwell designs have facilitated the development of several powerful single-cell secretomic assays, coupling these assays with downstream analyses for additional molecule classes often requires manual cell retrieval from microwells. Assessing cell state by multiple molecule types is of interest, as cellular protein secretion can be impacted by the intracellular proteome of that cell. Furthermore, the intracellular proteome of single cells can vary extensively, where even differences among protein isoforms can cause distinct cell function. While bulk studies on cell populations have shown us that these groups are related,[1] specific relationships between single cell isoform expression and protein secretion are currently yet to be investigated, as state-of-the-art technologies have not been adapted to make both these two measurements from single-cells.

To perform dual secreted protein and intracellular protein isoform measurements from single-cells, we introduce a proposal for an integrated device that facilitates on-chip detection of both molecular types. Our proposed chip builds on enclosed microengraving technologies for single-cell secreted protein measurement, but incubates cells in a microwell array patterned into polyacrylamide gel, instead of PDMS. After capture of secreted proteins by microengraving, intracellular protein isoforms can be interrogated by using the polyacrylamide gel matrix for single-cell Western blotting directly on chip. Towards our development of this assay, we first develop analytical modelling analyses to inform the lower limit of secreted protein detection from single cells in our proposed design. Next, we identify a model cell line and target secreted protein, and determine an approximation of the single-cell protein secretion rate of our model biological system. Then, we validated a method for antibody patterning on poly-L-lysine treated glass slides for subsequent use as microengraving capture surfaces. Finally, we apply the antibody patterned microengraving capture surfaces for preliminary detection experiments of secreted protein from bulk solution and single-cells. While these initial experiments prove unsuccessful, we identify potential causes of experimental failures and identify potential next experimental steps.

A.2   Results and Discussion

Proposed Device Theory of Operation.
The workflow for the proposed dual secreted protein and intracellular proteoform single-cell assay is described in Figure 1. The assay protocol combines the individual microengraving device for secreted protein detection and the microgel electrophoretic cytometry device for intracellular protein isoform detection. First, single-cells are isolated into a microwell array patterned into a polyacrylamide microgel chip. After cell settling, the microgel chip is covered with an antibody microengraved glass slide. Next, the enclosed chip is incubated to allow for single-cell secreted proteins to accumulate in individual microwells and bind to the protein capture antibodies on the microengraved glass slide. Then, the chip is disassembled by removing the microengraved glass slide from the microgel chip, such that the individual cells remain settled in microwells. Finally, the cells settled in the microwell array undergo the conventional scWB workflow, and the microengraved glass slide is interfaced with antibody probe solution for immunoassaying. Both the microengraved glass slide and the microgel chip are imaged by microarray scanner, and single-cell expression of intracellular isoforms and secreted proteins are made.
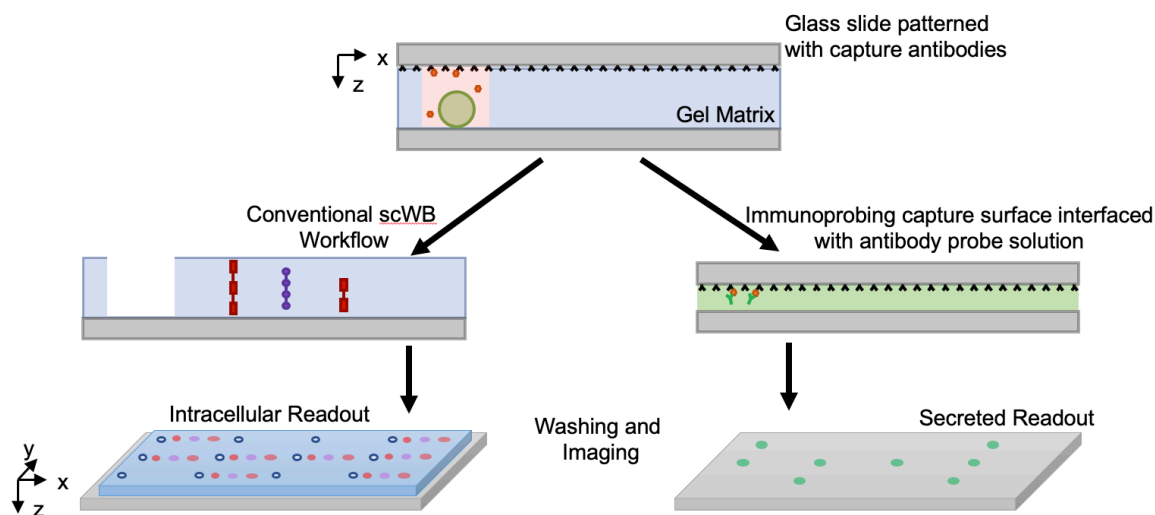

Figure 1. Schematic of the proposed workflow for an assay for dual secreted protein and intracellular isoform measurements from single-cells. The workflow combines aspects of microengraving tools and single-cell Western blotting assays. First, a cell is incubated in a microwell embedded in a polyacrylamide gel matrix. The microwell is enclosed using an antibody patterned glass slide, and the enclosed system is allowed to incubate while proteins are secreted from single cells. After designated protein secretion windows, the chip is disassembled and the microgel portion containing single-cells undergoes a single-cell Western blotting workflow to assay intracellular protein isoforms, while the antibody patterned glass slide undergoes immunoprobing workflows to assay secreted proteins.

Estimation of the Lower Limit of Detection of Secreted Molecules by Modelling Simulations.
To estimate the lower limit of detection of secreted proteins in our proposed assay, we developed a modelling analysis to approximate the concentration of target molecules secreted from a single-cell in an enclosed microwell over time (Figure 2). Our modelling analysis considers a single cell during the enclosed chip incubation stage of the assay. Specifically, the cell (15 μm diameter) is

isolated in a microwell (30 μm diameter; 30 μm height) patterned into a polyacrylamide (8%T) microgel chip. The microwell volume surrounding the cell is filled with fluid and the top and bottom of the chip is enclosed by glass slides that are impermeable to secreted molecules. The target secreted protein is assumed to a hydrodynamic radius of 2 nm (corresponding to a ~21 kDa protein, expected size of common IL-6 cytokine).[11] The target protein is secreted from the cell at a rate of 10 molecules per second, which is within the range of expected cytokine secretion rates.[6,7,8] This modelling analysis can be used to approximate the concentration of secreted proteins in the microwell and surrounding gel matrix at specified time points. In Figure 2, the concentration distribution after 2 hours of cell incubation is shown by the colormap that overlays the model.
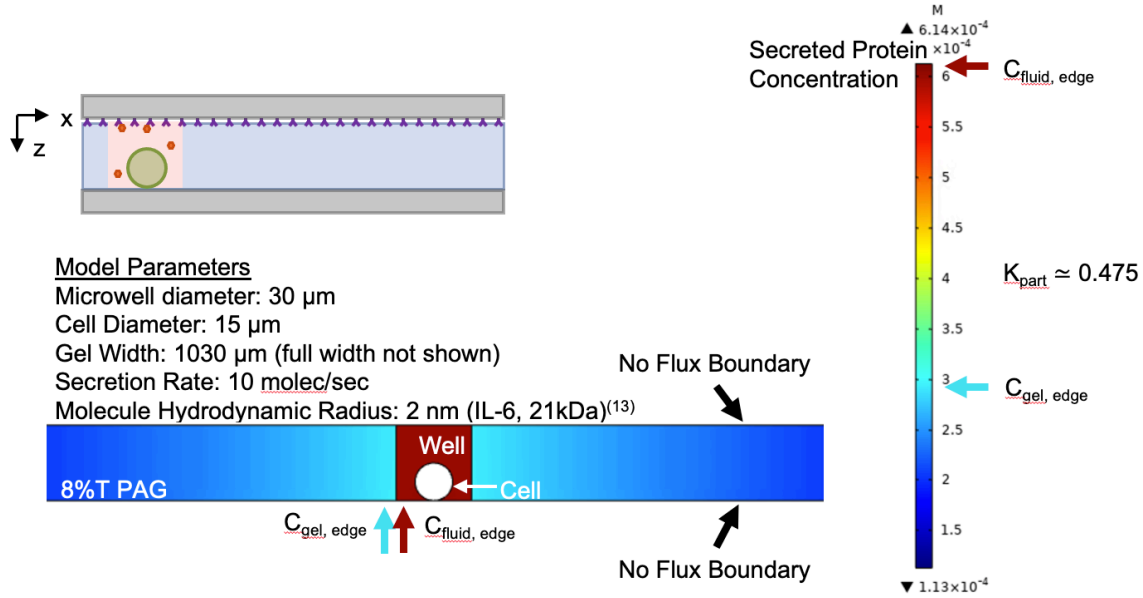

Figure 2. A modeling analysis was performed in COMSOL to estimate the concentration distribution of secreted proteins during cell incubation in a microwell embedded in a polyacrylamide gel matrix. Modeling parameters are included in the figure.

As expected, a portion of the secreted proteins are diffusively lost from the microwell into the gel matrix during cell incubation, though these losses are partially mitigated by size exclusion partitioning induced by the gel matrix. To determine the impact that the diffusive protein losses from the microwell have on the concentration of molecules available for detection in the microwell by microengraving, we calculated the proportion of single-cell secreted proteins remaining in the gel-embedded microwell compared to the total number of secreted molecules. This proportion is determined by the following equation

$$Protein\ Remaining\ in\ Well = \frac{[Ag_{well}]}{[Ag_{well}] + [Ag_{gel}]} \quad (1)$$

where $[Ag_{well}]$ is the concentration of secreted protein in the microwell, and $[Ag_{gel}]$ is the concentration of secreted protein in the gel matrix. The proportion of protein remaining in well is plotted over a 2 hour incubation window in Figure 3, and shows that ~10% of the total secreted proteins remain in the microwell after 2 hours. After developing this modelling framework, we

applied it to compare the previously reported lower limit of secreted protein detection in PDMS-based microengraving assays (0.4-0.7 molec/s for 2 hr single-cell incubation) to the expected concentration of secreted proteins remaining in a microwell.[8] We observe that for a secretion rate of 10 molecules per second the total number of molecules remaining in the microwell at 2 hours is above the previously reported lower limit of secreted protein detection in PDMS-based microengraving assays.
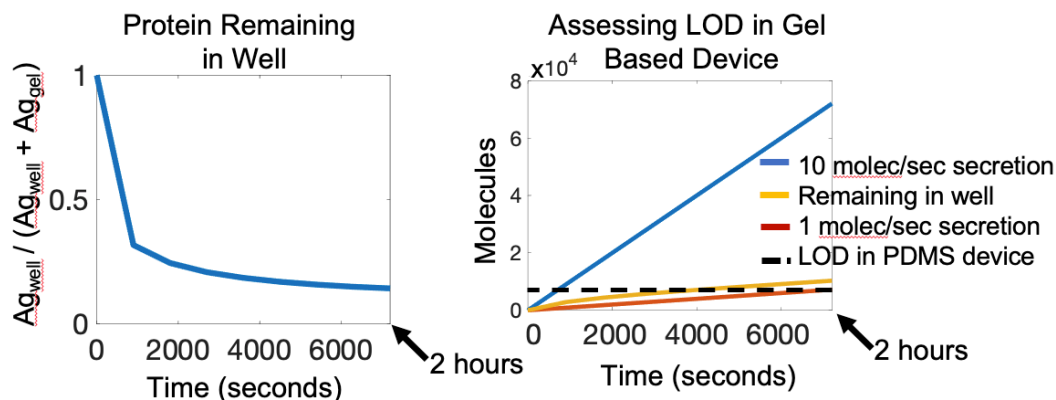

Figure 3. Secreted proteins are diffusively lost from the microwell into the gel matrix during cell incubation, adversely impacting the concentration of secreted proteins remaining in microwells that are available for detection by microengraving. (Left) The proportion of molecules remaining in the microwell compared to the total amount of molecules secreted from a cell is plotted over time. (Right) The proportion of molecules remaining in the microwell correspond to a lower limit of detection for single-cell protein secretion rates of ~10 molecules per second for a 2 hour incubation window.

Secreted IL-6 Detected from Bulk U-251.

We next sought to establish a model cell line and secreted target protein to be later used in device validation experiments. We selected U251 human glioblastoma cells and secreted IL-6 cytokines, as evidence from the literature suggested that cytokine secretion from U251 cells would be above the lower limit of detection for existing single-cell secretomic devices. To verify that the in-house U251 cells do secrete IL-6 and approximate the single-cell IL-6 secretion rate, we assayed by ELISA the bulk supernatant of U251 cell culture for IL-6 cytokines. To establish the ELISA assay, we first characterized the IL-6 concentration regime over which a linear relationship between IL-6 solutions of known concentrations and absorbance could be observed (Figure 4). The data were fit by linear regression in order to extrapolate IL-6 concentration in samples of unknown IL-6 concentration. We characterized a linear fit equation between absorbance and IL 6 concentration as

$$Absorbance = 0.0009 * [IL6] + 0.0693 \quad (2)$$

where Absorbance indicates arbitrary units of absorbance, and [IL6] indicates concentration of IL-6 (pg/mL).
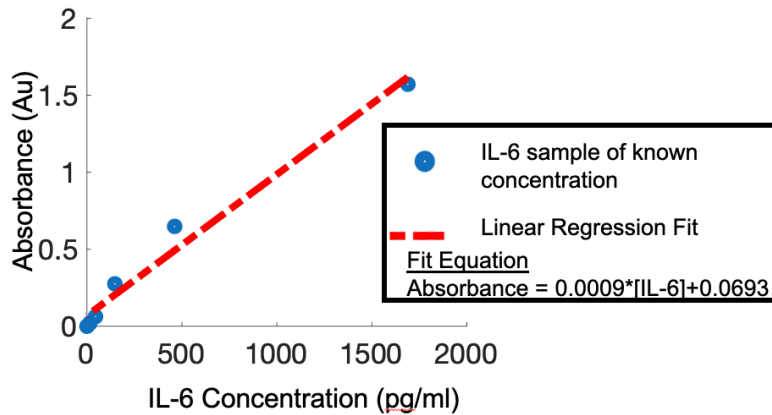
Figure 4. Characterization of the relationship between solution absorbance and solution IL-6 concentration is determined for an ELISA kit using solutions of known IL-6 concentration.

After characterizing the relationship between absorbance and IL-6 solution concentration, we then applied the ELISA to our lab's in house U251 human glioblastoma cell line to approximate IL-6 cytokine secretion rate. To do so, U251 cells were cultured in serum-free media for 41 hours and the cell culture supernatant was assayed using the ELISA. A mean absorbance of 0.4304 +/- 0.0146 was observed (n=6, arbitrary units, error reported as standard deviation, serum-free background subtracted). This mean absorbance corresponds to an extrapolated IL-6 concentration of 393.7695 pg/mL. Serum-free media not exposed to IL-6 was also assayed, and its absorbance 0.0580 +/- 0.0027 (n=2) was extrapolated to predict a near-zero IL-6 concentration of -12.3472 pg/mL (Table 1).

Sample	Measured Absorbance	Extrapolated IL-6 Concentration
U251 Supernatant	0.4304 +/- 0.0146 (n=6)	*393.7695 pg/mL*
Serum-Free Media	0.0580 +/- 0.0027 (n=2)	-12.3472 pg/mL

Table 1. The absorbance of U251 bulk cell culture supernatant is measured by ELISA and the characterization of absorbance vs. IL-6 concentration is used to extrapolate the IL-6 concentration in U251 bulk cell culture supernatant.

To approximate the average single-cell IL-6 secretion rate, we used the extrapolated IL-6 supernatant concentration, the supernatant volume (10 mL), the cell culture time (41 hours), and the final cell count at the time of supernatant removal (~1,077,700 cells). These values are summarized in Table 2, and the estimation of the average single-cell IL 6 secretion rate was determined (0.7096 molec/sec). During cell culturing, the cell culture expanded from ~50% flask confluency to ~80% flask confluency during the 41-hour culture time window, making the estimated single-cell IL-6 secretion rate a conservative estimate. This estimated average secretion rate is near the reported single-cell IL-6 secretion LOD for microengraving systems (0.5-0.7 molec/sec). The previously reported LOD in microengraving systems was derived from a 2-hour

incubation window of a cell in a microwell. As the total molecule abundance available for detection increases with time, it was hypothesized that longer incubation windows could enable slower molecule secretion rates to be detected.

Extrapolated IL-6 Supernatant Concentration	Supernatant Volume	Culture Time	Cell Count at Supernatant Removal	Estimated Single-Cell IL-6 Secretion Rate
393.7695 pg/ml	10 mL	41 hours	1077700 cells	*0.7096 molec/sec*

Table 2. The single-cell IL-6 secretion rate is determined from the IL-6 concentration in bulk U251 cell culture supernatant, the supernatant volume, the cell culture time, and the cell count in cell culture.

Antibody Patterning on Poly-L-Lysine Glass Slides.
The IL-6 detection component of the proposed immunoassay involves capturing IL-6 onto an antibody coated glass slide. Antibodies can be coated onto glass slides by first treating glass slides with poly-L-lysine. Protocols for coating glass slides with poly-L-lysine for patterning with organic molecules (DNA, anti-bodies, etc.) are commonly available in "omics" literature, and have been applied for capture antibody patterning of glass slides in microengraving. In-house glass coating involves organic material removal by strong base wash, poly-L-lysine coating, and storage in a dry environment. Alternatively, pre-prepared slides are commercially available. In the subsequent experiments, Thermo Fisher Microarray SuperChip slides were used to expedite the early demonstration processes.

To characterize the concentration of antibodies required to saturate the available antibody patterning sites on poly-L-lysine-treated glass slides, we patterned defined regions of poly-L-lysine glass slides with specific concentrations of fluorescently-labelled antibodies using microarray gaskets (Figure 5). Antibody concentrations included 0 µg/mL, 1 µg/mL, 40 µg/mL, 100 µg/mL, and 500 µg/mL, and were informed by the antibody concentrations used in previously reported microengraving systems (Figure 5A). After patterning the defined regions with the specified antibody concentrations, the on-chip antibody fluorescence was imaged by microarray scanner and the mean fluorescence in each patterning region was determined (Figure 5B). The mean fluorescence for regions treated with antibody concentrations ≥ 40 µg/mL were not statistically distinct (p>>0.05, Mann-Whitney U-Test). Mean fluorescence for 1 µg/mL and 0 g/mL Ab treatments were statistically distinct from Ab treatments of 40 µg/mL (p<0.027 Mann-Whitney U-Test). These results indicate that available Ab patterning sites are saturated at 40 µg/mL and is consistent with concentrations used in the microengraving literature.[7]
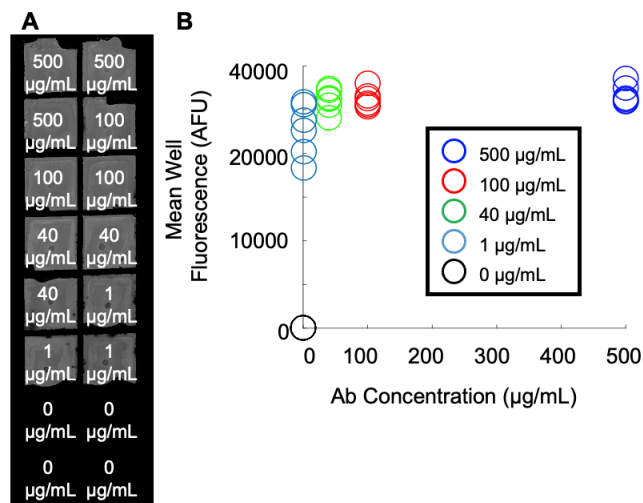
Figure 5. Poly-L-Lysine treated glass slides can be used for patterning capture antibodies on the glass slide surface. (A) Image of a poly-L-lysine coated glass slide after patterning by varied concentrations of Dk α-Rb AF647, washing, and gasket removal. Image generated by microarray scanner, 635 nm laser excitation. (B) Plot of mean well fluorescence intensity of glass slides described in A (2 glass slides, same Ab concentrations applied).

Application of Antibody Patterned Glass Slides for IL-6 Detection from Bulk Cell Supernatant and Single-Cells by Microengraving

After determining conditions for saturating antibody patterning sites on poly-L-lysine-treated glass slides, we next sought to use the antibody patterned glass slides to capture IL-6 by sandwich immunassay. As a model system, we again used the bulk supernatant of U251 glioblastoma cell culture, which we previously determined to have an IL-6 concentration of 393.7695 pg/mL (Table 1). To assess IL-6 capture over a range of IL-6 concentrations, we performed serial dilutions of the U251 supernatant, as described in Figure 6. IL-6 protein solutions of known concentrations were used in a microarray gasket system to validate the sandwich immunoassay mechanism. IL-6 concentrations used for characterizing detection antibody fluorescence are shown in Figure 6. Resulting detection antibody fluorescence captured to the glass slide is shown in Figure. Non-specific well signal outside the confines of the gasket chambers indicates need for additional characterization in (i) Ag washing, (ii) Ab probe delivery, (iii) blocking and (iv) Ab washing. Descriptions of these steps in literature are not detailed to convey specific tacit knowledge. Additional next steps might include patterning with capture antibody and detection of fluorescently-labelled IL-6, investigating higher concentrations of IL-6, or modifying handling steps to prevent cross-talk between wells.
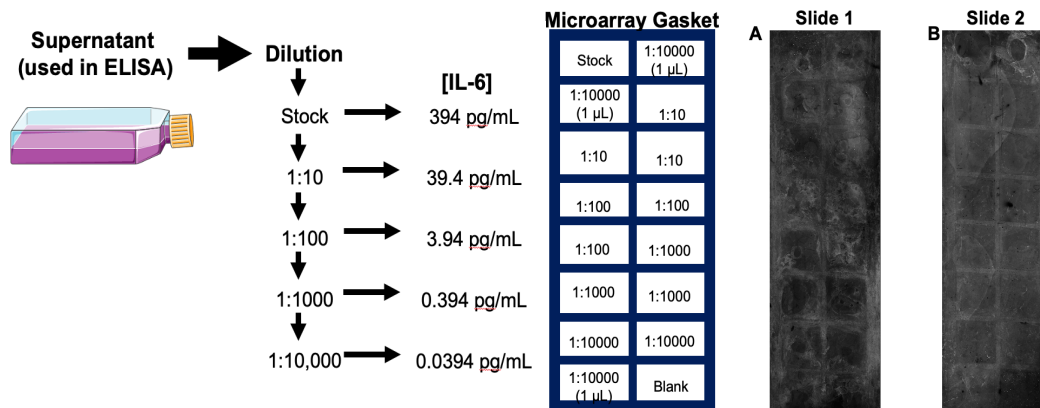
Figure 6. U251 bulk cell culture supernatant was serially diluted and used as target protein sample solution for IL-6 detection by microengraving. (A&B) Glass slides coated with capture antibodies were exposed to specific IL-6 antibody concentrations using microarray gaskets to define specific regions of interest, and subsequently probed using fluorescently-labelled antibodies. Antibody fluorescence shown in white.

We additionally applied our capture antibody patterned glass slides for the detection of IL-6 secreted from single U251 cells settled in microwells. Microwell arrays were formed in two separate ways: (i) microwells patterned into a PDMS array or (ii) microwells patterned into a 7%T polyacrylamide gel grafted onto a glass slide. Microwells in both cases had 16 μm radius and 32 μm depth. Cells were gravity settled into microwell arrays and a capture antibody patterned glass slide was brought into contact with the microwell array surface, and the assembly was compressed using the microarray gasket system. To provide enough time for the concentration of IL-6 secreted from single-cells in microwells to be above the theoretical limit of detection of our chip, the system was enclosed for 2 hours. After disassembly of the incubation system, the chip was probed with fluorescently labelled antibodies, washed and imaged. Imaging results are shown in Figure 7. No microwell specific antibody fluorescence can be identified in the imaged chips, and nonspecific antibody fluorescence can be observed throughout the chip. These preliminary experimental observations could potentially be due to insufficient IL-6 protein secretion from single-cells during the 2 hour incubation window, incomplete detection antibody removal during washing steps, or other experimental challenges.
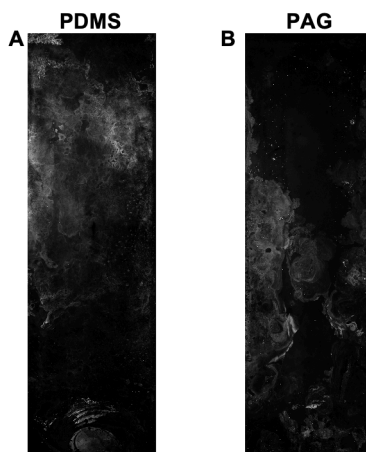
Figure 7. Glass slides patterned with capture antibodies were exposed to U251 glioblastomas isolated in individual microwells and incubated for 2 hours. Microwells were made of either (A) PDMS or (B) polyacrylamide gel. Glass slides were subsequently immunoprobed using fluorescently-labelled antibodies. Antibody fluorescence is shown in white.

Before repeating single-cell microengraving experiments, we propose that detection of purified protein including antibody amplification steps should first be demonstrated. Additionally, in handling the system, there was an observed need for a simplified microwell array glass capture slide compression system, as the gaskets were difficult to uniformly tighten especially while in buffer solution. Commercially available hybridization chambers are de-scribed in microengraving literature for these steps (similar cost to individual gasket purchase). If specific LOD characterization experiments using purified proteins do not result in detectable amounts of target proteins from single-cells, inclusion of IL-6 secretion stimuli may be required.

A.3 Conclusions

In order to facilitate the simultaneous detection of secreted proteins and intracellular isoforms from single cells, we introduced here a proposal for a microwell-based device that facilitates secreted protein detection by microengraving and intracellular protein isoform detection by single-cell western blotting. In developing this project, we demonstrated that the Herr lab in-house U251 glioblastoma cells secrete IL-6 at concentrations that can be detected by kit ELISA in bulk, and perform calculations to approximate the single-cell secretion rate of IL-6 from the cell line. We perform a modelling analysis, we estimate a theoretical lower limit of detection in our chip, and determine that a 2 hour cell incubation time is sufficient for the secreted concentration of IL-6 from U251 cells to be above our chips theoretical limit of detection. We validated a method for antibody patterning on poly-L-lysine treated glass slides, and determined that available antibody patterning sites can be saturated with a concentration of 40 μg/mL. Application of the antibody patterned glass slides for IL-6 detection by immunosandwich assay were inconclusive, but we identify several potential next steps to inform continued investigations: (i) detection of fluorescently-labelled purified protein IL-6 on chip by microengraving should be demonstrated, (ii) detection of IL-6 from bulk supernatant at higher concentrations than investigated here should be pursued, and (iii) to boost target protein secretion rate, IL-6 secretion stimuli should be included

in cell culture media, or a model biological system with higher cell secretion rates should be investigated (e.g. antibody secretion from hybridomas).

A.4   References

1   S. Liu, J. S. Lee, C. Jie, M. H. Park, Y. Iwakura, Y. Patel, M. Soni, D. Reisman and H. Chen, *Cancer Res.*, 2018, **78**, 2040–2051.

2   J. Arribas, J. Baselga, K. Pedersen and J. L. Parra-Palau, *Cancer Res.*, 2011, **71**, 1515–1519.

3   H. Kawamoto, K. Kawamoto, T. Mizoue, T. Uozumi, K. Arita and K. Kurisu, *Acta Neurochir. (Wien).*, 1996, **138**, 1442–1448.

4   M. E. KENDALL and W. C. HYMER, *Endocrinology*, 1987, **121**, 2260–2262.

5   N. Ahlborg and B. Axelsson, *Methods Mol. Biol.*, 2012, **792**, 77–85.

6   P. Rorsman and F. M. Ashcroft, *Physiol. Rev.*, 2018, **98**, 117–214.

7   J. C. Love, J. L. Ronan, G. M. Grotenbreg, A. G. Van Der Veen and H. L. Ploegh, , DOI:10.1038/nbt1210.

8   Q. Han, E. M. Bradshaw, B. Nilsson, D. A. Hafler and J. C. Love, *Lab Chip*, 2010, **10**, 1391–400.

9   Y. Lu, Q. Xue, M. R. Eisele, E. S. Sulistijo, K. Brower, L. Han, E. David Amir, D. Pe, K. Miller-Jensen, R. Fan and G. P. Nolan, , DOI:10.1073/pnas.1416756112.

10   Y. Lu, J. J. Chen, L. Mu, Q. Xue, Y. Wu, P. H. Wu, J. Li, A. O. Vortmeyer, K. Miller-Jensen, D. Wirtz and R. Fan, *Anal. Chem.*, 2013, **85**, 2548–2556.

11   J. D. Kimmel, G. A. Gibson, S. C. Watkins, J. A. Kellum and W. J. Federspiel, *J. Biomed. Mater. Res. Part B Appl. Biomater.*, 2009, **9999B**, NA-NA.